Studies on the Design of Thin Microwave Linear to Circular Polarization Converters Based on Frequency Selective Surface

Thesis submitted for the award of the Degree
of

Doctor of Philosophy

in the Department of Electrical Engineering

by

Mohammad Ayoub Sofi
(2018REE0015)

Under the supervision of

Dr. Kushmanda Saurav

and

Prof. Shiban Kishen Koul

भारतीय प्रौद्योगिकी संस्थान जम्मू
INDIAN INSTITUTE OF TECHNOLOGY JAMMU
विद्याधनं सर्वधन प्रधानम्

Indian Institute of Technology Jammu
Jammu 181221

September 2021

Declaration

I hereby declare that the matter embodied in this thesis entitled **"Studies on the Design of Thin Microwave Linear to Circular Polarization Converters Based on Frequency Selective Surface"** is the result of investigations carried out by me in the Department of Electrical Engineering, Indian Institute of Technology Jammu, India, under the supervision of **Dr. Kushmanda Saurav** (IIT Jammu) and **Prof. Shiban Kishen Koul** (Center for Applied Research in Electronics, IIT Delhi) and it has not been submitted elsewhere for the award of any degree or diploma, membership etc. In keeping with the general practice in reporting scientific observations, due acknowledgements have been made whenever the work described is based on the findings of other investigators. Any omission that might have occurred due to oversight or error in judgment is regretted. A complete bibliography of the books and journals referred in this thesis is given at the end of the thesis.

September 2021	Mohammad Ayoub Sofi
Indian Institute of Technology Jammu	(2018REE0015)

I dedicate this thesis to my late grandparents. Even though they did not had formal education, they never stopped sharing their wisdom, tutelage, support and encouragement to study and always prayed for my prosperity in education and blissful life.

Abstract

Frequency selective surface (FSS) is a periodic design of infinite array of metallic patterns on single/both sides of a dielectric substrate to selectively reflect, transmit and/or absorb incident electromagnetic (EM) wave. The behaviour of FSS is determined by its geometrical shape, size, dielectric substrate, spacing and orientation. FSS designs are widely employed in radomes, antennas, spatial filters, high-impedance surfaces, polarization converters, absorbers, lens, transmit/reflect-arrays, and EM shielding in the microwave and millimeter-wave regimes.

The circularly polarized (CP) state of an EM wave is desirable for many electromagnetic radiation applications due to their features like mitigation of multi-path fading, reduction of the Faraday rotation effect when signals propagate through the ionosphere and immunity of the polarization mismatching between transmitting and receiving antennas. Due to the role of CP waves in wide range of applications, the control and manipulation of polarization state of an EM waves has always been of interest in the scientific community. CP waves can be obtained either directly from a CP antenna or transforming the LP wave into a CP wave by passing it passed through a linear-to-circular (LTC) polarization converter. The second scheme is more convenient and desirable in antenna arrays where it is difficult to generate CP wave from each antenna element.

With the advent of FSS based approaches, many efforts have been made to manipulate and control polarization by using LTC polarization converters to transform an incident linearly polarized (LP) wave into a reflected/transmitted CP wave. However, most of the LTC polarization converters reported are multilayered, bulky, and prone to fabrication error due to misalignment between each layer. Single substrate layer LTC polarization converter is therefore an effective solution to resolve the errors caused due to multilayer problem. Although, single substrate layer designs overcome the problem associated with multilayer configurations, the independent control of LP and CP states are still challenging. Therefore, a lot of research with respect to the reconfigurable LTC polarization converters can be carried out. The angular stability of a LTC polarization converter determines its ability to provide satisfactory performance for oblique incidence of the incident wave. However, most of the reported single substrate layer LTC polarization converter designs achieve polarization conversion for normal incidence only, which practically becomes prohibitive, as incoming waves can have arbitrary incidence angles. Furthermore,

the LTC polarization converter with wide angular stability must possess compact size. Therefore, there has been significant interest towards the design of stable and compact size LTC polarization converters.

In satellite communications to enhance the isolation between the transmitted and received signals, an antenna must function in two nonadjacent frequency bands with orthogonal polarization. Therefore, dual-band LTC polarization converters with orthogonal polarization at the two operating frequency band can be explored which can be used in combination with dual-band LP antennas to realize a dual-band orthogonally polarized CP antenna. A few dual-band LTC polarization converters reported in literature are multilayered and possess large size. Therefore, single substrate layer dual-band LTC polarization converter with compact size further need to be explored.

The motivation behind this thesis is to resolve the above limitations through developing single layer polarization reconfigurable and wide angular stable with compact size LTC polarization converter structures. Furthermore, a single layer dual-band LTC polarization converter with orthogonal CP at lower and upper frequency bands of operation is also developed. This thesis also presents the utilization of LTC polarization converters developed in realizing the CP patch antenna, antenna arrays, and dual-band four port MIMO antenna. The design concepts of the proposed LTC polarization converters and CP antennas have been validated by measurements carried out on the fabricated prototypes.

A linear-to-circular polarization reconfigurable converter (PRC) working in transmission mode is presented in this thesis. The PRC's fundamental unit consists of a cascade of half-hexagon structure and its mirror replica printed on both sides of a single layer substrate (ϵ_r=2.2 and $\tan\delta$ = 0.0009) as shown in Figure 1. Both the top and bottom metal pattern are made of copper having conductivity (σ) of 5.8×10^7 S/m and thickness of 0.035 mm. Initially, a slot of length 1 mm is etched in the central arm of the converter to obtain the two states, one without slot (State I) and the other with slot (State II) which are later realized by using a PIN diode BAR63-02LE6327 from the Infineon Technologies with a length equal to 1 mm. The state of the diode controls the behaviour of the proposed converter to a $\phi = 45°$ LP incident wave and transmits a LP and CP wave in state I (ON State) and II (OFF State), respectively as can be observed from results provided in Figure 2. In the state I, the PRC transmits two orthogonal components with equal magnitude and phase difference varying between $13° - 19°$ in the frequency range 13.76

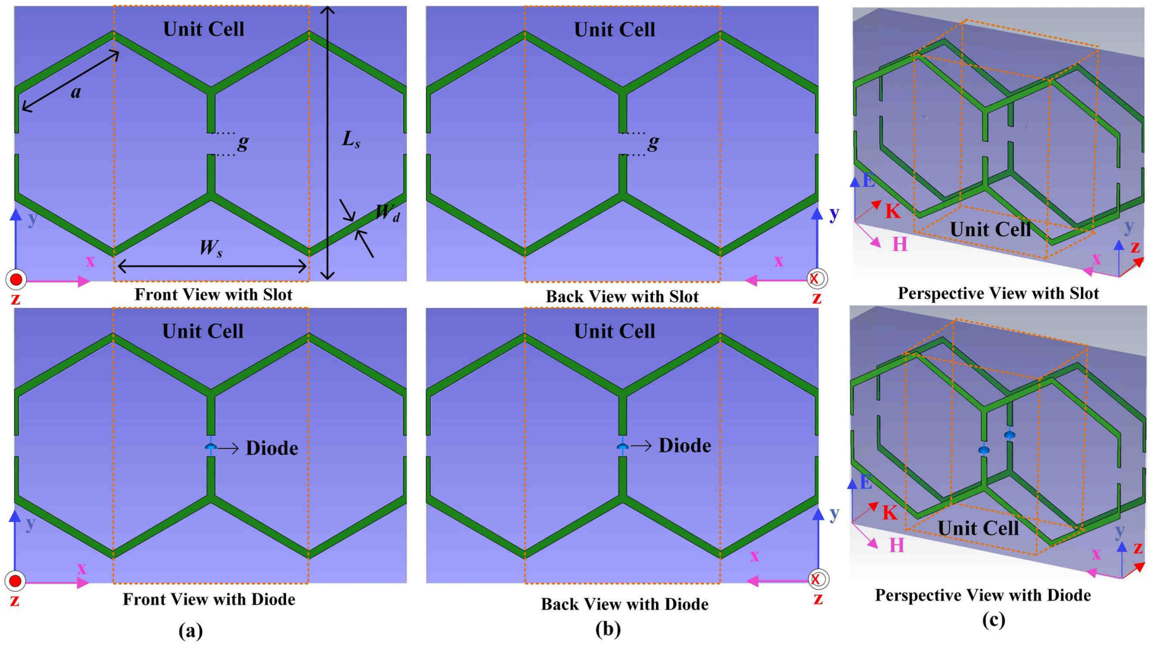

Figure 1: Schematic of the proposed unit cell of the polarization reconfigurable converter (a) front view, (b) back view and (c) perspective view. $W_s = 9.25$, $L_s = 13$, a = 5.34, g = 1, and $W_d = 0.34$ (all dimensions are in mm).

– 17.0 GHz as shown in Figure 2(a) representing an LP wave. However, for the state II, two orthogonal components have equal amplitude with a phase difference of 85°–111° in the frequency band 14.84 – 15.84 GHz as shown in Figure 2(b) representing a CP wave. Therefore, controlling the state of the diode reconfigurability between LP and CP states can be achieved. The resonant frequency for x- and y-polarization in state I is different as shown in Figure 2(a). The reason for frequency shifting is attributed to the fact that the current length along the y-direction is increased, which results in the decrease of the resonant frequency of the unit cell for y-polarization, as shown in Figure 2(a). In state II,

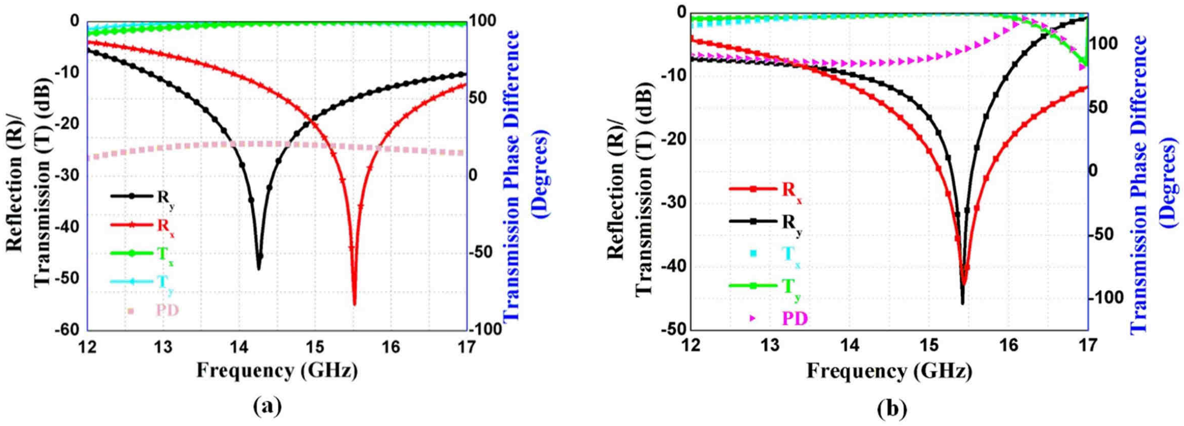

Figure 2: Plot of reflection/transmission coefficient and transmission phase difference of polarization reconfigurable converter (PRC) for (a) g = 0 (Diode ON) (b) g = 1 (Diode OFF), R_x, R_y is reflection and T_x, T_y is transmission for x- and y-polarized incident wave respectively, PD is phase difference between T_x and T_y.

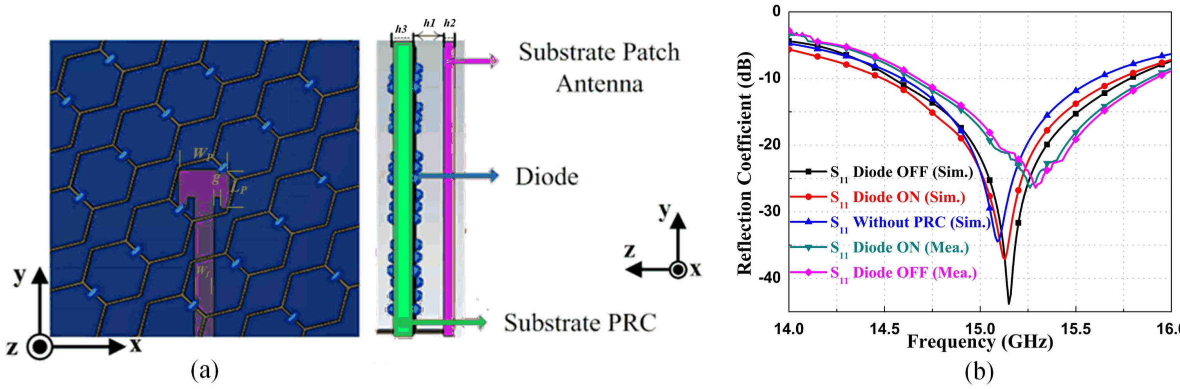

Figure 3: (a) Schematic of antenna with polarization reconfigurable converter (PRC). (b) Simulated and measured reflection coefficient of patch antenna with PRC. $h_1 = 6.5$, $h_2 = 0.762$, $h_3 = 3.04$, $w_p = 8.25$, $L_p = 6.4$, $g = 1$, and $w_f = 2.85$ (all dimensions in mm).

there is an open circuit in the central arm of the unit cell, and the current does not find the continuous path through this arm. The current is equally distributed in the upper and lower half of the unit cell and traverses equal length for both the polarization along the x- and y-axes. Therefore, the unit cell resonates around the same frequency in this state for both the polarizations. The polarization reconfigurable behavior of the converter is verified by placing 45° clockwise rotated 6 × 6 array of the proposed PRC's unit cell on top of an LP patch antenna shown in Figure 3(a) as a superstate at a distance of $\lambda_o/3$ (λ_o is calculated with respect to 15.15 GHz) to obtain a polarization reconfigurable CP antenna resonating at 15.1 GHz. The optimum height of $\lambda_o/3$ is obtained after performing the parametric studies of the height of superstate above the LP patch antenna. The S-parameters of the patch antenna with the PRC is shown in Figure 3(b) exhibiting an

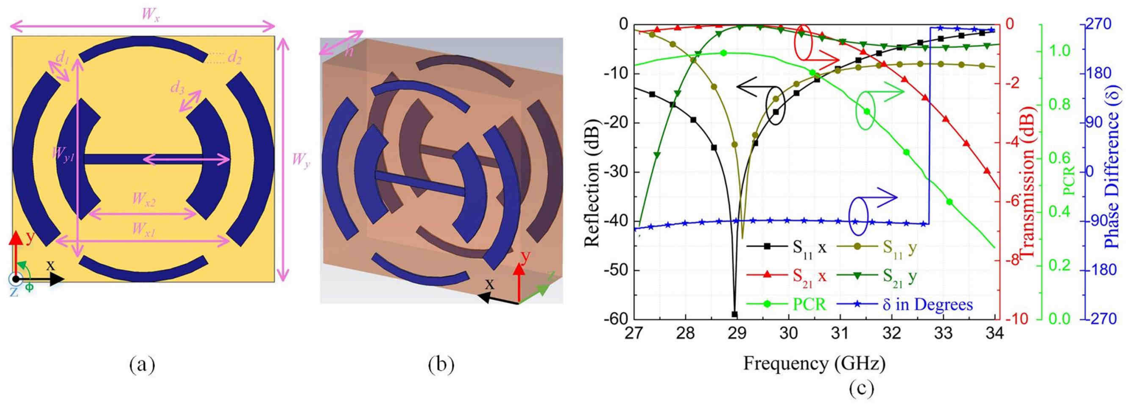

Figure 4: (a) Front, (b) perspective views and (c) magnitude of reflection, transmission coefficients, PCR and phase difference between the orthogonally polarized transmission coefficients of the proposed converter. $W_x = 3.96$, $W_{x1} = 2.23$, $W_{x2} = 1.35$, $W_y = 3.76$, $W_{y1} = 3.02$, $d_1 = 0.15$, $d_2 = 0.3$ and $d_3 = 0.42$ (all in mm).

impedance bandwidth of 6.52 % (14.75 – 15.78 GHz).

The design of single layer wide angular stable LTC polarization converter is also discussed in this thesis. Figure 4(a) shows the schematic of the unit cell of this LTC polarization converter which is designed using split-rings and a metallic strip printed on both sides of a single substrate layer (ϵ_r=2.2 and $\tan\delta = 0.0009$). The x- and y-polarized orthogonal transmitted components are equal in magnitude as shown in Figure 4(c) in the frequency range of 28.56 – 31.23 GHz and the corresponding phase difference ($\Delta\phi_{xy} = \phi_x - \phi_y$) between them, $\Delta\phi_{xy} = -90°$. Based on the results presented in Figure 4(c), it can be implied that a left hand circularly polarized (LHCP) wave is transmitted from the polarization converter when excited by an incident LP wave. The polarization conversion ratio (PCR) of the proposed polarization converter shown in Figure 4(c) is greater than 0.85 (85%) in the frequency band of 28.0 – 31.0 GHz, which denotes an excellent polarization purity. The maximum PCR achieved is 0.992 (99.2%) at 29.23 GHz. The polarization converter can convert an incident LP wave to a CP wave with very low insertion loss (< 1.25 dB) in the frequency band: 28.75 – 32.85 GHz. Moreover, for oblique incidence up to 45^0, axial ratio bandwidth (ARBW) and ellipticity (e) responses remain quite stable. A prototype of 71 × 71 unit-cells of the proposed LTC polarization converter is fabricated using photolithographic technique and measurement results are in good agreement with simulated ones. The measured ARBW or e in the range of 0.94 – 0.98 is obtained in the frequency band of 29.50 – 32.65 GHz (10.13%). Furthermore, the characteristics of the polarization converter are verified by placing a 45° rotated array of 15 × 15 elements

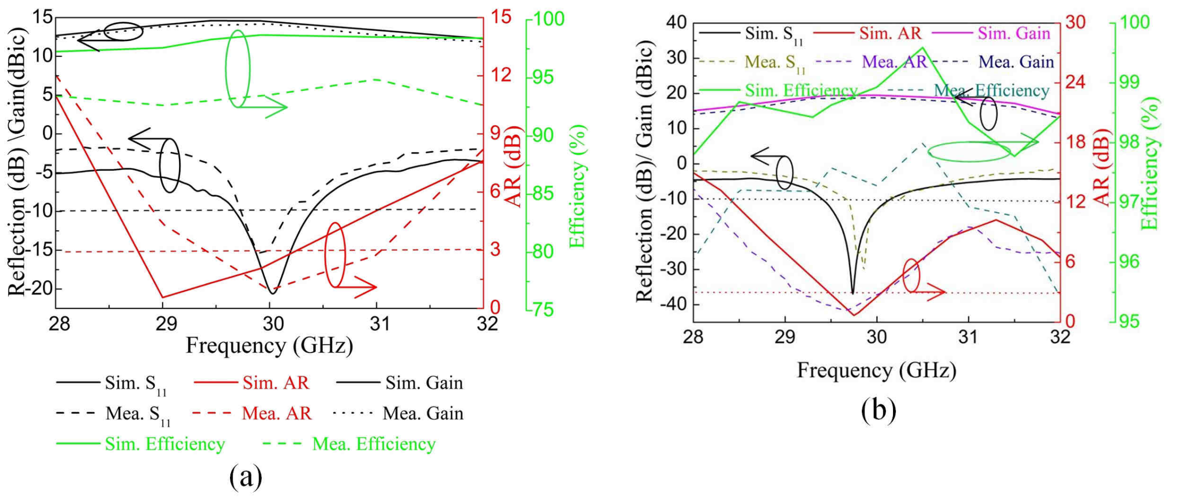

Figure 5: Simulated and measured reflection coefficient, AR, gain, radiation efficiency of the (a) 1 × 4 and (b) 4 × 4 CP patch antenna array.

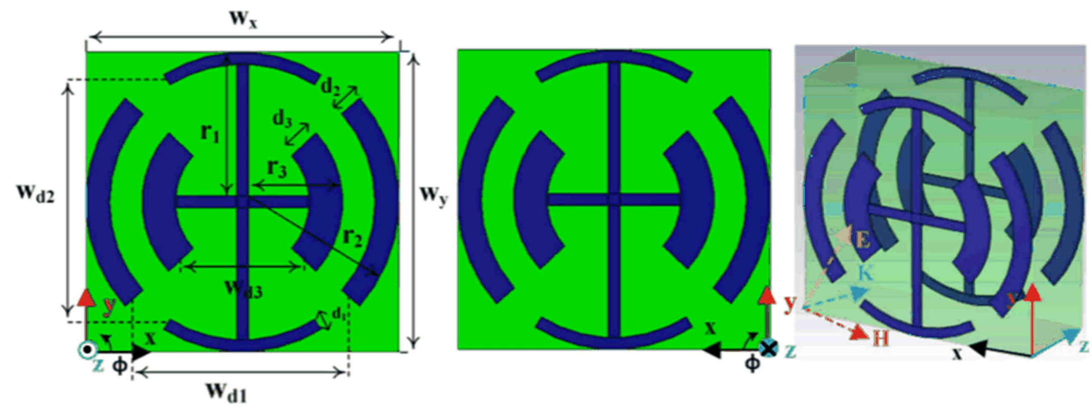

(a) (b) (c)

Figure 6: Schematic of the proposed unit cell of the dual-band LTC polarization converter (a) front view, (b) back view and (c) perspective view. d_1=0.15, d_2= 0.3, d_3=0.42, r_1=1.86, r_2=1.95, r_3= 1.25, w_{d1}= 2.2, w_{d2}= 3, w_{d3}= 1.35, w_x =3.90, w_y =3.72 (all dimensions are in mm).

of its unit-cell in the broadside direction of a 1 × 4 and 4 × 4 LP patch antenna array operating in the same frequency band such as that of the polarization converter. The S-parameters, AR and radiation efficiency of the integrated 1 × 4 and 4 × 4 array antenna is shown in Figure. 5(a) and (b), respectively. The overlapping CP bandwidth of 1.67% (29.75 – 30.25 GHz) and 1.51% (29.65 – 30.10 GHz) is exhibited by the designed 1 × 4 and 4 × 4 CP patch antenna array, respectively. The proposed LTC polarization converter integrated with 1 × 4 and 4 × 4 antenna array shows a measured gain of 14.1 dBic and 18.7 dBic, respectively in the xz-plane. The proposed polarization converter and CP antenna arrays can be used for uplink Ka-band fixed-satellite service (29.5 – 30.0 GHz) and military satellite communication (30.0 – 31.0 GHz) applications.

A compact dual-band LTC polarization converter with orthogonal CP at the lower and upper operating frequency bands is discussed in this thesis. The schematic of the proposed dual-band LTC polarization is shown in Figure 6. The proposed converter is designed on a single layer substrate and is composed of metallic split-rings with horizontal and vertical metallic strips printed on both sides of substrate to improve transmission. The extra metallic strip along the vertical direction creates the second resonance at around 20 GHz compared to the previous converter design discussed above to exhibit dual-band operation. The unit cell of the converter has a size of 3.72 × 3.90 × 1.52 mm^3 ($0.0072\lambda_o^3$, λ_o is calculated with respect to 20.67 GHz). The reflection response of the proposed cell is depicted in Figure 7(a) and clearly there are two frequency bands centered at 20.92 GHz (≈ 20.10−21.75 GHz) and 30.25 GHz (≈29.10−31.40 GHz) with reflection coefficient below -10 dB. The magnitude of transmission coefficients for both of the polarizations are

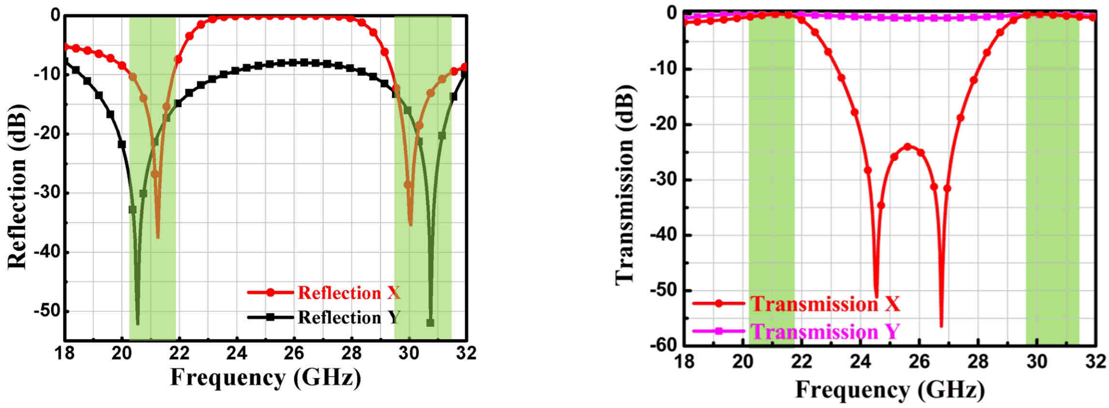

(a) (b)

Figure 7: (a) Reflection and (b) transmission coefficient of proposed dual-band LTC polarization converter.

presented in Figure 7(b) and at both the frequency bands, the transmission magnitude remains better than -0.5 dB. The phase difference of 78.2° − 107.45° in the lower frequency band: 20.10 − 21.75 GHz and -75.72° to -95.66° in the upper frequency band: 29.12 − 31.4 GHz is obtained for the dual-band LTC polarization converter. It is observed that in the transmission response, there are two nulls for T_{xx}. A 180° phase shift is obtained in the transmission of T_{xx}, which can be attributed to the fact that for x-polarized wave, the split-rings in the structure behave as coupled resonators and for y-polarization, they are non-resonant, resulting in the opposite polarizations of the transmitted CP wave in the two frequency bands. The proposed converter has a measured 3-dB axial ratio bandwidth of 5.56% (20.10 − 21.25 GHz) in the lower band and 3.97% (29.12 − 30.30 GHz) at the upper band. The converter transmits a right hand circularly polarized (RHCP)

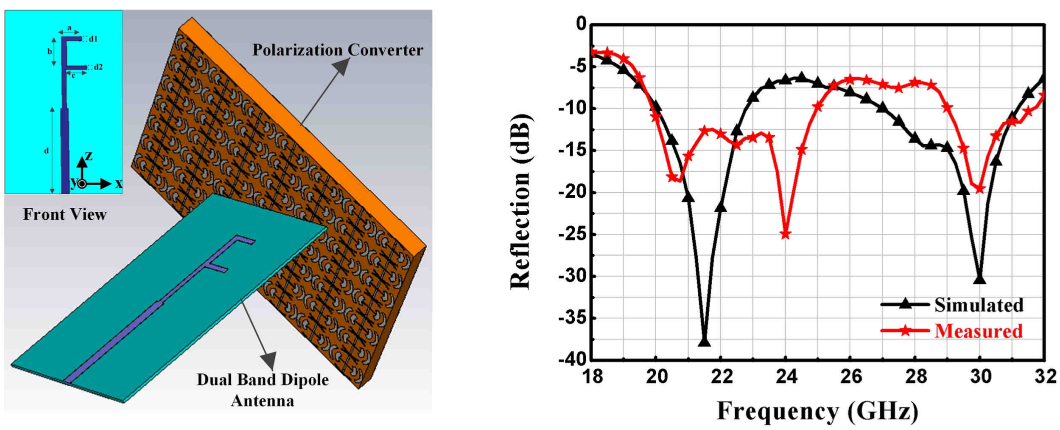

(a) (b)

Figure 8: (a) Integrated dual-band LP dipole antenna with proposed LTC polarization converter. (b) Reflection coefficient of dual band LP dipole antenna integrated with polarization converter. a = 2.6, b = 3.75, c = 2.65 , $d_1 = d_2 = 0.5$, d = 11 (all dimensions are in mm).

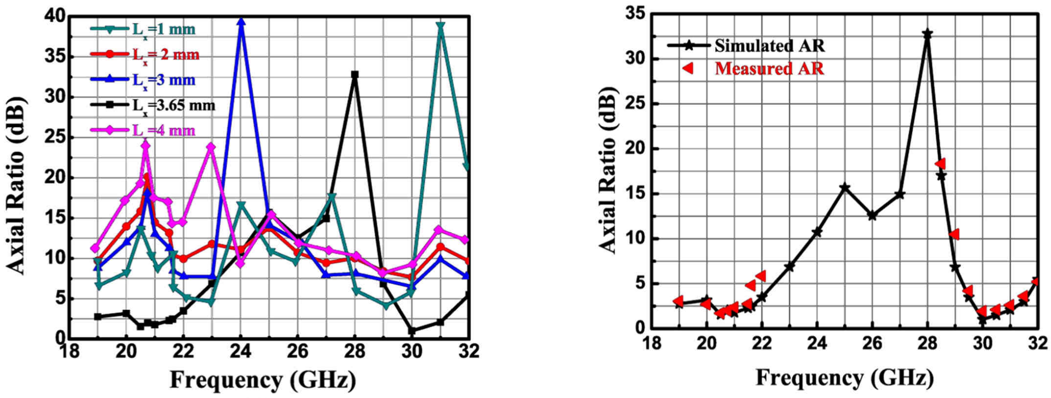

(a) (b)

Figure 9: (a) Variation of the AR in the end-fire direction with the change in the spacing between the dipole antenna and polarization converter. (b) Axial ratio of integrated dual-band LP dipole.

wave at lower band and left hand circularly polarized (LHCP) wave at the upper band for a linearly polarized incident wave. The characteristics of the polarization converter are validated by integrating an array of 7 $\times$ 7 elements of its unit-cell in the end-fire direction of a dual-band LP dipole antenna as shown in Figure 8(a) operating in the same frequency bands like that of the polarization converter. The polarization converter is oriented along $\theta = 45^{o}$, with respect to the axis of the dipole antenna, as shown in Figure 8(a) to ensure that the LP wave of dipole excites the polarization converter diagonally. The reflection coefficient of this integrated antenna better than -10 dB is obtained in the frequency bands: 20.10 $-$ 22.75 GHz and 27.10 $-$ 31.30 GHz as depicted in Figure 8(b). The distance between the dipole antenna and the dual-band LTC polarization converter to obtain the optimum AR less than 3 dB at the two operating frequency bands is determined through parametric studies. The variation in the axial ratio with the change in the spacing of the converter and dipole (L_x) is shown in Figure 9(a). The value of the AR less than 3dB in the lower and upper frequency bands is obtained for $L_x = 3.65$ mm. For values of L_x, less than or more than 3.65 mm, the AR increases, at both the frequency bands of operation indicating that dipole transmits LP waves without being transformed into CP waves. The optimum distance at which polarization converter is placed from the dipole antenna is nearly equal to $\lambda_o/4$ (λ_o being the free space wavelength corresponding to the central frequency of lower frequency band) to perform satisfactorily. The antenna integrated with the polarization converter exhibits measured CP bandwidths of 7.80% and 6.57% (Figure 9(b)) in lower frequency band: 20.10 $-$ 21.75 GHz and upper frequency band: 29.4 $-$ 31.4 GHz, respectively. The integrated antenna can act as a feed source to a

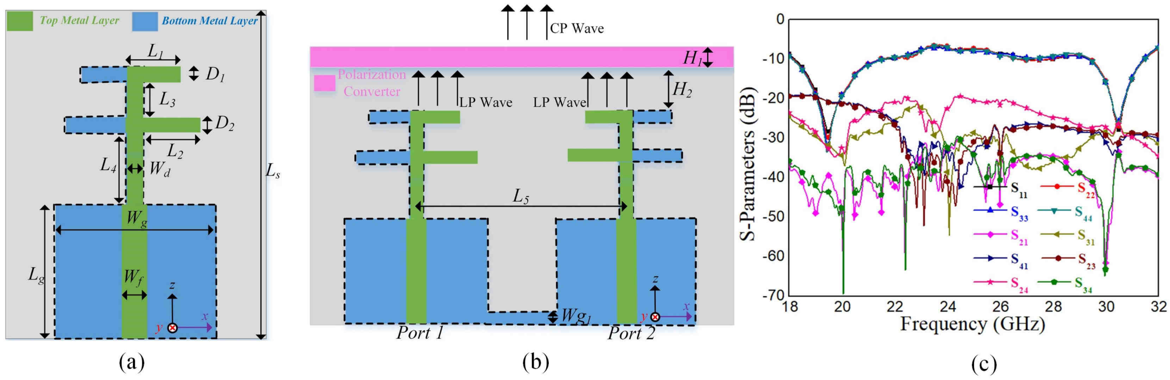

Figure 10: Schematic of (a) single element of MIMO, (b) two-port MIMO and (c) S-parameters of four-port CP MIMO antenna. $L_1 = 2.05, L_2 = 3.13, L_3 = 3.75, L_4 = 5.5, L_5 = 19.60, D_1 = 0.5, D_2 = 0.4, W_d = 0.35, W_f = 0.75, W_g = 11, L_g = 11, L_s = 23.85, H_1 = 1.52, W_{g1} = 0.5, d_1 = 0.15, d_2 = 0.3, d_3 = 0.42, r_1 = 1.86, r_2 = 1.95, r_3 = 1.25, W_{d1} = 2.2, W_{d2} = 3, W_{d3} = 1.35, W_x = 3.90, W_y = 3.72$ (all dimensions are in mm).

high gain dual-band transmit-array for uplink (30.0–31.0 GHz) and downlink (20.2–21.2 GHz) of K/Ka-band military satellite communication.

A dual-band CP four-port multiple-input multiple-output (MIMO) antenna is discussed in this thesis. The schematic of the single element of the MIMO antenna is shown in Figure 10(a). The single element of MIMO is composed of a cascade of two back to back F-shaped dipoles of different lengths resonating at around 20 GHz and 30 GHz. The four-port MIMO antenna is obtained by placing the four single element structures orthogonal to each other with common ground connection. An array of 7×7 elements of the unit cell of dual-band LTC polarization converter is placed at a distance of $\lambda_o/4$ (λ_o is calculated with respect to 19.51 GHz) in the end-fire direction of MIMO antenna to obtain an orthogonal CP wave at the two frequency bands. The S-parameters of the four port CP MIMO antenna are shown in Figure 10(c) exhibiting a dual-band operation in the lower frequency band: $19.65 - 22.05$ GHz and upper frequency band: $29.25 - 30.35$ GHz. The MIMO antenna shows an isolation better than -20 dB among all the ports at both the operating frequency bands. The proposed CP antenna shows good MIMO performance with correlation coefficient (CC) less than 0.19 and diversity gain (DG) better than 0.97 at both the frequency bands. The four-port MIMO also agrees with polarization and spatial diversity, and the CP nature at lower and upper frequency bands can be interchanged by exciting the orthogonal ports. A prototype of both the two and four port CP MIMO antennas is fabricated and the measured. The CP bandwidths of 11.51% and 3.69% is obtained in the lower ($19.65 - 22.05$ GHz) and upper ($29.25 - 30.35$ GHz) frequency bands, respectively in four port CP MIMO antenna. The proposed antenna can be used for K/Ka-band: $29.5 - 30.0$ and $19.7 - 20.2$ GHz fixed satellite service as uplink and downlink frequencies, respectively.

Acknowledgements

All praises be to Allah, for His showers of blessings throughout my work to complete the research successfully.

I would like to express my sincere gratitude and appreciation to my research supervisor *Dr. Kushmanda Saurav*, Department of Electrical Engineering, Indian Institute of Technology (IIT) Jammu whose guidance, support and constant encouragement has been invaluable throughout this study and have made this an inspiring experience for me. His understanding and expertise in my area of research greatly improved the contents of this thesis. I am grateful for his helpful comments, suggestions and constructive criticism throughout this entire study. My thesis has benefited substantially from his insightful recommendations.

I would like to thank my supervisor *Prof. Shiban Kishen Koul*, Center for Applied Research in Electronics (CARE), Indian Institute of Technology Delhi for his technical advice at various stages during my research. His constant motivation and support has driven me towards the completion of this task. His exemplary management skills helped in the completion of several tasks on a fast track, which otherwise would have taken much longer time. He was always there to offer any kind of help during my stay here. His guidance instilled in me the potential of working on a research problem and coming to a fruitful solution out of it. It has been an honour to have him as the thesis supervisor and shall always indebted to him for being the saviour whenever I have been shrouded in any problem, be it professional or personal.

I would like to thank the Department of Electrical Engineering IIT Jammu for providing the Lab facilities and the financial support that permitted me to complete my thesis. A special words of mention deservedly for, *Dr. Archana Rajput*, *Dr. Alok Kumar Saxena*, *Dr. Amit Kumar Singh* and *Dr. Zamir Wani* whose well-entrenched knowledge have always improved my understanding of various topics in microwave research. The fruitful discussions with them helped me a lot in my research and academic work.

I would like to thank *Prof. Ananjan Basu* and *Prof. Mahesh P Abegoankar*, Center for Applied Research in Electronics, IIT Delhi who were the instructors during my course works at IIT Delhi. The inspiring lectures delivered by them, helped me in building a strong foundation of the basics of Electromagnetics and generated a keen interest to tackle research problems associated with Microwave Circuits and Antennas. My sincere gratitude also extends to all the members of Microwave Lab CARE, IIT Delhi for giving access to the laboratory and research facilities. Without their precious support it would not be possible to conduct this research.

I am thankful to my fellow labmates, *Mr. Mehran Manzoor*, *Mr. Javid Ahmad*, *Mr. Ankit Kumar Pandey*, *Mr. Gazali Bashir*, and *Ms. Suchitra Tiwari* for the stimulating discussions, and for all the fun we have had in the last three years. My colleagues in the lab have helped a lot in creating a good environment suitable for research activity. It truly has been very, very good time in this lab.

I have spent very nice time in IIT Jammu campus with my Ph.D. batchmates *Mr. Burhan Wafai*, *Mr. Mohit Pal*, *Mr. Suhaib*, *Mr. Tawseef Ahmad*, *Mr. Ajaz Ahmad*, *Mr. Jalil*, *Ms. Deebha Mumtaz*, *Ms Sadbhavna Thakur*, *Mrs. Ambreen Bashir*, *Ms. Ameena Girdhher* and *Ms. Sapna Thapar*. I thank them for their company and help during my stay here.

Last but not the least, I want to express deep gratitude towards my family members for their unconditional love, care, sacrifice and blessing throughout my studies. I am blessed with parents, *Haji Ghulam Hassan Sofi* and *Saleema Banoo*, who have brought me to where I am today. Thanks for your understanding, your never ending encouragement, and for always being there for me. Your support has meant more to me than you could possibly realize. I also acknowledge love, care and affection from my brother *Mr. Showkat Ahmad Sofi* and my sister-in-law *Mrs. Nargis* and their kids *Amaan* and *Aamina*. I also want to thank my younger brother *Dr. Feroz Ahmad Sofi* for being so supportive while I was working on my thesis.

Contents

List of Figures

List of Tables

List of Symbols

Symbol	Description
E	Electric field
H	Magnetic field
K	Electromagnetic wave vector
ε_r	Real part of permittivity of the dielectric
$tan\delta$	Loss tangent of the dielectric
σ	Conductivity
λ	Guided wavelength
λ_0	Free space wavelength
f_r	Resonance frequency
f_c	Centre frequency of the operating band
f_{cp}	Centre frequency of the circularly polarized operating band

List of Abbreviations

Abbreviation	Description
AR	Axial Ratio
ARBW	Axial Ratio Bandwidth
BW	Bandwidth
CP	Circularly Polarized
CPBW	Circularly Polarized Bandwidth
DBS	Direct Broadcasting Services
EBG	Electromagnetic band-gap Structure
EM	Electromagnetic
FDTD	Finite Difference Time domain
FEM	Finite Element Method
FSS	Frequency Selective Surface
GNSS	Global Navigation Satellite System
GPS	Global Positioning System
HPBW	Half Power Beamwidth
IBW	Impedance Bandwidth
LHCP	Left Handed Circularly Polarized
LP	Linearly Polarized
LTC	Linear to Circular
MIMO	Multiple Input Multiple Output
MoM	Method of moments
PCR	Polarization Conversion Ratio
RCS	Radar Cross-Section
RFID	Radio Frequency Identification
RHCP	Right Handed Circularly Polarized
SRR	Split Ring Resonator
WLAN	Wireless Local Area Network

Chapter 1

Introduction

An electromagnetic (EM) wave represents the synchronized oscillations of electric and magnetic fields with respect to time and position propagating at the speed of light through the vacuum. EM waves are formed when there is an acceleration or deceleration of the charged particles. EM wave requires no medium for propagation from point to point. EM wave is described in terms of photons in quantized form, which are massless discrete energy particles travelling with the speed of light through vacuum. Energy, momentum, and angular momentum are carried by EM waves away from their source and can be imparted to the matter with which they interact. Apart from the parameters of the EM wave such as frequency, wavelength, speed, energy, and momentum, polarization plays an important role. The time variation of direction and relative magnitude of the electric field vector of an EM wave at a fixed location in space is described by the polarization [1]. Polarization can also be defined as the trace followed by the tip of the electric field at a fixed location in space. Polarization plays a significant part in several applications like optical imaging, contrast imaging, optical sensing [2], and telecommunication [3]. Microwave antennas used for transmitting and receiving are inherently polarized i.e., they are capable to transmit (or receive) signals of a particular polarization only. For illustration, if one tries to receive a vertically polarized signal through the use of a horizontally polarized antenna, the magnitude of the received signal is drastically decreased. The polarization of the signal has to be changed to the preferred polarization for maximum reception through the antenna. In satellite communications polarization is used to twofold the channel capacity over a fixed frequency band. A single channel is used to broadcast the two signals in orthogonal polarization by selecting the receiving antenna for one and transmitting antenna for the

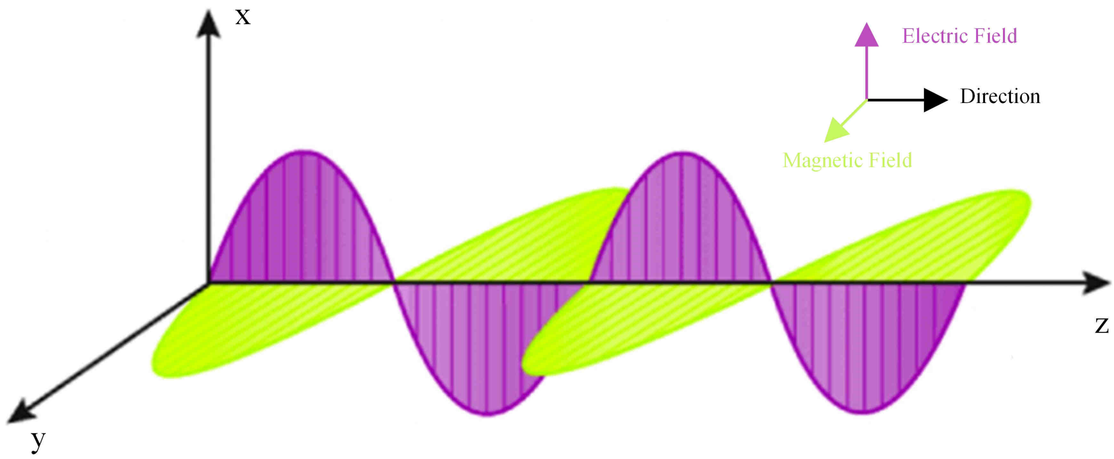

Figure 1.1: Linearly polarized (LP) wave [5].

.

other polarization, either signal can be selected without interference from the other [4]. Polarization is classified into three types.

1.0.1 Linear Polarization

If the field (electric or magnetic) of a time-harmonic EM wave at a given point in space is oriented along the same straight line at every instant of time, then a wave is said to be linearly polarized. Linear polarization is achieved if the electric or magnetic field vector owns: (a). Single component or (b). Two orthogonal linear components are either in phase or out of phase (180° or multiples of 180°) [1]. A linearly polarized wave is illustrated in Figure 1.1.

1.0.2 Circular Polarization

A time-harmonic wave is circularly polarized (CP) if, at a given point in space, the locus of the electric field vector traces a circular path with the variation in time [1]. Circular polarization is achieved if the electric field (or magnetic field) vector contains two orthogonal linear components with the same magnitude and phase difference that is an odd multiple of 90°. The sense of rotation of CP wave is determined by rotating the phase-leading component towards the phase lagging component and observing the field rotation as the wave travels away from the observer. If the rotation is clockwise, then the wave is right-hand (clockwise) circularly polarized (RHCP). If the rotation is

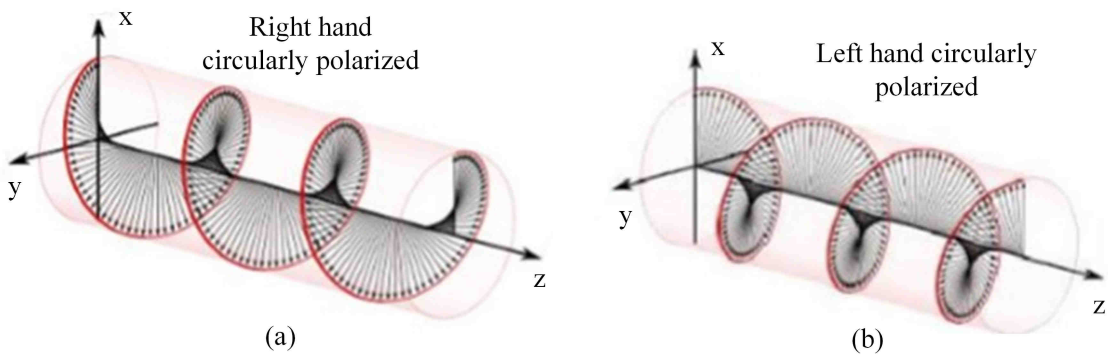

Figure 1.2: (a) Right-hand circularly polarized (RHCP) and (b) left-hand circularly polarized (LHCP) wave [5].

.

counterclockwise, then the wave is left-handed (counterclockwise) circularly polarized (LHCP). The RHCP and LHCP waves are depicted in Figure 1.2.

1.0.3 Elliptical Polarization

A time-harmonic wave is elliptically polarized if the locus of electric field (or magnetic field) forms an ellipse as a function of time at a fixed point in space [1]. The sense of rotation is determined in the same way as that of circular polarization. The elliptically polarized wave must possess two orthogonal linear components that may be of the same or different magnitude. If the linear components are not of the same magnitude, the time phase difference between the two components must not be 0° or multiple of 180° and if the components are of same magnitude, the time phase difference them must not be odd multiples of 90°. An elliptically polarized wave is shown in Figure 1.3(a).

1.1 Polarization Ellipse

The polarization of an EM wave can also be described using a polarization ellipse. In general, the curve traced by the electric field (or magnetic field) as a function of time is a tilted ellipse as shown in Figure 1.3(b) [1]. The axial ratio (AR) is defined as the ratio of the major-axis to the minor-axis of the ellipse as represented in (1.1).

$$AR = \frac{major-axis}{minor-axis} = \frac{OA}{OB}, 1 \leq AR \leq \infty \tag{1.1}$$

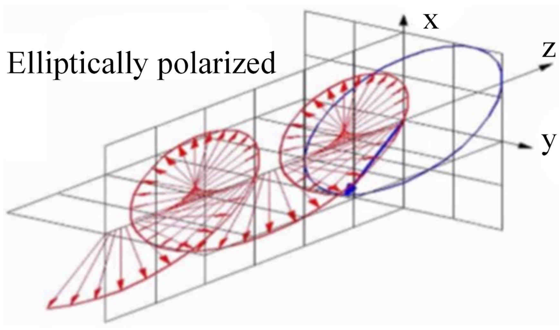

(a)

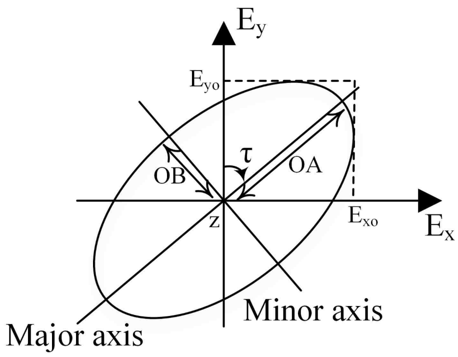

(b)

Figure 1.3: (a) Elliptically polarized wave [5] and (b) polarization ellipse.

.

where,

OA=$[1/2\{E_{xo}^2+E_{yo}^2+[E_{xo}^4+E_{yo}^4+2E_{xo}^2\ E_{yo}^2\ \cos(2\triangle\phi)^{1/2}\}]^{1/2}$

OB=$[1/2\{E_{xo}^2+E_{yo}^2$-$[E_{xo}^4+E_{yo}^4+2E_{xo}^2\ E_{yo}^2\ \cos(2\triangle\phi)^{1/2}\}]^{1/2}$

The tilt of ellipse, relative to the y-axis is represented by angle τ given by (1.2)

$$\tau = \frac{\pi}{2} - \frac{1}{2}\tan^{-1}\left[\frac{2E_{xo}E_{yo}}{E_{xo}^2 - E_{yo}^2}\cos(\triangle\phi)\right] \tag{1.2}$$

A general form of the polarization ellipse is depicted in Figure 1.3(b). The angle between the major-axis and the E_y-axis is denoted by τ. The ratio of major to minor-axis referred to as ellipticity is the substitute of eccentricity. The ellipticity angle is expressed as, $\chi = \tan^{-1}$ (OB/OA). For linear and circular polarization ellipticity e of infinity (∞) and unity (1) (or χ of zero and 45°) respectively is obtained [6].

1.2 Jones Calculus for Polarization of the Electromagnetic Waves

Jones calculus, discovered by R. C. Jones in 1941 can be used to describe the behaviour of a polarized EM wave. An EM wave is represented by a Jones vector, while the linear optical elements are represented by Jones matrices [3]. The polarization of the EM wave after passing through an optical element is found by taking the product of the Jones matrix of the optical element and the Jones vector of the incident wave. Let us suppose that a monochromatic plane wave is travelling in the positive z-direction, with the angular frequency of ω and wave vector (0,0,k), where the wave number k= ω/c. The electric and magnetic fields E and H are orthogonal to k at each point and both lie in the plane transverse to the direction of wave propagation k [3].

$$\begin{pmatrix} E_x(z,t) \\ E_y(z,t) \end{pmatrix} = \begin{pmatrix} E_{ox}e^{i(kz-\omega t+\phi_x)} \\ E_{oy}e^{i(kz-\omega t+\phi_y)} \end{pmatrix} = \begin{pmatrix} E_{ox}e^{i\phi_x} \\ E_{oy}e^{i\phi_y} \end{pmatrix} e^{i(kz-\omega t)} \tag{1.3}$$

The amplitude and phase of the electric field in the x- and y-direction are represented by the Jones vector. The intensity of the EM wave is proportional to the sum of the squares of the absolute values of the two components, E_{ox} and E_{oy}, of the Jones vector [6]. The intensity is commonly normalized to 1 at the starting point to simplify calculations. The Jones vector for a linear polarization along the x-axis is $\begin{pmatrix} 1 & 0 \end{pmatrix}^T$ while for y-polarization it becomes $\begin{pmatrix} 0 & 1 \end{pmatrix}^T$ where T stands for transpose. Similarly, the Jones vector for RHCP wave is: $\frac{1}{\sqrt{2}}\begin{pmatrix} 1 \\ i \end{pmatrix}$, while for LHCP wave $+i$ is replaced by $-i$.

1.3 Birefringence

Birefringent materials are characterized by the property that their refractive index is dependent on polarization and direction of propagation of an EM wave [7]. The feature of birefringence is due to the anisotropy of the structure and is generally evaluated as the maximum difference between refractive indices realized by the material for different propagation directions or polarizations. For example, non-cubic crystal structures are often birefringent, as are plastics under mechanical stress. The double refraction phenomenon arises due to the birefringence in the material where an incident ray of light is split by polarization into two rays which marginally differ in their path.

Uniaxial is the basic form of birefringence. Uniaxial optical anisotropy of a material is governed in a single direction, whereas all directions perpendicular to it (or at a given angle to it) are optically equivalent [8]. Hence, rotating the material around this axis does not show any effect on its optical behavior and is known as the optic axis of the material. Polarization of light perpendicular to the optic axis is governed by a refractive index called ordinary refractive index (n_o) while the EM wave aligned in the direction of optic axis views an optical index called extraordinary refractive index (n_e). The difference between the two is usually referred to as birefringence ($\triangle n$) [9]:

$$\triangle n = n_o - n_e \tag{1.4}$$

The orthogonal components travel with different speeds due to the difference in the refractive index that causes phase difference resulting in the polarization conversion of the emerging wave. Polarization conversion can be accomplished based on the phase difference acquired while going through an optically anisotropic material.

1.4 Polarization conversion of Electromagnetic waves

The polarization of EM waves can be altered using typical methods including the use of birefringent material like quartz crystal [7], Faraday-effect [10]. In birefringent materials the phase of one of the linear components is delayed compared to that of the other orthogonal component, thereby manipulating the polarization state of the EM wave. An LP wave is converted into a circularly or elliptically polarized wave if the phase of one of the components as measured at the output of the birefringent material is lagging by odd multiples of 90° with respect to the other orthogonal component. However, a CP wave is obtained if the two orthogonal components have the same magnitude and the phase difference is 90°. If the two orthogonal components are not of equal magnitude and have a phase difference of 90° or magnitude is similar but phase difference is neither 90° nor 180° then the resulting wave will be elliptically polarized. An LP wave is transformed into its orthogonal LP wave if the birefringent material provides a phase delay of 180°. For obtaining a definite delay, the birefringent material is required to have thickness given by

$$d = \triangle\phi\lambda/2\pi \tag{1.5}$$

where, d represents the thickness of the material, $\triangle\phi$ denotes the phase difference brought by the material, and λ is the free space wavelength of the wave inside the material [9]. From (1.5) one can interpret that thick or bulky materials are required for modifying the polarization at higher wavelengths and vice versa. Furthermore, from (1.5) the thickness of the material should be half of the operating wavelength of the EM wave for a horizontal to vertical polarization conversion to take place.

The typical methods employed to carry out polarization conversion are narrow band, use bulkier materials and also attain polarization conversion at particular wavelengths. Furthermore, polarization conversion using these techniques is heavily dependent on the incidence angle of the incoming wave. So, smaller bandwidth and angle of incidence dependence make these conventional methods less suitable in modern polarization control devices [11]. To overcome these limitations, microwave engineers and scientists have come up with structures called frequency selective surfaces (FSS) [12] − [14], and metasurfaces [15] − [19], which can manipulate the polarization state of electromagnetic waves. The FSS are discussed in the next section. Most often, polarization control is achieved with waveplates such as a quarter-wave plate [20]. For a quarter-wave plate, the transmitted phase difference between two orthogonal electric field components is a quarter of the wavelength (90°). When an incident field is linearly polarized at 45° relative to its crystal axes, the quarter-wave plate converts the transmitted field to circular polarization, which has applications in satellite communication and rain clutter suppression [20].

1.5 Frequency Selective Surface (FSS)

Frequency selective surfaces (FSS) are the assembly of one- or two-dimensional identical elements (patch or aperture) called unit-cells in periodic arrangement operating as spatial filters to exhibit frequency filtering properties similar to that of conventional microwave filters. The behaviour of FSS depends upon the frequency, angle of incidence, and polarization of the incident wave. The FSS can function as high-pass, low-pass, bandpass, and bandstop filters. These properties allow the FSS to properly manage the propagation of electromagnetic energy [21]. The basic fundamental behind the physics of FSS structure is directly derived from the analysis of diffraction gratings in optics, which is used to decompose a beam of non-monochromatic light into its spectral orders. The study of FSS structures and their relation to electromagnetic waves earned consideration in the mid-1960s. The patch/aperture-type FSS ideally perform total reflection and transmission, respectively, in the proximity of its fundamental resonance frequency. The FSS unit-cell geometry, size, inter-element spacing, dielectric substrate, which build up the unit-cell element, determines the overall resonance frequency, bandwidth, and dependency on the angle of incidence as well as the polarization of the planar incoming wave[22]. Thus, to design an FSS structure, the appropriate choice of geometrical parameters is of primary importance for the desired frequency response, because these parameters have the potential to remarkably vary the frequency response.

1.5.1 Operating Theory of FSS

According to the circuit theory, FSS structures (capacitive and inductive) also called spatial filters and microwave filters are analogous to each other. The basic mechanism of operation of FSS has been explained by Munk in detail [21]. When an EM wave strikes the FSS structure, it stimulates the electric currents into the elements of the FSS. The strength of the electric current produced depends on the extent of coupling energy among the FSS elements. The electric currents generated act as EM sources and constitute scattered fields. The resultant field is the combination of the incident and scattered fields. Therefore, the appropriate currents and field response can be accordingly achieved from properly designed elements and generate the filter response. The physical mechanism of the FSS filtering characteristics is explained through a dipole FSS structure upon which an incident wave strikes in two ways as shown in Figure 1.4. The incident plane wave in the first case as shown in Figure 1.4(a) strikes the dipole FSS in such a manner that the FSS structure is orthogonal to the propagation vector and the axis of the dipole is aligned with the electric field [23]. The electrons gain energy and oscillate due to the electric field, a portion of the incident wave energy is translated into kinetic energy and gives rise to the re-radiated waves/energy. The cancellation of the plane wave occurs as the re-radiated and incident waves are out of phase on the right side of the FSS structure. The re-radiated waves on the left side of the FSS constitute the reflected wave, resulting in low transmittance through the FSS filter [24]. In Figure 1.4(b), the electric field vector is orthogonal to the FSS dipole structure. When an EM wave is incident on the FSS structure in this case, the electrons do not re-radiate because of their inability to oscillate up and down. Therefore, the FSS structure remains invisible to the incident plane wave and total transmission occurs or transmittance will be higher [25]. Based on the basic principles of operation, FSS can be divided into two groups: resonant and non-resonant structures.

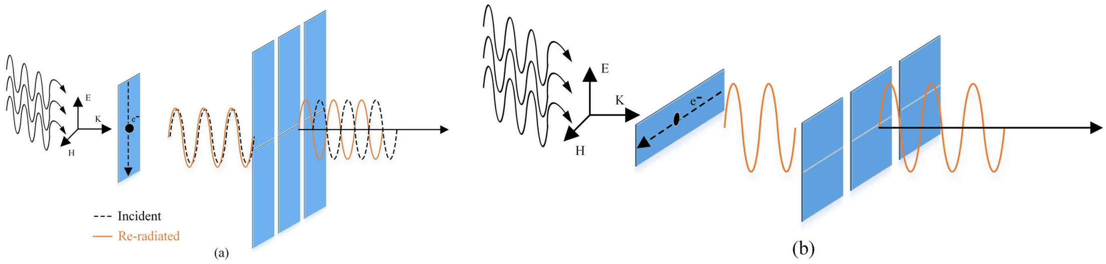

Figure 1.4: Filtering mechanism of FSS for E-vector (a) parallel and (b) orthogonal to the metallic dipole [22].

1.5.2 Resonant FSS

Essentially, the FSS structure operates at its resonance frequency. The single layer FSS structures that exhibit their frequency dependence are termed as resonant FSS. Nonetheless, resonant FSS can be designed in a multilayer configuration. The array of patch elements and apertures (slots) are two primary groups of resonant FSS. The array of patch elements are metallic in regular configuration and can be modeled by electric currents, while aperture arrays are slots in metallic surfaces in periodic form that can be modeled by magnetic currents [21]. Both the groups of resonant FSS can present different behaviour with respect to frequency, essentially patch type element display bandstop characteristics in comparison to aperture type which perform similar to that of bandpass filters [21].

The choice of selecting a particular element may be of most interest when designing a bandstop or bandpass FSS. The shape of FSS is selected based on the application requirements like dependence of incidence, polarization angle of the incident plane wave, and bandwidth. In general, all FSS are eventually supported by the dielectric substrate which has a pronouncing effect on the bandwidth of the FSS. The FSS element can attain various shapes which are shown in Figure 1.5. The FSS elements can be classified into three classes according to [21]. The first group is the centre-connected FSSs, such as the square spiral elements, the four-legged elements, the Jerusalem cross, and the three-legged elements, as shown in Figure 1.5. The loop type elements like the hexagonal rings, the circular ring, the square rings, the three and four-legged loaded elements are grouped in another class called loop type. The solid interior patch FSSs, such as square, circular paths, and hexagonal patches are grouped in another set. Finally, group four represents the designs obtained by combining the other group elements. The resonant frequency is located roughly at a frequency in which the electrical length of center-connected elements

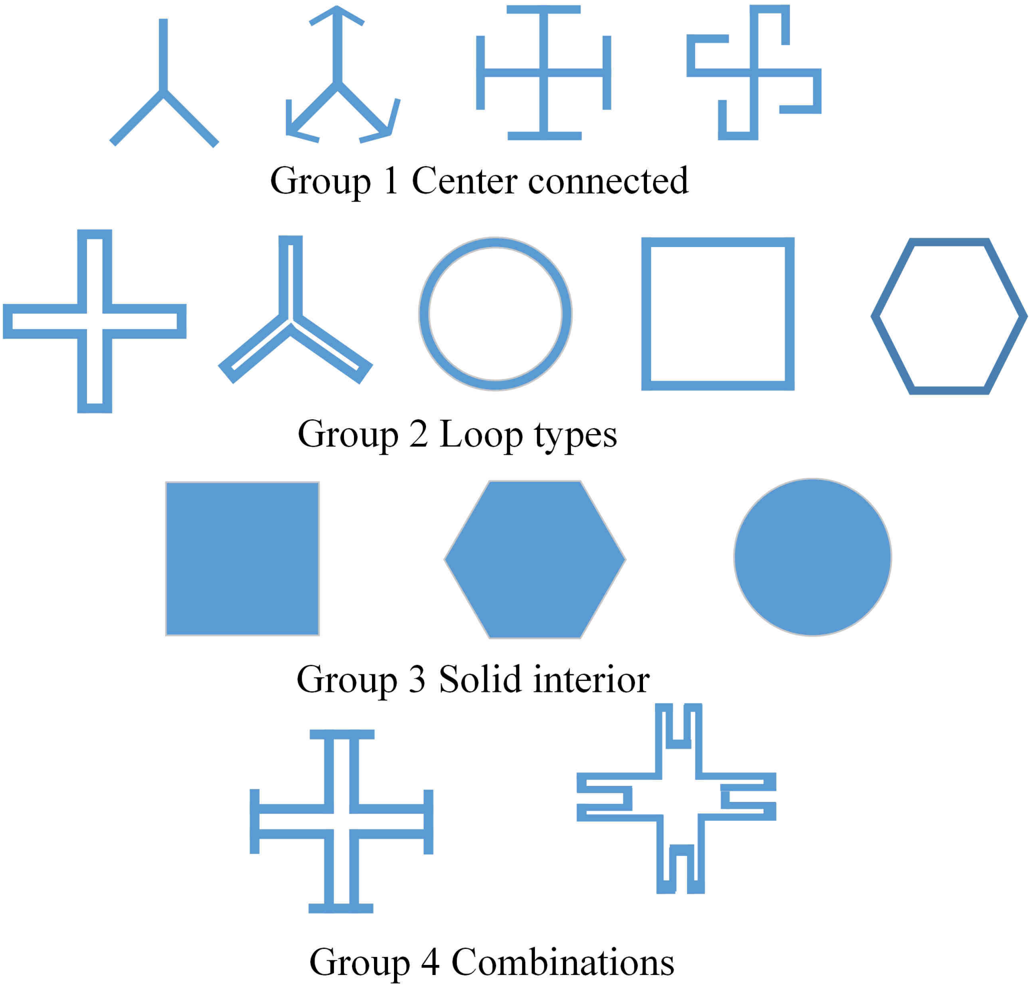

Figure 1.5: Element shapes of FSS [21].

is $\lambda/2$, the average circumference of the loop and solid type FSS is around λ [21]. The resonant frequency of the combination is somehow more complicated and depends on the particular shape of the elements.

1.5.3 Non-Resonant FSS

FSS structures that consist of capacitive patches and inductive grids on different sides of the substrate forming a parallel LC circuit are referred to as non-resonant FSS. In contrary to the resonant FSS, elements of non-resonant FSS do not exhibit resonant property when they are isolated from periodic structure [25]. In non-resonant FSS at least two metallic layers composed of capacitive patches and inductive layers are required in order to obtain the desired frequency response. One of the examples of non-resonant FSS is shown in Figure 1.6. The advantage of non-resonant FSS over the resonant ones is that the former have simpler design procedures and smaller periodicity.

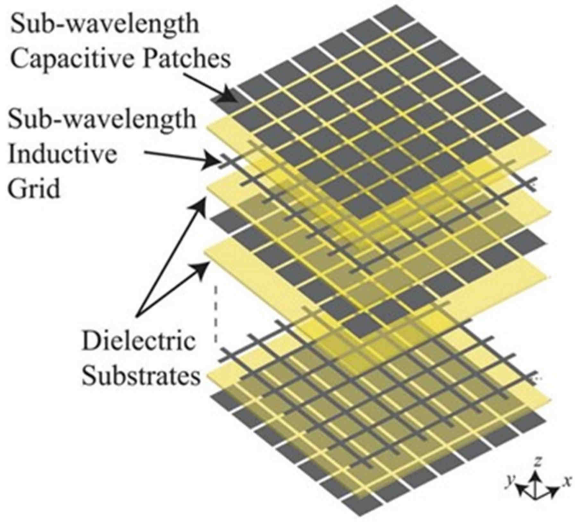

Figure 1.6: An example of non- resonant FSS [26].

FSS has largely been studied for the past six decades and a variety of FSS based at microwave and optical frequencies structures have emerged. In past FSS has been generally used with antennas [27] − [32], including diplexers for quasi-optical microwave devices [33], resonant beam splitters, and antenna radomes [34], [35]. Nowadays, FSSs are being employed in dichroic sub-reflectors [36], radio frequency identification (RFID) [37], lens antennas [38], absorbers and rasorbers [39] − [42], cloaks [43], [44], sensors [45] − [47], polarizers [48] − [53] and electromagnetic interference [54]. Apart from these some brief applications of FSS in various fields are shown in Figure 1.7 [55], [56]. The performance of FSS is largely determined by the requirement of compact size and stability with respect to oblique incidence dependence and the polarization of EM wave. Thus, the FSS design require improving these performance parameters.

FSS are inherently narrow band and they do not provide adequate spatial filtering response. Extensive research is going on to miniaturize the FSSs and improve the frequency response with broader bandwidth (BW) at higher incidence angles and dual polarization. Single layered FSS structures provide unstable performance as the incidence angle of EM wave varies. Multilayered FSS offering greater resilience of varying parameters for desired performance has been reported to reduce the constraints of single layer FSS [57] − [62]. For reducing the size of antennas and arrays, FSS based on fractal elements and miniaturized arrays are introduced [63] − [65]. Active and 3-D FSS designs have opened new windows for scientists and engineers in microwave technology [66] − [69]. Furthermore, embedded FSS (with inserted metallic rods and plates based on stepped-impedance

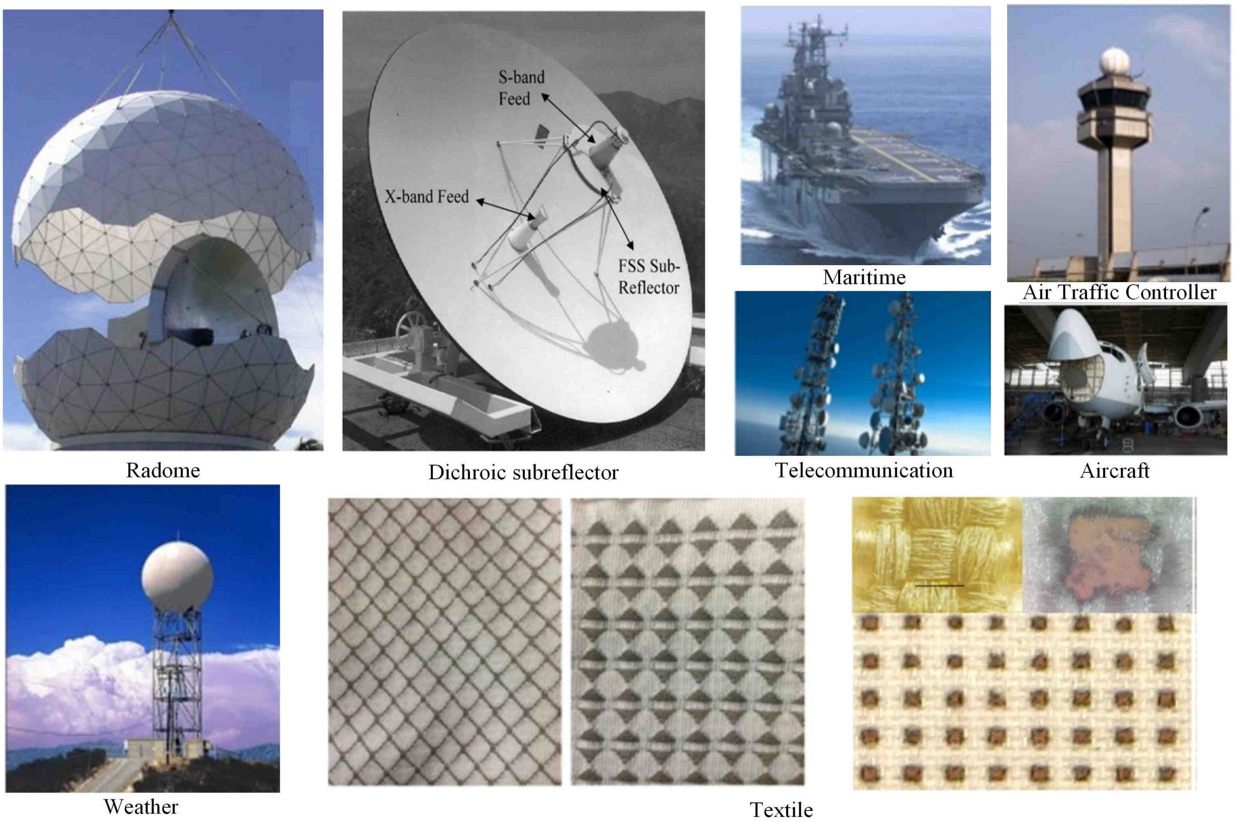

Figure 1.7: Appplications of FSS in various fields [35]−[38].

resonator) [57] − [70], integrated FSS and Electromagnetic band-gap structures (EBG) [53], [54], [57] − [69], and metamaterial inspired FSSs [57]−[72] are the most current progresses achieved by microwave researchers. FSS has been studied through approximate analytical techniques, which involve equivalent circuit method to analyze the transmission characteristics. However, with the development of new complex designs, state-of-the-art electromagnetic solvers based on numerical methods like finite element method (FEM), method of moments (MoM), finite difference time domain method (FDTD), and the integral equation (boundary element) method (IEM/BEM) [73] − [76] use unit cell and periodic boundary conditions (PBC) allowing the design analysis quite straightforward. A well-known technique is IEM/BEM used in combination with the MoM [77] − [78].

1.6 Measurement of FSS

The reflection and transmission properties of FSS can be measured using several methods available in the literature [79], [80]. The free space measurement setup followed to carry out the measurement of FSS in this thesis is shown in Figure 1.8. A pair of standard

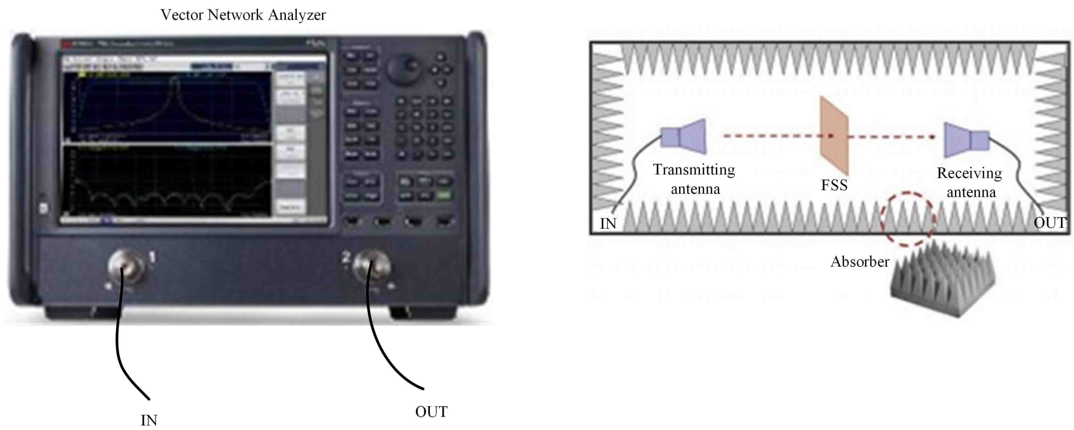

Figure 1.8: Measurement set up of FSS.

gain horn antennas and a vector network analyzer are used. The pair of standard gain horn antennas are facing each other with the same polarization. The FSS structure to be characterized is placed in between the antennas. The distance from the antenna and FSS structure should be large enough to meet the far-field criteria given by (Distance > $2D^2/\lambda$ criteria) [81], where D is the largest antenna dimension and λ is the free space wavelength at the resonant frequency. Therefore, a plane wave can be assumed to be arriving at the FSS. The setup to measure transmission characteristics is shown in Figure 1.9(a). Radio-frequency absorbing materials are employed to overcome diffraction and spillover around the edges. Calibration can be carried out before measurement to ensure the measurement accuracy.

The transmission coefficient without the FSS sample is first measured as the reference (S_{21} =1 or 0 dB) and when the FSS structure is under test, the measured transmission coefficient is normalized with respect to the reference. The measurement of transmission characteristics under oblique incidence is ensured by rotating the FSS structure to the angle of interest. Under oblique incidence the measurement is not as good as normal incidence due to the finite size of the FSS. The size of the FSS under test should ideally be large as possible. As the measurement is relative (compared with the response without the FSS), the size of the FSS greater than the aperture of the standard gain horn antenna used for measurement can give good results.

For measurement of reflection properties of the FSS structure, a pair of standard gain horn antennas is used acting as the transmitter and the receiver, respectively as shown in Figure 1.9(b). Radio-frequency absorbing material is used between the two antennas to avoid the direct coupling between the two. The reflection coefficient is first measured

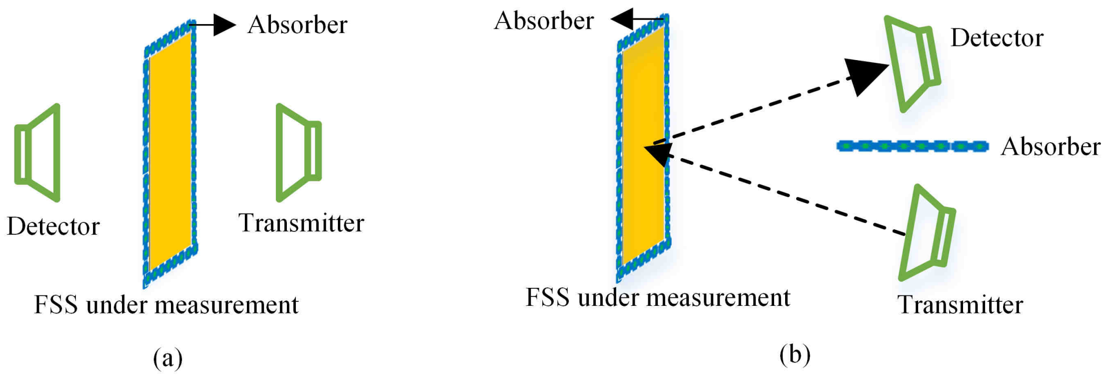

Figure 1.9: Experiment setup to measure (a) transmission and (b) reflection coefficient.

with a plane metallic sheet for normalization purposes to ensure $S_{11} = 1$ or 0 dB. The measured reflection coefficient of the FSS under test is normalized with respect to the reference. Oblique incidence measurement is realized by moving the transmitting and receiving antenna in a circle so that each subtends an angle of interest with the FSS.

1.7 Literature Survey on Polarization Converters based on FSS

The polarization converting devices are used to modify and manage the polarization of an EM wave. When an LP incident wave strikes a polarization converter, it passes through or is reflected, a cross- or circularly polarized reflected/transmitted wave can be achieved. To obtain a linear-to-circular (LTC) polarization conversion the target is to acquire transmission or reflection for two incident orthogonal linear components (of a LP incident wave) equal in magnitude, but with a $\pm 90°$ phase difference between the two components [82]. Polarization converters are designed as periodic composite materials on low loss dielectric substrate upon which an array of metallic unit-cells are printed. Polarization converters are polarization dependent and can be realized using the FSS, and are also sometimes described as metasurface [83].

Different configurations of the unit cell of polarization converter has been used in different frequency ranges to achieve polarization conversion [84] $-$ [93]. Polarization converters operate in transmission and reflection mode based on whether the incident wave on the converter is transmitted or reflected. Both types of the polarization converters have been studied in the literature for polarization conversion. The polarization conversion of an

EM wave is achieved through the use of an anisotropic unit-cell [84]. The geometrical configuration of an anisotropic cell is different along different axes. Due to the anisotropy in the structure, the response to the incident LP wave is different along different directions. The anisotropic FSS is used to achieve LTC polarization conversion where two linear orthogonal components of the incident wave are reflected with equal magnitude and 90° phase difference. The reflected wave can be RHCP or LHCP based on the sign of the phase difference of the reflected wave. Reflective anisotropic circular polarizing metasurface acts as a quarter-wave plate [85] as it converts linear polarization into circular and circular polarization into linear polarization similar to that of a quarter-wave plate. Many polarization converters employing anisotropic unit-cell geometries have been reported in the literature [86] − [88]. The chiral geometries have also been adopted to attain polarization conversion [89] − [93]. The property of chiral geometries is the lack of mirror symmetry, where the chiral shape cannot overlap on its mirror image. Broadly polarization converters can be classified into two major groups:

1. Reflection Type Polarization Converters
2. Transmission Type Polarization Converters

1.7.1 Reflection Type Polarization Converters

The reflection-type polarization converters transform a LP incident wave into a reflected wave having two orthogonal components with equal amplitude and phase difference of 90°. Reflective polarization converters comprising both the linear-to-linear and linear-to-circular available in the literature are explored in this section. The reflection type polarization converters examined here are composed of the metallic printed patterns on top of a substrate and a ground plane on the other side.

1.7.1.1 Linear-to-Linear Reflective Polarization Converters

The reflection type linear-to-linear polarization converter capable of transforming an incident LP wave to its orthogonal polarization are reported in [94] − [97]. In [94] a linear-to-linear reflective polarization primarily used to lower the RCS of a slot array antenna is reported. The unit-cell of the polarization converter is composed of a fishbone-like design printed on a grounded substrate as shown in Figure 1.10(a). The polarization converter is excited by a horizontal LP incident wave to generate three plasmon resonances. The

3-dB bandwidth of 104.35% is obtained for this polarization converter over which a horizontal LP incident wave is converted to vertical LP wave. A double v-shaped linear to cross reflective polarization converter is reported in [95] as shown in Figure 1.10(b). The electric and magnetic features of the unit cell facilitate four plasmon resonances leading to broaden the bandwidth of orthogonal reflections. The polarization converter achieves ultra-wideband performance from $12.4 - 27.96$ GHz attaining a PCR of more than 90%. A graphene-based reflective cross polarization converter operating in $2.1 - 2.9$ THz frequency range is reported in [96]. The same polarization converter can transform a CP incident wave to its orthogonal CP after reflection from the converter. The polarization converter is composed of a half elliptical ring loaded with strips as shown in Figure 1.10(c) and a gold layer. The PCR can be controlled by changing the chemical potential of graphene and ranges from 2% to 98% and 60% to 98% for LP and CP incident wave, respectively. An ultrathin reflective polarization rotator composed of oval shaped unit-cell shown in Figure 1.10(d) excites two plasmon resonances to enlarge the cross-polarization reflection bandwidth [97]. The PCR greater than 68.6% is achieved in the frequency band: $8.0 - 18.0$ GHz with an angular stability of 30° for oblique incidence angle. The wideband behaviour can be attributed to simultaneous excitation of of electric and magnetic resonances.

The reflective polarization converter in [98] is based on multiple plasmon resonances to realize a high polarization conversion ratio (PCR). The polarization converter consists of asymmetric resonators in the shape of double split-rings on a grounded substrate as depicted in Figure1.10(e). The polarization converter is excited by vertical LP wave. The perpendicular component of the incident field gives rise to two resonance eigen-modes and the third resonance eigen-mode is generated when the field is parallel to the split gap. The location of resonant frequencies at 9.57 GHz, 10.6 GHz, and 12.02 GHz can be shifted by changing the dimensions of the unit-cell. The PCR of 99% is attained by the polarization converter. In [99]] four plasmon resonances are generated in a double-arrow (Figure1.10(f)) shaped grounded type unit-cell of the reflective polarization converter. The four resonances are located at 6.8 GHz, 12.17 GHz, 15.45 GHz, and 23.13 GHz. The first two and last two eigen-mode resonances are respectively generated by the perpendicular and parallel component of the incident vertical LP wave. A PCR of 50% is exhibited by the polarization converter.

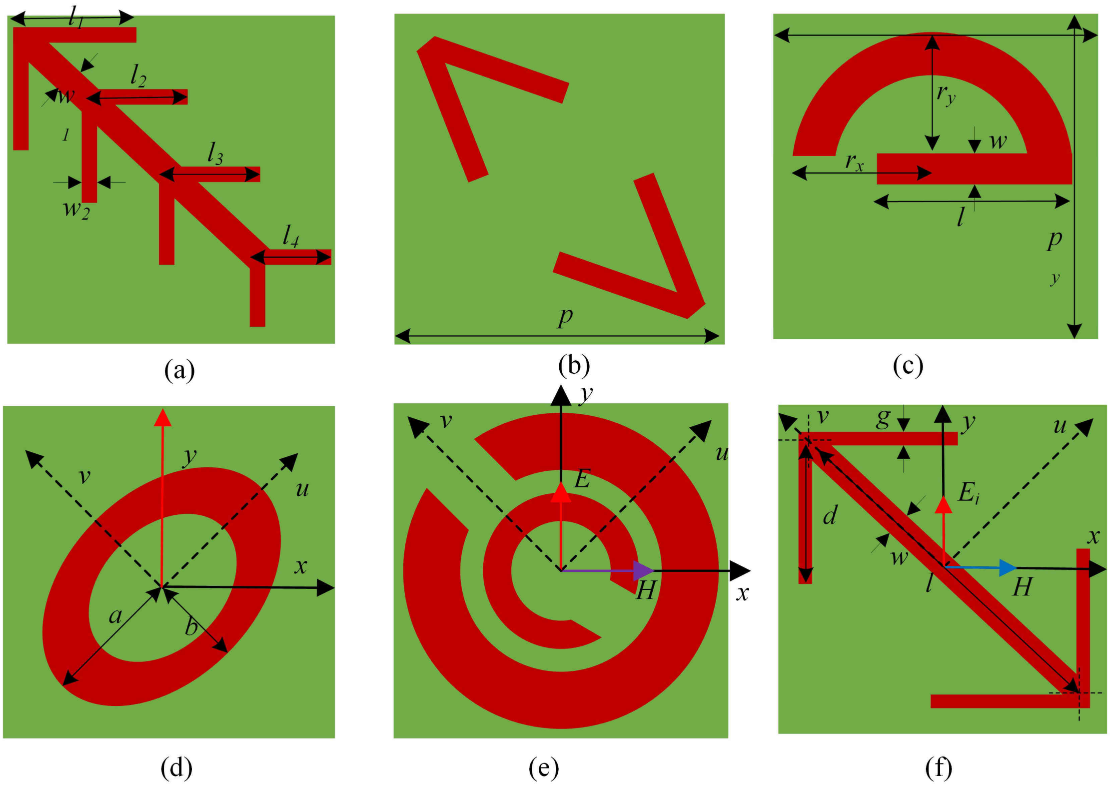

Figure 1.10: Various reflection type linear-to-linear polarization converters (a) fishbone [94], (b) double-v [95], (c) half-elliptical ring [96], (d) oval shape [97], (e) double split-ring [98], and (f) double-arrow [99].

1.7.1.2 Linear-to-Circular Reflective Polarization Converters

Reflective linear-to-linear polarization converter composed of a pair of meander lines and a metallic strip backed by the grounded substrate is reported in [100]. The anisotropy characteristics of the converter control the reflection characteristics of two orthogonal LP incident waves for linear-to-circular polarization conversion. The converter achieves a 3-dB axial ratio bandwidth of 60% with angular stability up to 60° for a linear-to-circular polarization. A dual-band linear-to-circular polarization converter working in reflection mode is reported in [101]. The polarizer consists of rectangular patches as shown in Figure 1.11(a) above a metallic grounded dielectric substrate. The distinct feature of this polarizer is the conversion of the LP incident plane wave into the CP wave in one of the frequency bands of operation and orthogonal CP with respect to that of the first band in the second band of operation. This feature is desirable in satellite communication as transmit and receive signals are preferred to have orthogonal polarization. A dual-band reflective low-profile LTC polarization converter operating in the Ku band is reported in [102], where a 45° incident LP wave is converted into the orthogonal CP at lower and upper-frequency band of operation using the unit-cell as shown in Figure 1.11(b). The

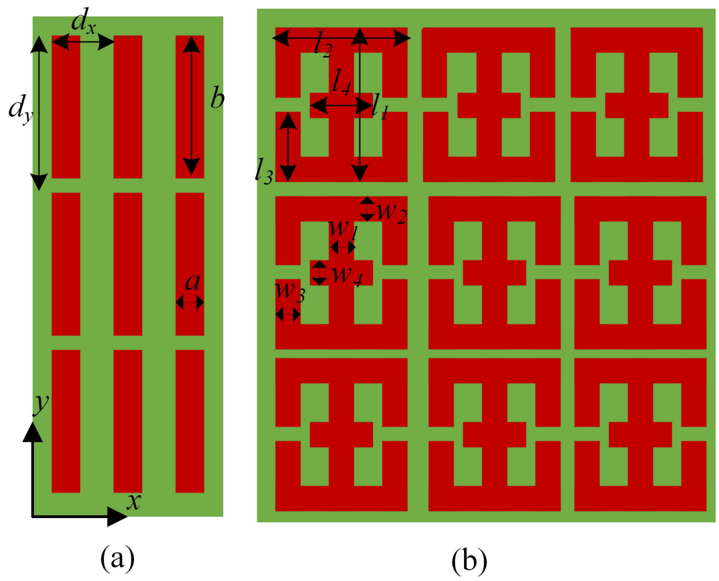

Figure 1.11: Reflection type linear-to-circular polarization converters (a) rectangular patch [101] and (b) dipole and metal strip [102].

compactness in the design is achieved by manipulating the TE and TM polarized waves.

A reflective linear-to-linear and LTC polarization conversion at lower and upper-frequency bands, respectively, use a pair of meander lines and a metal strip on a metallic-backed substrate [103] as shown in Figure 1.12(a). The converter achieves a fractional bandwidth of 13.0% from $13.70 - 15.60$ GHz for a LTC polarization. A LTC polarization converter with ARBW extending from $4.7 - 21.7$ GHz is reported in [104]. The LTC polarization conversion takes place by virtue of metallic vias inserted below the superstate as shown in Figure 1.12(b), thereby connecting the top metal and the ground plane of the unit-cell. A dual-band reflective polarization converter, transforming an LP wave into an orthogonal LP in the frequency bands $4.40 - 5.30$ GHz and $9.45 - 13.60$ GHz and incident LP into the CP in the frequency bands $4.47 - 5.35$ GHz and $9.57 - 13.57$ GHz with the same sense of polarization. The polarization converter is composed of a concentric rectangular loop and the metallic patch [105] as shown in Figure 1.12(c) showing a PCR of greater than 86% in all four bands.

A polygon-based reflective LTC polarization converter with broadband performance is reported in [106]. The unit cell of the polarization converter is shown in Figure 1.12(d). The TE and TM LP waves are converted to LHCP and RHCP, respectively. A 46% ARBW and angular stability up to 30° is exhibited by the polarization converter for both the polarized waves. Linear-to-circular and linear-to-linear polarization converter using Jerusalem type unit-cell as shown in Figure 1.12(e) is reported in [107]. The polarization

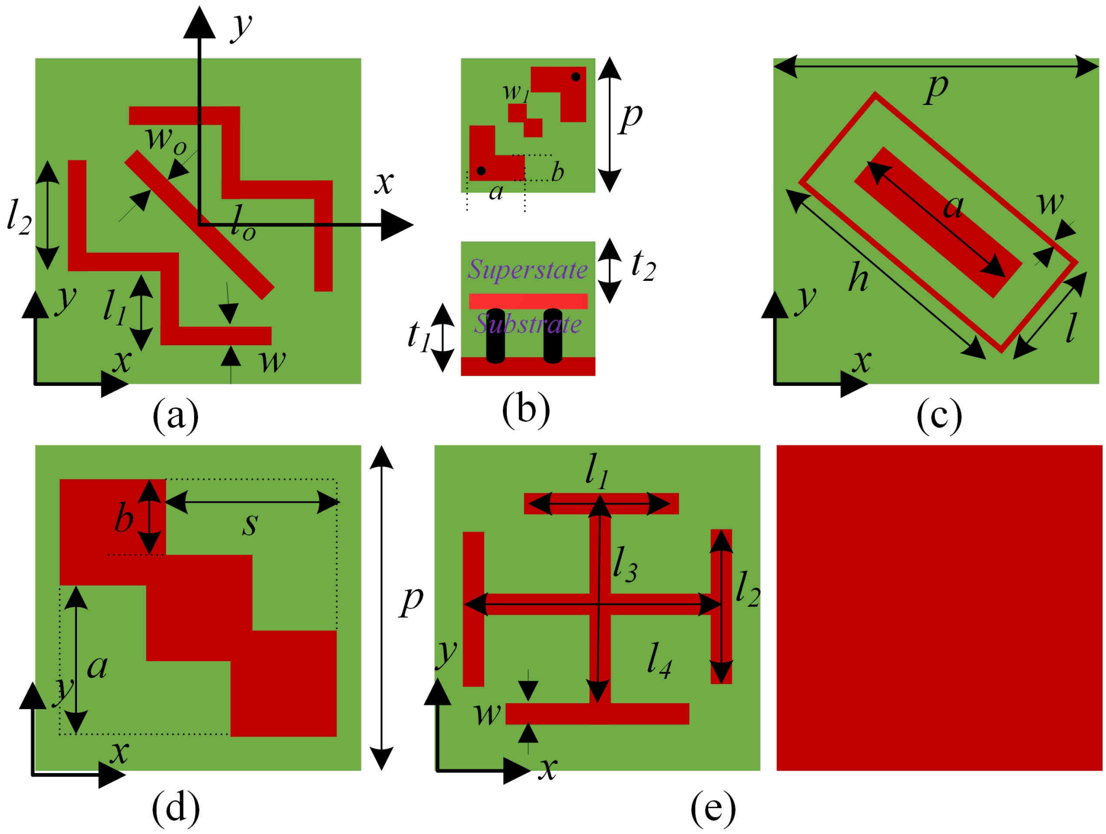

Figure 1.12: Some reflection type linear-to-circular polarization converter (a) Meander line and metal strip [103], (b) L-shaped strips and metal vias [104], (c) rectangular loop and metallic patch [105], (d) polygon type [106], and (e) Jerusalem type [107].

converter is single-layered and achieves a 25% ARBW. A 45° aligned incident LP wave is used to excite the polarization converter which consists of two orthogonal components. The dimensions l_3 and l_4 are used to obtain the reflected CP or orthogonal LP through the adjustment of phases of two orthogonal components.

1.7.2 Transmission Type Polarization Converters

In this section polarization converters working in transmission mode performing linear-to-linear and linear-to-circular polarization conversion are investigated. The transmission-type polarization converters transmit a wave having orthogonal components with equal amplitude and phase difference of 90°.

1.7.2.1 Linear-to-Linear Transmission Type Polarization Converters

Linear to cross- polarization converter composed of an array of dielectric substrate sandwiched in artificial structures (Figure 1.13(a)) where the two vias connect the top and bottom metallic layers is reported in [108]. The converter exhibits near unity polarization conversion efficiency and reaches maximum of 98.6% at 8.79 GHz. A two substrate layered linear-to-cross polarization converter is reported in [109]. The unit-cell is composed of cut strips arranged in a square shape as shown in Figure 1.13(b). Four identical cut strips form the top layer and the bottom layer on the lower substrate is the mirror image of the top layer across the horizontal plane. The polarizer is excited by an LP incident wave. The magnetic field in the four cut strips excites the magnetic dipoles which are heavily coupled to each other. The coupling results in the transmission of cross polarization. The polarization conversion efficiency exhibited by the polarization converter is about 90%. A two substrate layer linear to cross- polarization converter working in transmission mode is described in [110]. The unit cell consists of an asymmetric split ring and its 90° rotated counterpart as shown in Figure 1.13(c) on the top and bottom substrate, respectively. The polarizer attains 58% bandwidth with negligible co-polarization transmission. A three substrate layer based polarization converter based on a split-ring resonator [111] is reported, where each layer is rotated by 45° with respect to its previous layer as shown in Figure 1.13(d). A horizontal LP incident plane wave excites the polarization converter which after transmission gets converted into a vertical LP wave. The converter achieves 24% and 96% cross polarization conversion bandwidth and PCR, respectively. A horizontally LP incident wave is converted into a vertically polarized transmitted wave.

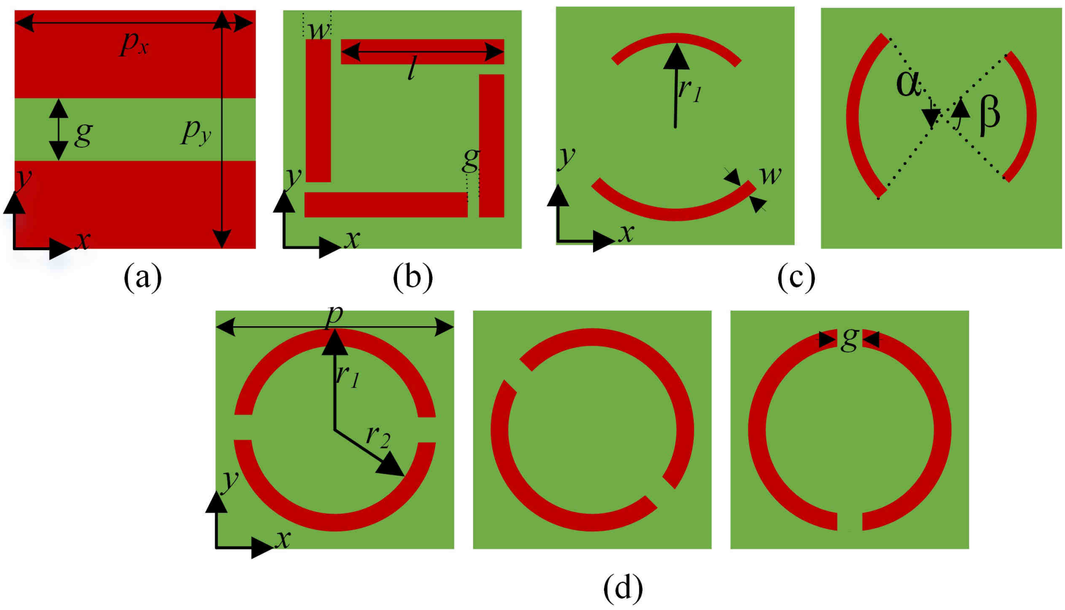

Figure 1.13: Some transmission type linear-to-linear polarization converters (a) dielectric slab [108], (b) cut strip [109], (c) asymmetric split-ring [110] and (d) split-ring resonator [111].

1.7.2.2 Linear-to-Circular Transmission Type Polarization Converters

Meander line polarizer [112] − [115] first realized in 1966 at the Stanford Research Institute uses a single [112], [113], and multilayer [114], [115] structure to convert an incident LP wave to a CP wave. The single-layer design is narrowband and subsequently the bandwidth is improved using a multilayer [114] configuration. In [114] a meander line-based design is modified into a three-layered structure with spacing of $\lambda/8$ between the layers to perform LTC polarization conversion over a wide bandwidth. The array of meander lines presents broadband shunt inductive and capacitive property to the incident wave [116]. The operating principle of meander line polarizer can be explained by resolving the incident wave (E_V) into two equal and in phase components E_L and E_C as shown in Figure 1.14(a). The parallel and perpendicular component of the incident field pass through a broadband shunt inductive and capacitive filter, respectively [116]. The spacing of $\lambda/4$ between the elements increases and decreases the upper passband frequency of inductive filter and the lower passband frequency of capacitive filter, respectively as shown in Figure 1.14(c). A differential phase shift of 90° is obtained in the common passband ($f_{L1} - f_{C2}$) due to the same slope of phase shift through either of the filter as shown in Figure 1.14(d)-(f) generating a CP wave.

The Jerusalem cross [117], [118] LTC polarization converter as shown in Figure 1.15(b) is a single substrate layer polarization converter where 90° phase difference between the orthogonal components of the transmitted wave is achieved by tuning inductive coupling among arms and capacitance between the unit cells. Furthermore, this structure has a high transmission loss and is not reconfigurable. A single layer polarization converter using a metallic annular ring and strip is reported in [119].

A linear-to-circular polarization converter reported in [120] achieves wideband performance using an array of sub-wavelength capacitive patches and inductive grids as shown in Figure 1.15(c) The structure performs differently along the x- and y-directions due to the asymmetry in the unit cell. Although the structure provides a wideband response, the design is multilayered. A two-substrate-layer polarization converter using different geometrical sizes and shapes in the unit cell based on the cross composite as shown in Figure 1.15(d) is reported in [121]. This structure converts an LP wave to a CP wave with a wide 3-dB ARBW of 74% using a cascade of different layers with different sizes and shapes in the unit cell.

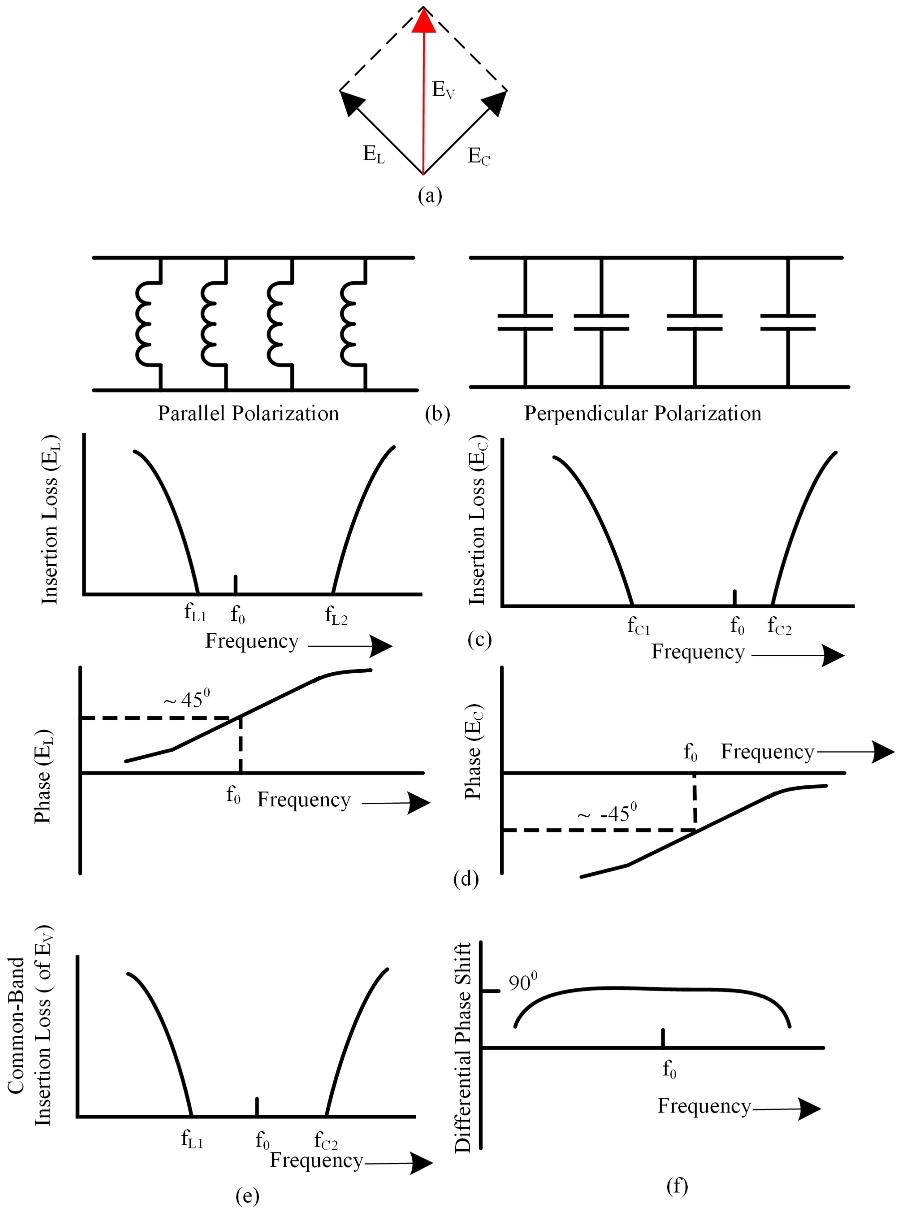

Figure 1.14: Summary of principle of operation of meander line polarizer.

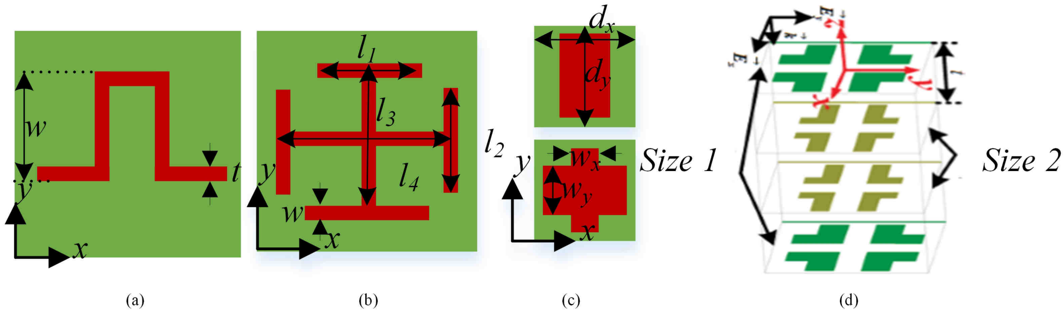

Figure 1.15: Some transmission type linear-to-circular polarization converter (a) Meander line [112], (b) Jerusalem cross [117], (c) sub-wavelength capacitive patches and inductive grids [120] and (d) cross composite [121]

.

Dual-band linear-to-circular polarization converter designed on single and two substrate layers are reported in [122] and [123], respectively. LTC polarization converter presented in [123] possess split-ring structures as shown in Figure 1.16(a). The electrically and magnetically excited rings have different size which generate equal magnitude orthogonal transmitted components with a 90° phase difference. The converter reported in [124] uses a pair of a planar dipole with the dipole printed on the top, and the bottom layers respond to transverse electric and magnetic waves, respectively. In [125], dual-band LTC polarization conversion is obtained by using a cascaded structure of split-ring resonators and patches divided by a metallic strip as shown in Figure 1.16(b). The structure is four-substrate layered and behaves differently for orthogonal polarizations due to the uneven nature of the converter design. The dual-band LTC polarization converter reported in [126] and [127] uses a three-metal layer unit cell in its design and is based on the antenna filter antenna element [128]. It operates at 20/30 GHz with low insertion loss and narrow bandwidth.

A five-layer modified Jerusalem cross reported in [129] possesses a 0.6 dB insertion loss and 4% and 2.7% ARBW in the frequency band $19.2-20$ GHz and $29.2-30$ GHz, respectively. Multilayer structure reported in [130] is based on FSS utilizing a resonator at top and a metallic line on the bottom surface of the substrate. A metasurface based dual-band LTC polarization converter using a subwavelength T-type resonator and rectangular split-ring resonator in its unit cell is reported in [131]. The polarization conversion is achieved by manipulating the mutual interactions among two types of resonators. A single substrate layer LTC polarization converter consisting of a rectangular loop and a

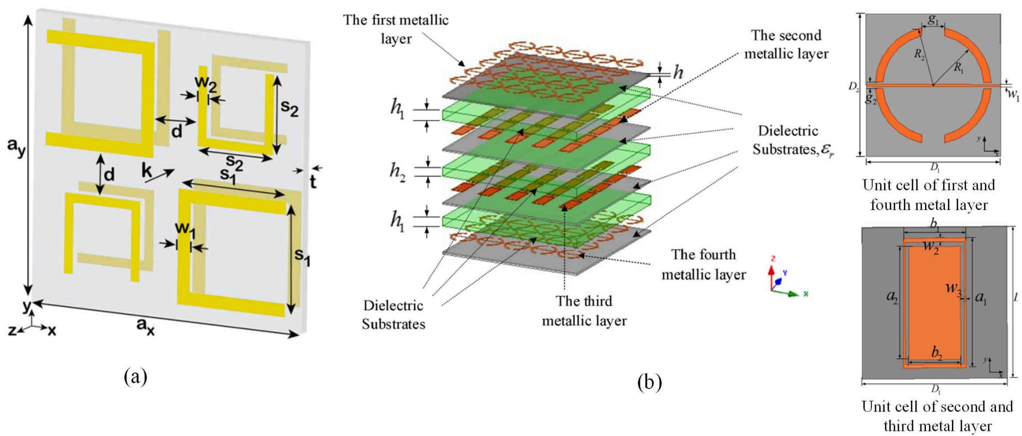

Figure 1.16: Some dual-band LTC polarization converters (a) split-ring [123] and (b) split-ring and metallic stip [125].

diagonal strip is reported in [132]. The polarization converter is used atop of patch and slot antenna to change the polarization and improve the impedance bandwidth. The 3 dB ARBW achieved with this polarization converter is about 12% at the center frequency of 2.45 GHz. Due to the inductive and capacitive effects of the rectangular loop and diagonal strip, the components of the incident LP wave could be phase advanced and delayed to produce a 90° phase difference between the equal amplitude orthogonal components of transmitted wave. A single-layer transmission type LTC polarization converter composed of an asymmetric cross slot [133] is studied. The polarization converter is used to modify the polarization state and reduce the radar cross-section (RCS) of a slot. The polarization converter provides a 3 dB ARBW of 10% at 4 GHz. The lengths of the two slots govern the reactance of the polarization converter for the incident LP wave and produce signals of equal magnitude with a phase difference of 90° thereby generating a CP wave. In [134] a three-layer polarizer consisting of two aperture coupled patches based on a second-order bandpass FSS, is reported. An ARBW of 30% (5.10 – 6.97 GHz) is exhibited by this converter. The unit cell consists of two aperture coupled patches. A CP wave is realized after transmission through the polarization converter when the polarizer is excited by a vertical or horizontal LP wave. Multilayer LTC polarization converter using split-ring bisected by a metallic strip based is studied in [135]. The advantage of this design is low cross- polarization and low sensibility to the incidence angle. Furthermore, angular stability up to 25° of oblique incidence over the frequency range of 25.5 – 36.5 GHz is achieved.

1.8 Motivation

Electromagnetic waves extensively used in wireless communication and satellites in outer orbit are an integral part of connecting areas around the globe. In satellite communication, certain frequency bands are used and typically one prefers to send enough information as possible within these bands [136]. One way to achieve this is to use the use orthogonally polarized EM waves. Linear polarization is suitable in point to point communication. The polarization of the LP wave can be changed from one state to the orthogonal state by rotating the transmitting antenna by 90°. The shortcoming of using LP EM waves is that to maximize the signal reception, the receiving antenna needs to be aligned in the same polarization as the transmitting antenna [136]. Therefore, it is difficult to manage an alignment when dealing with satellites and hence, linear polarization is not ideal. Faraday rotation is another undesirable phenomenon that LP waves undergo when passing through the ionosphere [136]. Alternatively CP wave is the ideal candidate for use in satellite communication as it allows flexibility in the orientation of transmitting and receiving antennas [137]. The only condition is that the receiver/transmitter antenna should be designed for one of the orthogonal circular polarizations.

Circularly polarized antennas have numerous advantages over that of the linearly polarized antennas, like the mitigation of multi-path interferences or fading [138],[139], immune to Faraday rotation due to the magnetic field in the ionosphere arising from the plasma [140] and polarization mismatching between transmitting and receiving antennas [141]. With these immense advantages, CP antennas are largely employed in wireless communication systems for satellite communications, global navigation satellite system (GNSS), radio frequency identification (RFID), mobile communications, wireless local area networks (WLAN), and direct broadcasting services (DBS) [142].

Antenna arrays are needed for high gain performance in modern wireless communication systems. Presently, CP arrays are becoming progressively vital to high-data-rate communication links, high-resolution radar and tracking systems, software radios, multi-functional systems, and electronic warfare applications [143] − [145]. The conventional arrays usually constitute a large number of elements where it is difficult to generate a CP radiation at each antenna element and often involve complex feeding networks like substrate integrated waveguide (SIW) feeding [146], [147], SIW with sequential rotation [148], substrate integrated gap waveguide (SIGW) feeding [149], dielectric based inverted microstrip gap waveguide [150] and feed involving grounding vias [151].

The CP waves can be obtained either directly from a CP antenna or a LTC polarization converter can be used with a LP radiating element to get a CP wave. The second scheme is more convenient and desirable in planar arrays where generation of CP wave at each antenna element is challenging. Therefore, FSS based LTC polarization converters can be used with LP antenna arrays to get CP radiation out of them. The complexity in the feeding network of arrays can be simplified through reflectarrays (RAs). However, RAs suffer from narrow bandwidth and signal blockage [152]. Considering these problems, a relatively simpler design to obtain a CP antenna array is needed which is achieved using

LTC polarization converter in this thesis.

With the advent of FSS based approaches, many efforts have been made to manipulate and control polarization by using LTC polarization converters to transform an incident linearly polarized (LP) wave into a reflected/transmitted CP wave. However, most of the LTC polarization converters reported are multilayered, bulky, and prone to fabrication error due to misalignment between each layer. Single substrate layer LTC polarization converter is therefore an effective solution to resolve the errors caused due to multilayer problem. Although, single substrate layer designs overcome the problem associated with multilayer configurations, the independent control of LP and CP states are still challenging. Therefore, an attractive application of LTC polarization converter in LP antennas is their expandability to reconfigurability [153]. The uniqueness is to design polarization reconfigurable converters and antennas where both linear and circular modes of operation are achievable within a single structure. Thus there remain ample scope for the design of reconfigurable polarization converters.

The angular stability of a LTC polarization converter determines its ability to provide satisfactory performance for oblique incidence of the incident wave. However, most of the LTC polarization converters achieve polarization conversion for smaller oblique incidence [49], [113], citeb120, [121], [135], [161], [165] and [166]. Therefore, higher angular stable single substrate layer LTC polarization converters are desirable. Furthermore, the LTC polarization converter with wide angular stability must possess compact size. Therefore, there has been significant interest towards the design of stable and compact size LTC polarization converters.

In satellite communications to enhance the isolation between the transmitted and received signals, an antenna must function in two nonadjacent frequency bands with orthogonal polarization. This way a single channel can be used for transmitting and receiving an EM waves with orthogonal polarization, thereby doubling the channel capacity. Therefore, dual-band LTC polarization converters with orthogonal polarization at the two operating frequency band can be explored which can be used in combination with dual-band LP antennas to realize a dual-band orthogonally polarized CP antenna. The few dual-band LTC polarization converters reported in literature [4], [120] $-$ [125], [129], [130] and [170] are multilayered and possess large size. Therefore, single substrate layer dual-band LTC polarization converter with compact size further need to be explored. The polarization diversity in wireless communication systems can be implemented with the use of polarization reconfigurable CP antennas [154] and thereby realizing frequency reuse and advancement in satellite communication systems [155].

Multiple-Input-Multiple-Output (MIMO) systems provide a significant increase in channel capacity without the need of additional bandwidth or transmit power by deploying multiple antennas for transmission to achieve diversity gain. A CP dual-band MIMO antenna with orthogonal circular polarization in the uplink and downlink frequency bands of satellite communication is desirable to increase the channel capacity twofold. Furthermore, the polarization in the two frequency bands should be interchangeable. However, dual-band CP MIMO antennas reported [183], [184], [188], and [191] possess same sense of polarization at the two operating frequency bands. Therefore, a dual-band CP MIMO antenna with orthogonal circular polarization and polarization diversity can be explored.

In summary, there are necessities for LTC polarization conversion structures with following desirable features:

1. Single substrate layer design.
2. Compact unit cell size.
3. Angularly stable for both TE and TM incident wave.
4. Compact dual-band converter with orthogonal circular polarization at the two frequency bands of operation.
5. Reconfigurable converters.

1.9 Organization of Thesis

The thesis is organized into six chapters with **Chapter-1** as an introduction where a brief overview of polarization and frequency selective surfaces have been discussed. The state-of-the-art on the designs of polarization converters (linear-to-linear/circular) operating in reflection and transmission mode has been studied. The motivation behind the work carried out in this thesis along with its organization are provided at the end of this chapter.

In **chapter-2** the detailed design, characterization and fabrication of a polarization reconfigurable converter (PRC) exhibiting linear-to-linear and linear-to-circular polarization conversion based on frequency selective surface is discussed. The unit-cell of the polarization converter is hexagon shaped whose polarization state can be controlled using a PIN diode embedded in its central arm. Polarization reconfigurable behavior of the converter is verified by placing 45° clockwise rotated 6 × 6 array of the proposed PRC's unit cell on top of an LP patch antenna. The transmitted radiation from the antenna with the PRC in the ON and OFF state of the PIN diode is LP and CP (left or right), respectively.

In **chapter-3**, a wide angularly stable LTC polarization converter is designed and fabricated. The polarization converter works in the transmission mode and is realized by printing periodic cells consisting of split-ring and a horizontal metallic strip on both sides of 60 mil thick substrate layer (ε_r= 2.2, $tan\delta$ = 0.0009). In the frequency band: 28.75 – 32.85 GHz, the converter can convert an LP incident wave to a CP wave with very low insertion loss (< 0.65 dB) and axial ratio bandwidth of 13.32%. The polarization converter shows angular stability up to 60° and 45° for TE and TM polarization, respectively while, the ellipticity greater than 0.95 in the frequency band: 28.75 – 31.55 GHz under oblique angle incidence is achieved. The proposed polarization converter can be used for uplink Ka-band fixed-satellite service (29.5 – 30.0 GHz) and military satellite communication (30.0 – 31.0 GHz) applications. The proposed LTC polarization converter is integrated with a 1 × 4 and 4 × 4 LP patch antenna array to obtain CP antenna arrays working at around 30 GHz. Thus, a simple design to obtain and realize CP antenna arrays is discussed.

In **chapter-4**, a compact dual-band LTC polarization converter is designed and fabricated on a single layer substrate material. The converter consists of split-rings and horizontal and vertical metallic strips printed on both sides of the dielectric substrate for dual-band operation. The converter transmits a right-hand circularly polarized (RHCP) wave at the lower band and a left-hand circularly polarized (LHCP) wave at the upper band for a linearly polarized (LP) incident wave. The characteristics of the polarization converter are validated by integrating an array of 7 × 7 elements of its unit cell in the end-fire direction of a dual-band LP dipole antenna operating in the same frequency bands such as that of the polarization converter. The antenna integrated with the polarization converter exhibits measured circularly polarized (CP) bandwidths of 7.80% and 6.57% in the lower frequency band: 20.10 – 21.75 GHz and the upper- frequency band: 29.4 – 31.4 GHz, respectively. The integrated antenna can act as a feed source of a high-gain dual-band transmit array for uplink (30.0 – 31.0 GHz) and downlink (20.2 – 21.2 GHz) of the Ka-band military satellite communication.

In **chapter-5**, a dual-band CP four-port multiple-input multiple-output (MIMO) antenna for K/Ka-bands fixed-satellite service is designed and fabricated using a dual-band transmission type LTC polarization converter discussed in chapter-4. The single element of MIMO is composed of a cascade of two dipoles of different lengths resonating at around 20 and 30 GHz. An array of 7 $\times$ 7 elements of the unit cell of dual-band LTC polarization converter is placed at a distance of $\lambda_o/4$ (λ_o is calculated with respect to the center frequency of lower band) in the end-fire direction of MIMO antenna to obtain an orthogonally CP wave at two frequency bands. The orthogonal circular polarization at lower and upper- frequency bands can be reversed by exciting the orthogonal ports. The proposed CP antenna shows good MIMO performance with correlation coefficient (CC) less than 0.19 and diversity gain (DG) better than 0.97 at both the frequency bands. A prototype of the MIMO antenna is fabricated and the measured CP bandwidths of 11.51% and 3.69% are obtained in the lower (19.65 – 22.05 GHz) and upper (29.25 – 30.35 GHz) frequency bands, respectively. The proposed antenna can be used for Ka-band: 29.5 – 30.0 and 19.7 – 20.2 GHz frequency bands assigned for fixed satellite service as uplink and downlink frequencies, respectively.

Finally, the conclusion and future scope of the works done in this thesis are presented in **Chapter-6**.

Chapter 2

Reconfigurable Linear-to-Circular Polarization Converter

Polarization converter or polarizer has earned a significant consideration among the scientists and researchers in the field of satellite communication because of their vast applications. Linear to circular polarization converters play a significant part in satellite wireless communication, for example it is used to shift the satellite antennas's polarization from linear to circular or viceversa to realize a CP antenna using a LTC polarization converter. CP antenna allows stable data transmission irrespective of orientation of transmitter and receiver [153]. Furthermore, the polarization property of the converter/antenna should be controllable and the overall size of the antenna be compact [49]. Hence there has been a great interest towards the design of compact CP patch antennas.

In this chapter, a LTC polarization reconfigurable converter (PRC) working in transmission mode is discussed. The PRC's fundamental unit consists of a cascade of half-hexagon structure and its mirror replica printed on both sides of a single layer substrate. A PIN diode inserted in the central arm of the unit cell controls the PRC's behavior to a $\phi = 45°$ LP incident wave, transmitting an LP and CP in the ON and OFF state of the diode, respectively. The proposed PRC is compact with an overall size of $0.046\lambda_o^3$ (λ_o is calculated with respect to 15.15 GHz) and exhibits a polarization conversion ratio greater than 0.9 in the frequency band 14.0 – 16.0 GHz. The polarization reconfigurable behavior of the converter is verified by placing 45° clockwise rotated 6 × 6 array of the proposed PRC's unit cell on top of an LP patch antenna. The transmitted radiation from the antenna with the PRC in ON and OFF state of the PIN diode is LP and CP (left or right). A prototype of the antenna with PRC is fabricated, and the results obtained from measurements are in agreement with simulated ones.

2.1 Design and Operation of Unit Cell of PRC

2.1.1 Principle of operation

When a LP wave is incident on the surface of the converter along +z direction, the transmitted wave consists of both x- and y-polarized components. Transmission matrix T is used to relate the amplitude of the incident field to those of the transmitted field as represented in Equations (1),(2), and (3)[157]

$$\begin{pmatrix} E_x^t \\ E_y^t \end{pmatrix} = T \begin{pmatrix} E_x^i \\ E_y^i \end{pmatrix} = \begin{pmatrix} t_{xx} & t_{xy} \\ t_{yy} & t_{tx} \end{pmatrix} \begin{pmatrix} E_x^t \\ E_y^t \end{pmatrix} \tag{2.1}$$

where the first and second subscripts i and j correspond to the polarized components of the transmitted and incident fields, respectively. Generally, a transmitted wave is represented as a superposition of two LP orthogonal components with identical magnitude.

$$\overrightarrow{E^t} = \overrightarrow{E_x^t} + \overrightarrow{E_y^t} = E_0^t(T_x\hat{x} + T_y\hat{y})e^{-jkz} \tag{2.2}$$

where E_0^t is the amplitude and

$$\begin{bmatrix} T_x \\ T_y \end{bmatrix} = \begin{bmatrix} |T_x|e^{j\phi} \\ |T_y|e^{j\phi} \end{bmatrix} \tag{2.3}$$

is the linear transmission matrix. As a result, a phase change of $\triangle\phi = \phi_x - \phi_y$ appears at the output of the converter among two orthogonal components. Therefore, if $|T_x| = |T_y|$ and $\triangle\phi = \pm 90^0$, the polarizer converts a LP incident wave into a CP one.

2.1.2 Unit cell design

The unit cell of the proposed PRC consists of two metallic printed half-hexagon shaped structures as shown in Figure 2.1. The front-view, back-view, and perspective-view of the proposed unit cell are respectively shown in Figure 2.1(a-c). To improve the transmission

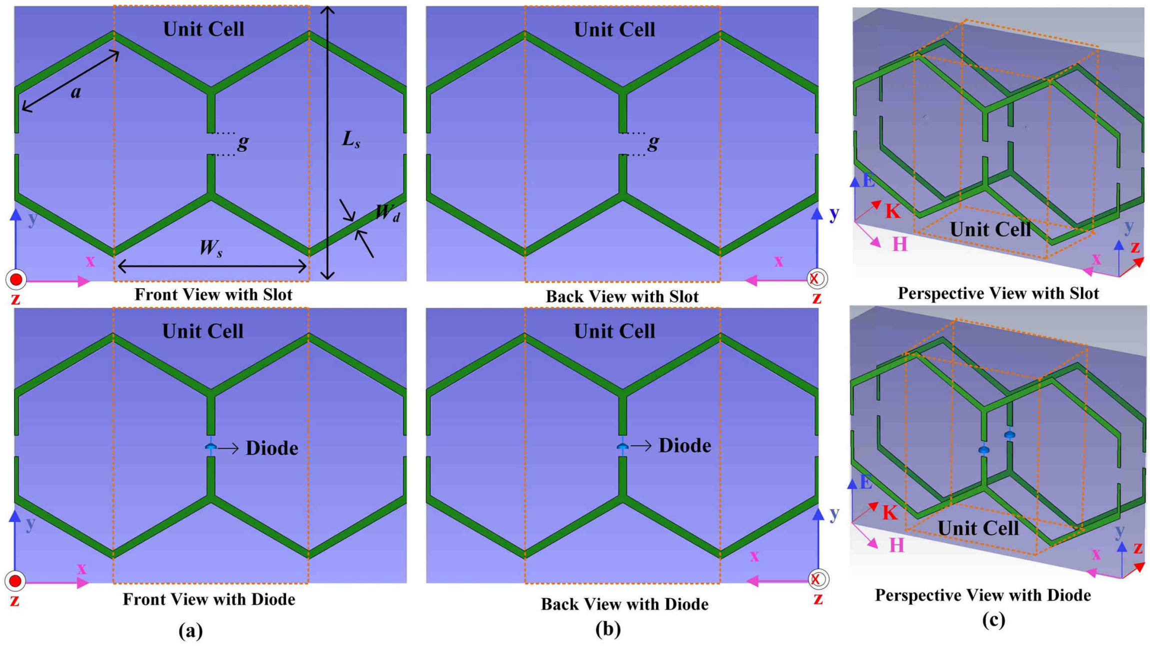

Figure 2.1: Proposed unit cell of the polarization reconfigurable converter (a) front view, (b) back view and (c) perspective view. $W_s = 9.25$, $L_s = 13$, $a = 5.34$, $g = 1$, and $W_d = 0.34$ (all dimensions in mm).

through the converter, the basic unit cell is printed on both the sides of the substrate material with the dielectric constant of 2.2 and a loss tangent of 0.0009. The slot length "g" in the middle of the cell plays an important role in the functioning of the cell. For the cell to act as LP to CP converter, the orthogonal components of the transmission coefficients should be nearly equal in magnitude with a 90° phase difference between them.

2.1.3 Response of polarization reconfigurable converter for a $\phi = 45°$ polarized incident wave

The behavior of the cell is determined through simulations using CST Microwave Studio electromagnetic solver. An infinite array of this design is simulated under the unit cell boundary conditions along x- and y-directions with open along the z-direction. The cell is excited by an incident wave polarized along $\phi = 45°$ as shown in Figure 2.1(c). The cell is simulated with slot length g equal to 0 and 1 mm representing short and open cases, respectively. The simulation results are obtained and it is confirmed that under the conditions g = 0 mm and g = 1 mm, the cell transmits an LP and CP wave respectively. Utilizing this concept, the slot length is modeled as a PIN diode for the two cases with g = 1 mm representing the OFF state of the diode and g = 0 the ON state to make the polarization converter reconfigurable. The PIN diode (BAR63-02LE6327) from the Infineon Technologies [155] with length 1 mm, ON-state resistance of 1Ω, and OFF state capacitance of 0.3 pF is used to control the reconfigurability of PRC. In the ON state of the diode, the PRC transmits two orthogonal components with equal magnitude and phase difference varying between 13° – 19° in the frequency range 13.76 – 17.0 GHz as shown in Figure 2.2(a) representing an LP wave. However, for the OFF state of the diode, two orthogonal components have equal amplitude with a phase difference of 85° – 110° in the frequency band 14.84 – 15.84 GHz as shown in Figure 2.2(b) representing a CP wave. To further validate the linear and circular polarization behaviour of the polarization converter, the AR of the polarization converter is calculated for two states from transmission coefficients using (2.4)[153]. The results obtained are shown in Figure 2.2(c). AR of the polarization converter for the cases when the diode is ON and OFF is obtained as 15 dB and 0.4 dB representing an LP and CP wave transmitted from the converter, respectively. Therefore, the operation of the unit cell can be switched between linear to circular polarization. The polarization conversion ratio (PCR) which measures the polarization conversion of an incident wave to the transmitted cross and co-component is shown in Figure 2.2(d). The PCR of the proposed PRC is greater than 0.9 (90%) in the frequency band 14.0 – 16.0 GHz which denotes a good polarization purity and maximum PCR reaches around 0.98 (98%) at 15.45 GHz.

$$AR = 10log_{10}\frac{(T_{xx}cos\tau+T_{yy}cos\triangle\phi sin\tau)^2+ \ T_{yy}^2sin^2\triangle\phi sin^2\tau}{(T_{xx}sin\tau+T_{yy}cos\triangle\phi cos\tau)^2-T_{yy}^2sin^2\triangle\phi cos^2\tau} \tag{2.4}$$

Where, $\tau = 1/2arctan((2T_{xx}T_{yy}cos\triangle\phi)/(T_{xx}^2 - T_{yy}^2))$, T_{xx} and T_{yy} are transmission coefficients in x- and y-polarization, $\triangle\phi$ is the phase difference between T_{xx} and T_{yy}.

Furthermore, to verify the results, as shown in Figure 2.2(a) and (b), the surface current distribution along the unit cell of the proposed PRC is observed. Figure 2.2(e) and (g) shows the current distribution for y- and x-polarization, respectively, when there is no slot (Diode ON) in the central arm of the unit cell. The current is mostly concentrated along this central arm. The equivalent current length along the y-direction is increased, which results in the decrease of the resonant frequency of the unit cell for y-polarization, as shown in Figure 2.2(a). As shown in Figure 2.2(f) and (h), there is an open circuit in the central arm of the unit cell, and the current does not find the continuous path through this arm. The current is equally distributed in the upper and lower half of the unit cell and traverses equal length for both the polarization along x- and y-axes. Therefore, the unit cell resonates around the same frequency in this state for both the polarization, as shown

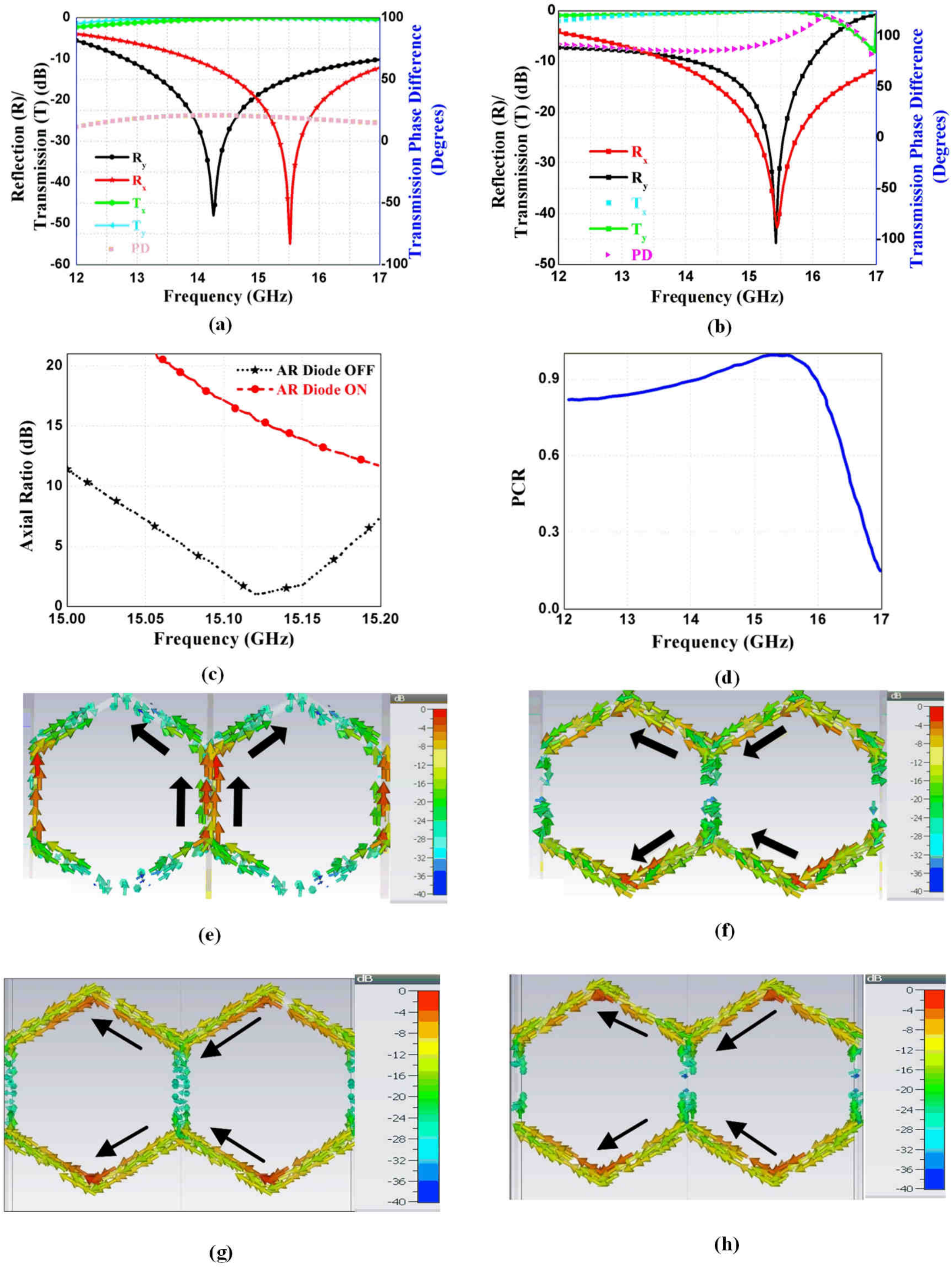

Figure 2.2: Plot of reflection/transmission coefficient and transmission phase difference of polarization reconfigurable converter (PRC) for (a) g = 0 (Diode ON) (b) g = 1 (Diode OFF), R_x, R_y is reflection and T_x, T_y is transmission for x- and y-polarized incident wave respectively, PD is phase difference between T_x and T_y. (c) Axial ratio (AR) for g = 0 (Diode ON) and g = 1 (Diode OFF). (d) Polarization conversion efficiency (PCR). Surface current (e) g = 0 (Diode ON), (f) g = 1 (Diode OFF) for y-polarization, (g) g = 0 (Diode ON) and (h) g = 1 (Diode OFF) for x-polarization.

in Figure 2.2(b). The performance comparison of the proposed polarization converter in terms of reconfigurability, the number of substrate layers used in the converter and electrical size is shown in Table 2.1. The proposed polarization converter is reconfigurable, uses a single substrate layer, and is compact as compared to polarization converters studied in Ref. [49], [117], [119] − [121] and [159] − [161].

Table 2.1: Performance Comparison of the Proposed Single-Band Linear-to-Circular Polarization Converter with the other Converters available in Literature

Reference	Frequency (GHz)	Number of Substrate Layers	Thickness	Reconfigurable	Dimension of Unit Cell mm^3
[49]	10	4	$0.2\lambda_o$	Yes	$0.33\lambda_o \times 0.33\lambda_o$
[117]	17.8	1	$0.09\lambda_o$	No	$0.33\lambda_o \times 0.33\lambda_o$
[119]	13.9	1	$0.0235\lambda_o$	No	$0.44\lambda_o \times 0.44\lambda_o$
[120]	10	4	$0.18\lambda_o$	No	$0.15\lambda_o \times 0.15\lambda_o$
[121]	9	4	$0.24\lambda_o$	No	$0.45\lambda_o \times 0.45\lambda_o$
[159]	10.7	1	$0.1248\lambda_o$	No	$0.428\lambda_o \times 0.428\lambda_o$
[160]	12.95	1	$0.069\lambda_o$	No	$0.432\lambda_o \times 0.432\lambda_o$
[161]	30	2	$0.275\lambda_o$	No	$0.39\lambda_o \times 0.39\lambda_o$
This Work	15.1	1	$0.15\lambda_o$	Yes	$0.465\lambda_o \times 0.654\lambda_o$

2.2 Study Under Oblique Incidence

In general, the incident wave to the polarization converter may be oblique depending upon the source or antenna. Hence, the response of the converter under oblique incidence angle is studied. The angular stability of the proposed reconfigurable polarization converter is studied for TE and TM polarizations against different incident angles θ. For TE and TM polarization the reflection responses of the proposed PRC for different incident angles is shown in Figure 2.3(a) and 2.3(b), respectively. The transmission responses against different incident angles for TE and TM polarization is shown in Figure 2.3(c) and 2.3(d), respectively. It is observed that the reflection response remains stable in the operating band upto the incident angle of 25° and corresponding transmission response remains

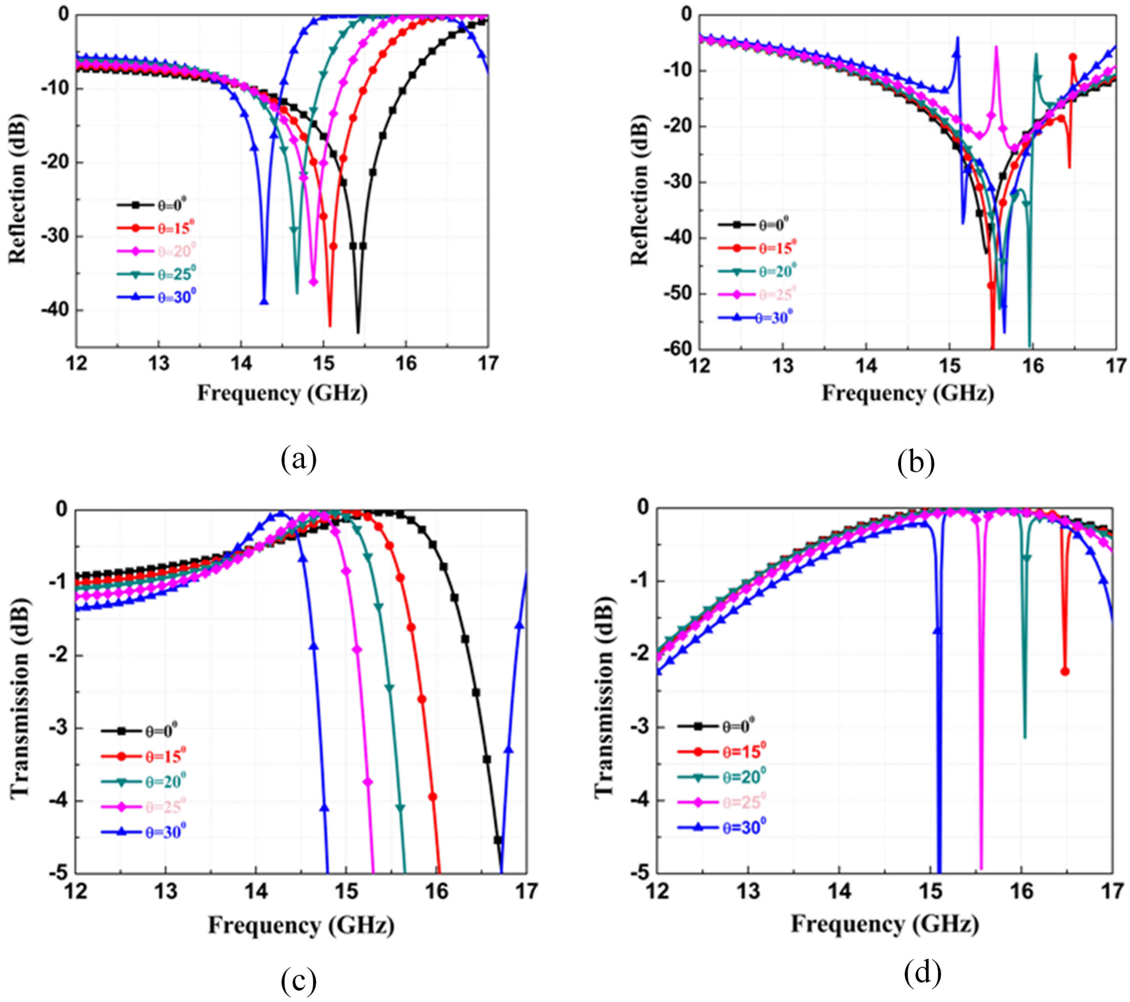

Figure 2.3: Oblique incidence performance (a) reflection TE, (b) reflection TM, (c) transmission TE and (d) transmission TM.

better than -1 dB in the working band of the converter. Hence, it can be concluded that the proposed converter shows an angular stability of upto 25° of incidence angle.

2.3 Equivalent Circuit of Unit Cell of PRC

The equivalent circuit of the unit cell of the polarization converter in ON and OFF state is shown in Figure 2.4(a) and (b), respectively. The LC model of the front and back side of the unit cell of the polarization converter are identical due to the same structure on the front/back side. The coupling between two metal layers on top and bottom of the substrate material is modeled by the parallel LC circuit, while the series LC circuit is due to resonance of the hexagonal loop structures in the top and bottom layers. The capacitance C_3 in the OFF case arises due to the slot in the central arm of the unit cell of the converter. The dielectric is modeled by a lossy transmission line of length equal to substrate thickness and having characteristic impedance given by (2.5), where Z_o is the characteristic impedance of free space and ε_r is the permittivity of the dielectric substrate.

$$Z = Z_o/\sqrt{\varepsilon_r} \tag{2.5}$$

The equivalent circuits are simulated using Keysight ADS software. The circuit response representing the simulated S_{11} of the equivalent circuits for x- and y-polarized waves in the ON state is shown in Figure 2.4(c) and (d), respectively whereas the OFF state response is depicted in Figure 2.4(e) and (f).

2.4 Integration of Polarization Converter With Patch Antenna

In this section, the integration of an LP patch antenna with PRC proposed in section 2.1.2 is discussed to validate the functionality of the PRC. An LP patch antenna is designed resonating at around 15.15 GHz [1] using the same substrate as that of the PRC with a thickness of 0.762 mm. A 6×6 array of the unit cell of proposed PRC, 45° clockwise rotated, is used as a superstate on top of the LP antenna. The height of the polarization converter from the patch antenna is optimized through simulations, and it is found the minimum AR for the CP state of PRC is obtained at the height of $\lambda_o/3$ (λ_o is wavelength with respect to 15.15 GHz), as shown in Figure 2.5(b). The PRC as a superstate and patch antenna is shown in Figure 2.5(a). The overall dimension of the PRC is $40 \times 40 \times 3$ mm^3 ($2.01 \times 2.01 \times 0.153\lambda_o^3$), while the PRC with antenna exhibits a total size of $40 \times 40 \times 10.3$ mm^3 ($2.01 \times 2.01 \times 0.518\lambda_o^3$).

2.5 Simulation and Experimental Results of PRC Integrated With LP Patch Antenna

An LP microstrip patch antenna is fabricated through the standard photolithographic procedure. A 6×6 array of the proposed PRC is also fabricated and is used as a superstate at a height of $\lambda_o/3$ from the patch antenna. The fabricated prototype of the LP patch antenna with PRC is shown in Figure 2.5(c). The reflection coefficient (S_{11}) measurement of the fabricated antenna with PRC is done using the MS2028C Vector Network Analyzer from Anritsu. The antenna can be operated in both the ON and OFF configurations of

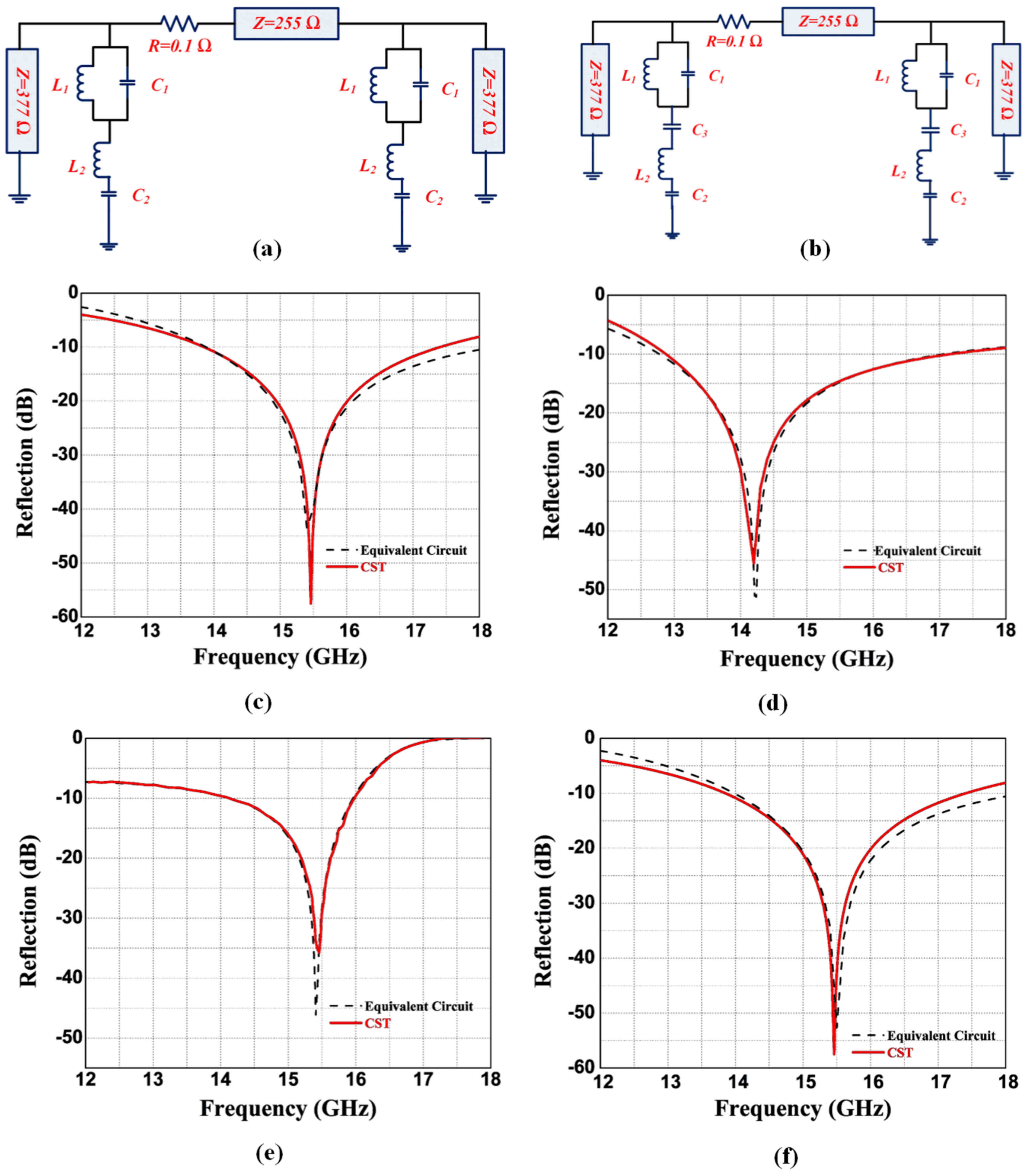

Figure 2.4: Equivalent circuit of polarization reconfigurable converter (PRC) (A) ON case ($L_1 = 10nH$, $C_1 = 10pF$, $L_2 = 5.77nH$, $C_2 = 66.53fF$ [x-polarization]), ($L_1 = 10nH$, $C_1 = 10pF$, $L_2 = 9.47nH$, $C_2 = 30.6fF$ [y-polarization]) (b) OFF case ($L_1 = 10nH$, $C_1 = 10pF$, $L_2 = 5.77nH$, $C_2 = 66.53fF$, $C_3 = 1.45pF$ [x-polarization]), ($L_1 = 10nH$, $C_1 = 10pF$, $L_2 = 9.47nH$, $C_2 = 30.6fF$, $C_3 = 0.06pF$ [y-polarization]). Circuit simulation of equivalent circuit (c) ON case x-polarization, (d) ON case y-polarization, (e) OFF case x-polarization, and (f) OFF case y-polarization.

.

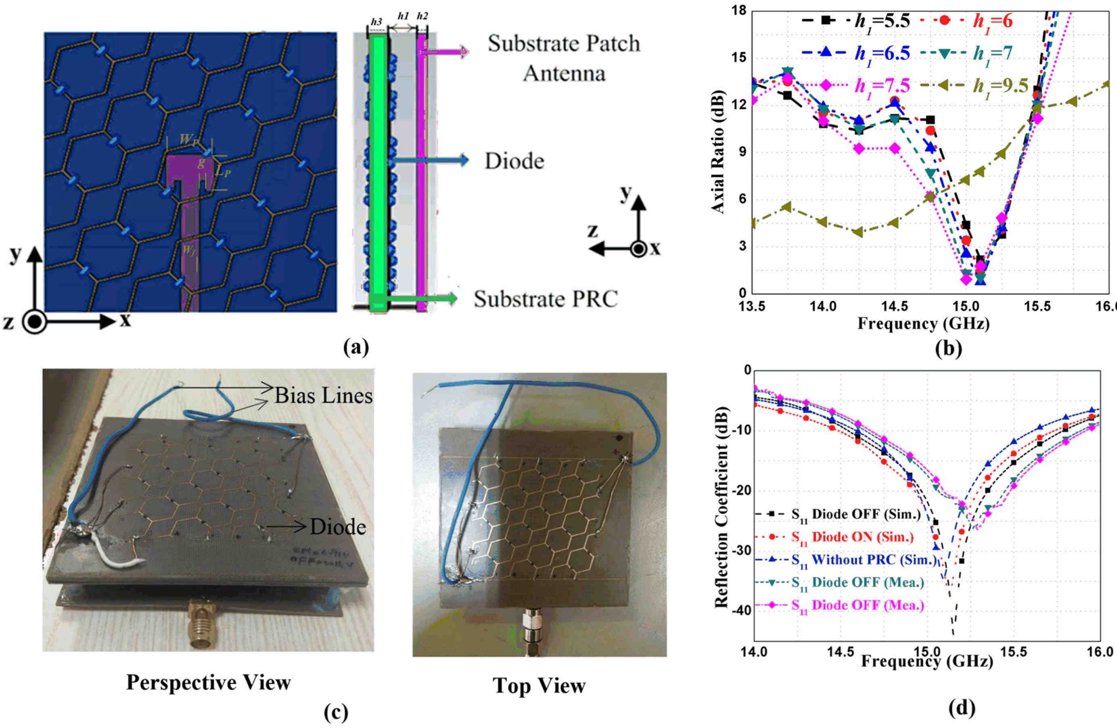

Figure 2.5: (a)Schematic of antenna with polarization reconfigurable converter (PRC). (b) Axial ratio for different heights (h_1) between antenna and polarization converter. (c) Fabricated patch antenna with PRC. (d) Simulated and measured reflection coefficient of patch antenna with PRC. $h_1 = 6.5$, $h_2 = 0.762$, $h_3 = 3.04$, $w_p = 8.25$, $L_p = 6.4$, $g = 1$, and $w_f = 2.85$ (all dimensions in mm).

the PIN diode. The magnitude of simulated and measured S_{11} parameters of the antenna with and without PRC is shown in Figure 2.5(d) and agree well. It can be observed that with the presence of a polarization converter, there is no effect on the reflection coefficient of the antenna. With this configuration of the PRC, the element lines of the PRC itself are used as biasing lines for the PIN diodes. Therefore, no separate biasing network for PIN diodes is required eliminating the complexity in designing.

All the AR measurements were carried out experimentally in an anechoic chamber using N9010A EXA (X-Series) Signal Analyzer from Keysight Technologies. The simulated and measured AR for different states of the PIN diode and hence PRC with antenna are depicted in Figure 2.6(a), which show a good concurrence. The PIN diode is turned ON by providing a bias voltage of 0.91 V, in this state the PRC transmits an LP wave as explained in section II, and also the AR of the antenna is above 15 dB both in simulations and measurements as shown in Figure 2.6(a) representing the linear polarization of the antenna. However, if the PIN diode is turned OFF by giving a 0 V bias voltage, the PRC transmits a CP wave, as shown in Figure 2.2(b). In the OFF state of the diodes, the

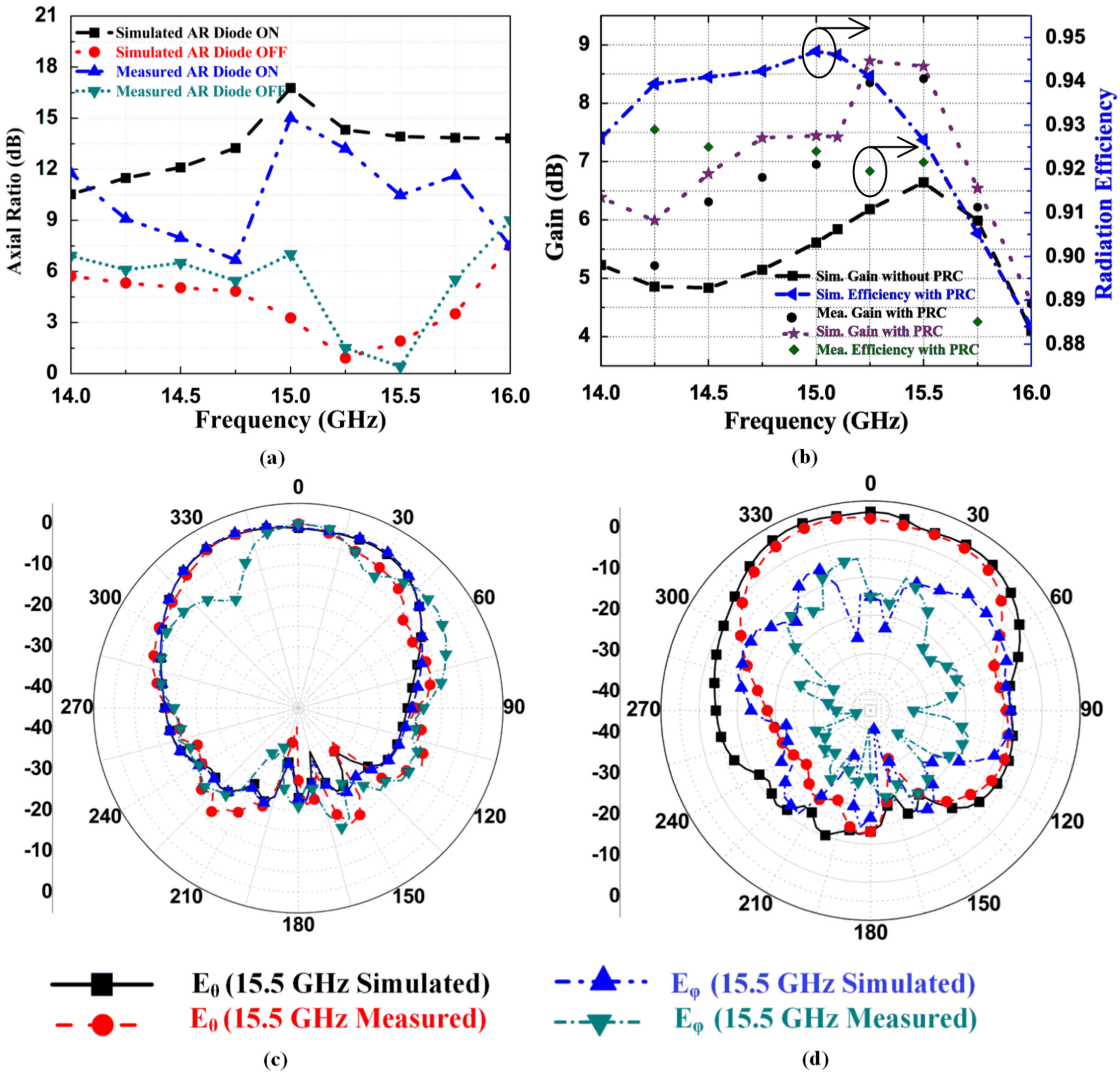

Figure 2.6: (a)Axial ratio of patch antenna with polarization reconfigurable converter (PRC). (b) Gain and radiation efficiency of the antenna with polarization converter. Radiation pattern in xz-plane for (c) g = 1 mm (Diode OFF) and (D) g = 0 mm (Diode ON).

minimum AR measured is around 0.86 dB, as shown in Figure 2.6(a), representing the circular polarization of the antenna. Therefore, the polarization of the antenna can be controlled by the working state of the diodes. To ensure that the PRC is illuminated with a 45° polarized incident wave, the PRC elements are rotated 45° clockwise to the patch antenna. The clockwise rotation of the PRC provides a right-hand CP wave in the OFF state of the diodes. A left-hand circular polarization of the antenna can be acquired if elements are rotated 45° anticlockwise. The gain and radiation efficiency of the antenna with PRC is shown in Figure 2.6(b). The simulated and measured gain of the antenna without PRC is around 6.53 dBi and around 8.53 dBi with PRC. The increase in gain can be attributed due to the formation of the Fabry-Perot cavity in the antenna with the PRC. The radiation pattern of the antenna with PRC is measured in xz-plane and is shown in Figure 2.6(c,d) for the OFF and ON states of the diodes, respectively. A good agreement between simulated and measured results is obtained.

2.6 Conclusion

A thin reconfigurable polarization converter based on FSS transmitting an LP and CP wave in its two states is presented. The two states of the PRC are controlled by the operating state of the PIN diode fitted in the central arm of the hexagonal unit cell. The PRC is single substrate layered, compact with an electrical size of $0.046\lambda_o^3$, PCR of higher than 0.9, and reconfigurable. A 6×6 array of PRC unit cells is successfully demonstrated on an LP patch antenna working in the Ku band (14.10 – 15.97 GHz) to change the polarization state of the patch antenna. The polarization state of the LP patch antenna is changed from linear to circular in the OFF state of diodes of PRC. The linear polarization of the LP patch antenna remains unaffected in the ON state of diodes. The proposed linear to circular polarization converter can be used with an antenna/antenna array to feed a highly directive transmit array designed in the uplink (14.0 – 14.5 GHz) of the Ku band satellite communication band for very small aperture terminal (VSAT) from 14 – 14.5 GHz.

Chapter 3

Wide Angularly and Ellipticity Stable Linear-to-Circular Polarization Converter

In this chapter, a transmission type LTC polarization converter is designed using split-rings and a horizontal metallic strip printed on both sides of a single substrate layer (ϵ_r = 2.2, tan δ = 0.0009). The polarization converter can convert an incident LP wave to a CP wave with very low insertion loss (< 1.25 dB) in the frequency band: 28.75 – 32.85 GHz. Moreover, for oblique incidence up to 60^0 and 45^0 for TE and TM polarization, respectively ARBW and ellipticity (e) responses remain quite stable. A prototype of 71 × 71 unit-cells of the proposed LTC polarization converter is fabricated and measurement results are in good agreement with simulated ones. The measured ARBW or e in the range of 0.94 – 0.98 is obtained in the frequency band of 29.50 – 32.65 GHz (10.13%). Furthermore, the characteristics of the polarization converter are verified by placing a 45° rotated array of 15 × 15 elements of its unit-cell in the broadside direction of a 1 × 4 and 4 × 4 LP patch antenna array operating in the same frequency band such as that of the polarization converter to transform them into a CP patch antenna array. The integrated 1 × 4 and 4 × 4 antenna array show a measured gain of 14.1 dBic and 18.7 dBic, respectively. The proposed polarization converter and CP antenna arrays can be used for uplink Ka-band fixed-satellite service (29.5 – 30.0 GHz) and military satellite communication (30.0 – 31.0 GHz) applications.

3.1 Design and Principle of operation of the Proposed Linear- to-Circular Polarization Converter

A transmission matrix (T) correlates the incident (E^i) and transmitted (E^t) fields of the converter [154], as expressed in (3.1).

$$\begin{bmatrix} E_x^t \\ E_y^t \end{bmatrix} = T \begin{bmatrix} E_x^i \\ E_y^i \end{bmatrix} = \begin{bmatrix} t_{xx} & t_{xy} \\ t_{yx} & t_{yy} \end{bmatrix} \begin{bmatrix} E_x^i \\ E_y^i \end{bmatrix} \tag{3.1}$$

where, $t_{ij} = E_i^t/E_j^i$, i and j denote the polarized components of the transmitted and incident fields, respectively. In general the transmitted wave can be represented as (3.2) [157], where E_0^t is the amplitude and (3.3) is the linear transmission matrix. Hence,

$$\overrightarrow{E^t} = \overrightarrow{E_x^t} + \overrightarrow{E_y^t} = E_0^t(T_x\hat{x} + T_y\hat{y})e^{-jkz} \tag{3.2}$$

$$\begin{bmatrix} T_x \\ T_y \end{bmatrix} = \begin{bmatrix} |T_x|e^{j\phi} \\ |T_y|e^{j\phi} \end{bmatrix} \tag{3.3}$$

from (3.3), it is evident that the phase difference of $\triangle\phi_{xy} = \phi_x - \phi_y$ between the two orthogonal components emerges at the output of the converter. The CP wave is obtained from the polarizer, if $|T_x| = |T_y|$ and $\triangle\phi = \pm 90^0$.

3.1.1 Design and Analysis of unit cell

The property of polarization conversion is realized through the cross-coupling of electric and magnetic resonances occurring due to incident waves. The unit-cell of the proposed LTC polarization converter consists of two identical layers of metallic pattern separated by a single dielectric substrate layer. The metallic pattern consists of a metallic strip embedded in two concentric split-rings as shown in Figure 3.1(a). Diclad 880 ($\epsilon_r = 2.2$, tan $\delta = 0.0009$) with a thickness of 1.52 mm is chosen as substrate material. The performance of the converter can be shaped by appropriately adjusting the geometrical parameters of unit-cell. When a LP wave is incident on the surface of the LTC polarization converter, the transmitted wave from it will consist of both the x- and y-polarized components.

The response of the transmitted components is shown in Figure 3.2(a). It can be seen

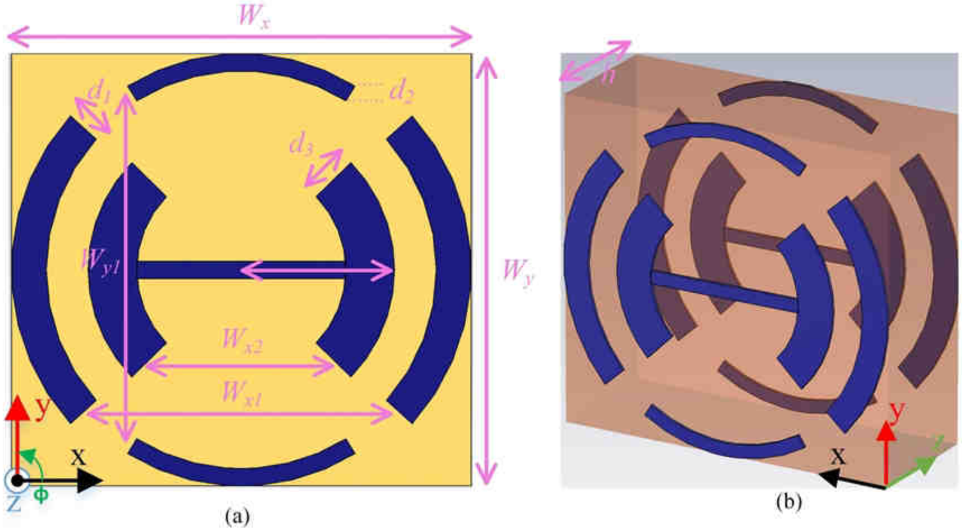

Figure 3.1: (a) Front and (b) perspective views of the proposed linear-to-circular polarization converter. $W_x = 3.96$, $W_{x1} = 2.23$, $W_{x2} = 1.35$, $W_y = 3.76$, $W_{y1} = 3.02$, $d_1 = 0.15$, $d_2 = 0.3$ and $d_3 = 0.42$ (all in mm).

that the x- and y-polarized reflected components in the frequency range 28.56 – 31.23 GHz is below -10 dB and the corresponding transmission coefficients are better than -0.65 dB. The phase difference ($\Delta\phi_{xy} = \phi_x - \phi_y$) between the two orthogonal transmitted components is plotted in Figure 3.2(b) and it is seen that $\Delta\phi_{xy} = -90°$ is obtained in this frequency band. Based on the results presented in Figure 3.2(a) and Figure 3.2(b), it can be implied that a LHCP wave is transmitted from the polarization converter when excited by an LP wave. The polarization conversion ratio (PCR) measures the polarization conversion of an incident wave to the transmitted co- and cross-polarized components. The PCR of the proposed polarization converter is plotted in Figure 3.2(b) using (3.4) [12].

$$PCR = \frac{|t_{yy}|^2}{|t_{yy}|^2 + |t_{xy}|^2} \tag{3.4}$$

where, T_{yy} and T_{xy} are the co-polar and cross-polar transmission, respectively, for a y-polarized incident wave. The PCR of the proposed LTC polarization converter is shown in Figure 3.2(b). It is observed that the PCR greater than 0.85 (85%) is obtained in the frequency band 28.0 − 31.0 GHz, which denotes an excellent polarization purity, and maximum PCR reaches around 0.992 (99.2%) at 29.23 GHz.

The AR is used to reveal the degree of the CP, which is mathematically calculated from (3.5) taking the magnitude of transmission coefficients and phase difference between

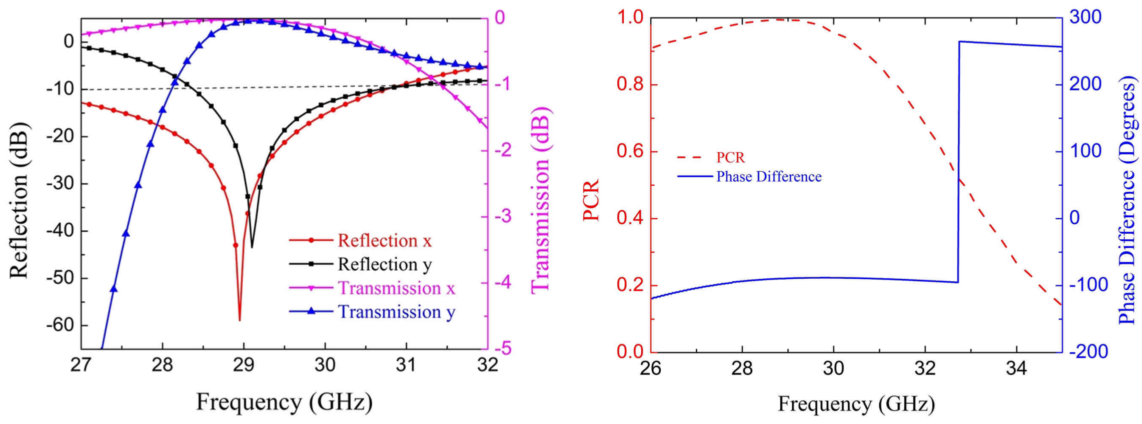

(a) (b)

Figure 3.2: Simulated (a) magnitude of reflection and transmission coefficients and (b) PCR and phase difference between the transmission coefficients of the proposed linear-to-circular polarization converter.

them into account.

$$A.R. = \sqrt{\frac{|t_{xx}|^2 + |t_{yy}|^2 + \sqrt{a}}{|t_{xx}|^2 + |t_{yy}|^2 - \sqrt{a}}}, \tag{3.5}$$

where, $a = |t_{xx}|^4 + |t_{yy}|^4 + 2|t_{xx}|^2|t_{yy}|^2 \cos(2\Delta\varphi_{xy})$. To get further a understanding of the LTC polarization conversion, Stokes parameters of (3.6) [12] are used.

$$\begin{aligned} I &= |t_{xx}|^2 + |t_{yy}|^2 \\ Q &= |t_{xx}|^2 - |t_{yy}|^2 \\ U &= 2\,|t_{xx}|\,|t_{yy}|\cos\phi_{xy} \\ V &= 2\,|t_{xx}|\,|t_{yy}|\sin\phi_{xy} \end{aligned} \tag{3.6}$$

Based on the Stokes parameters, ellipticity (e) defined as the ratio of V/I is calculated. For the left and right hand circularly polarized wave, the value of e is $+1$ and -1, respectively. As shown in Figure 3.3, the ellipticity of the proposed LTC polarization converter is close to $+1$ in the frequency band 28.75 – 31.55 GHz. Hence, the LHCP wave is transmitted by the proposed polarization converter.

3.1.2 Study Under Oblique Incidence

In practice, the incident wave may always not be normal to the plane of the polarization converter. It can be oblique or deflected due to the type of radiation antenna or other sources. Therefore, the performance of the polarization converter under oblique incidence must be studied. The proposed LTC is analyzed first for ellipticity variation with respect

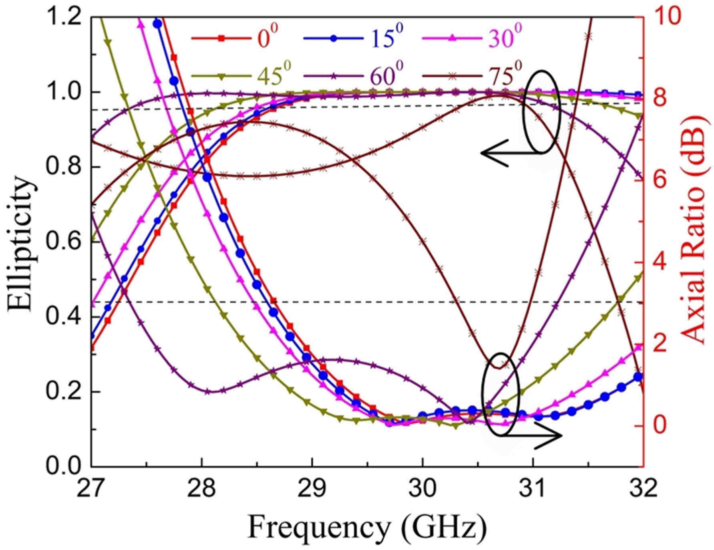

Figure 3.3: Ellipticity and axial ratio of the proposed linear-to-circular polarization converter under oblique incidence for TE polarization.

to different incident angles. Figure 3.3 shows the simulated ellipticity and AR for the different incident angles from 0° to 75°. The ellipticity and AR response remains quite stable for incident angle up to 60°. The proposed polarization converter is also evaluated under different incident angles for both transverse electric (TE) and transverse magnetic (TM) incident waves for linear to circular transmission coefficients. The variation of LHCP and RHCP transmission coefficients for oblique incidence under TE and TM polarization is presented in Figure 3.4(a) and (b), respectively. The co-and cross polarized transmission coefficients better than -1.25 dB and -15 dB is retained up to an oblique incidence angle

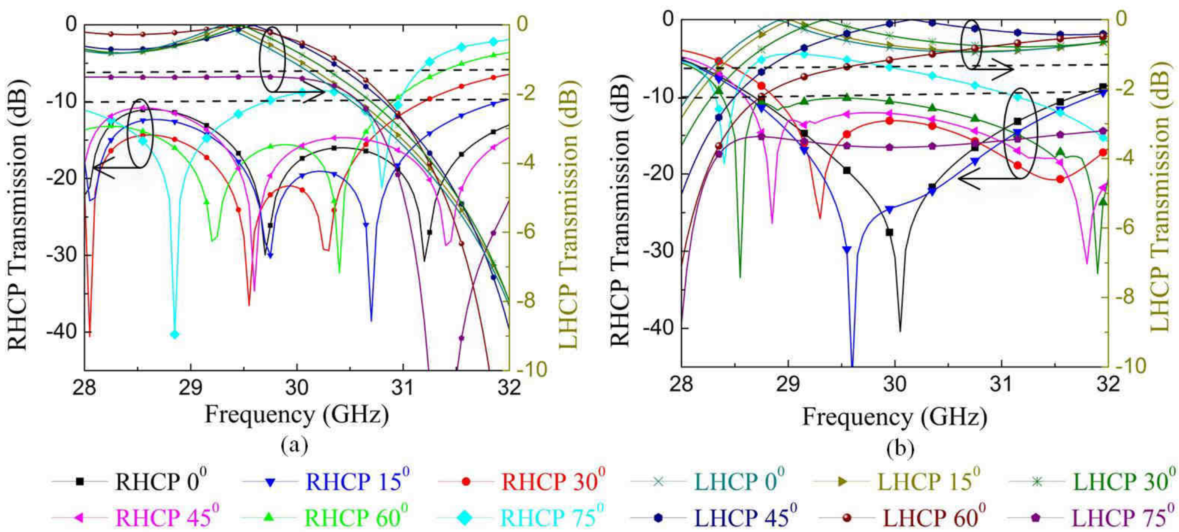

Figure 3.4: Magnitude of LHCP and RHCP transmission coefficients under oblique incidence for (a) TE and (b) TM polarization for the proposed converter.

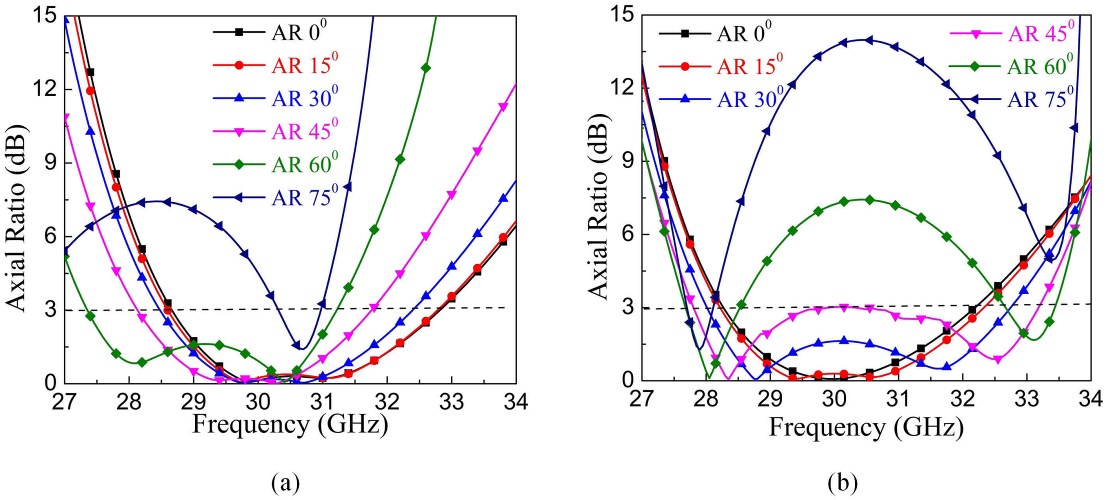

Figure 3.5: Magnitude of axial ratio under oblique incidence for (a) TE and (b) TM polarization for the proposed converter.

of 60° and 45° for TE and TM polarization, respectively. Furthermore, the AR under oblique incidence remains below 3dB for incident angle upto 60° and 45°, respectively for TE and TM polarization. This variation of AR with incident angle variation is shown in Figure 3.5(a) and (b) for TE and TM polarization, respectively. Accordingly, the overall angular stability upto 45° of the incident angle can be maintained for the proposed linear-to-circular polarization converter.

3.2 Equivalent Circuit of the Proposed Linear-to-Circular Polarization Converter

The LTC polarization converter used in this work consists of center connected metallic-strip and therefore it possess weak coupling between orthogonal components [162] of E-fields. Thus, the cross-polarization transmission coefficients of the proposed LTC polarization converter are negligible. The two metallic layers on the top and bottom of the dielectric substrate provide sufficient isolation due to the fact that ratio of element length to thickness of dielectric substrate lies within the range of $1.3 - 3.0$ according to [163]. Due to the properties of the polarization converter stated, the equivalent circuit model (ECM) can be separated for x- and y-polarizations. The ECM for x- and y-directions of the proposed polarization converter is shown in Figure 3.6(a) and (b), respectively. In the equivalent circuit, L_{x1}, C_{x1} and L_{y1}, C_{y1} are the inductances and capacitances of outer split-ring along x- and y-directions, respectively. C_{x2} is the capacitance between

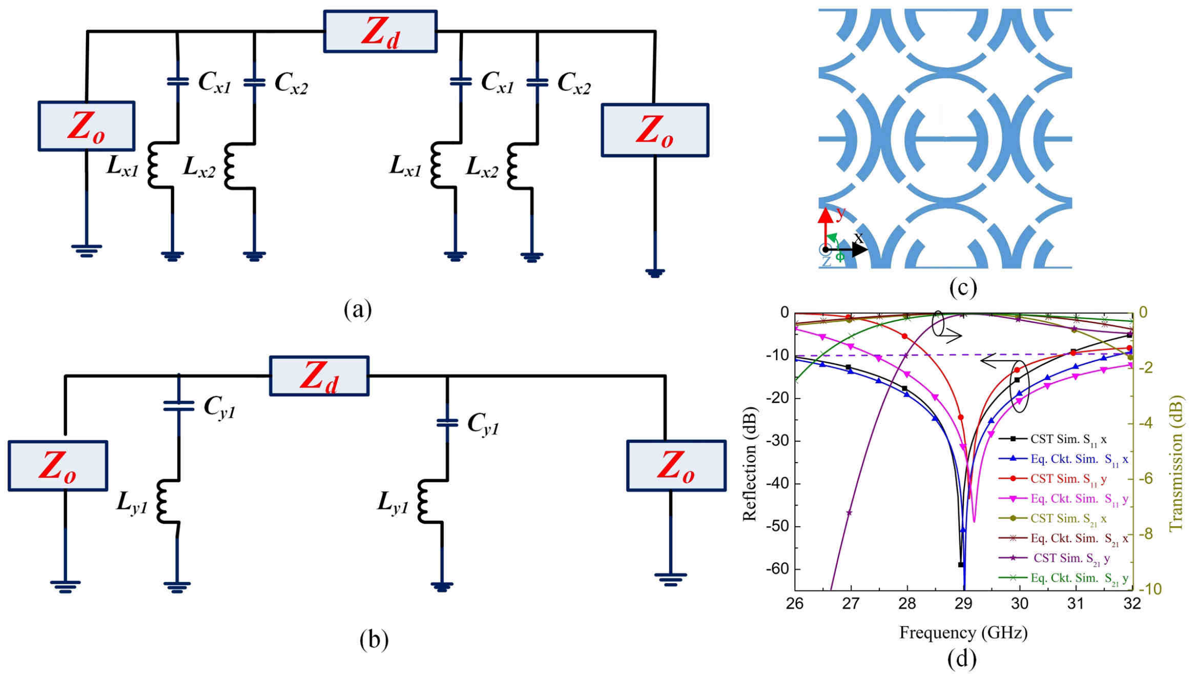

Figure 3.6: Equivalent circuit model for (a) x-polarization ($C_{x1} = 3.958$ fF, $C_{x2} = 1.04$ fF, $L_{x1} = 8.8$ nH, $L_{x2} = 9.86$ nH), (b) y-polarization ($C_{y1} = 3.94$ fF, $L_{y1} = 6.1$ nH) and (c) ECM model and (d) response of equivalent circuit and electromagnetic solver for x- and y-polarized incident waves of the proposed LTC.

inner and outer split-ring along x-direction while L_{x2} represent the inductance of inner metallic strip along x-direction. The dielectric between the top and bottom metal layer is modelled by a transmission line with characteristic impedance Z_d given by (3.7), where Z_0 is free space impedance and ε_r is relative dielectric permittivity. The equivalent circuit of the LTC polarization converter is simulated in Keysight Advanced Design System (ADS). The initial dimensions of the circuit elements have been approximated using (3.8) and (3.9) [164], where μ_0 and ε_0 represent the permeability and permittivity, respectively of the vacuum, W_x is unit cell length, d_1 is thickness of metallic split-ring along y-axis and $\varepsilon_{eff} = \sqrt{\varepsilon_r + 1)/2}$ is the equivalent permittivity of the substrate.

$$Z_d = \frac{Z_0}{\sqrt{\varepsilon_r}} \tag{3.7}$$

$$L = \frac{\mu_0 W_x}{2\pi} \ln\left(\left(\sin\frac{\pi d_1}{2W_x}\right)^{-1}\right) \tag{3.8}$$

$$C = \frac{2\varepsilon_0 \varepsilon_{eff} W_x}{\pi} \ln\left(\left(\sin\frac{\pi d_1}{2W_x}\right)^{-1}\right) \tag{3.9}$$

The final values of different circuit components are presented in caption of Figure 3.6. The ECM response of the LTC polarization converter for the x- and y-polarization of incident wave is shown in Figure 3.6(d) and a good concurrence with the results obtained from CST electromagnetic solver is obtained, hence validating the equivalent circuit. The impedance of the top and bottom metallic layers derived for the x- and y-direction is represented in (3.10) and (3.11), respectively.

$$Z_x = \frac{(1-\omega^2 L_{x1} C_{x1})(1-\omega^2 L_{x2} C_{x2})}{j\omega(C_{x2} + 2C_{x1} - 2\omega^2 L_{x2} C_{x1} C_{x2} - \omega^2 L_{x1} C_{x1} C_{x2})} \tag{3.10}$$

$$Z_y = \frac{(1-\omega^2 L_{y1} C_{y1})}{2j\omega C_{y1}}. \tag{3.11}$$

3.3 Experimental Verification of Proposed Linear-to-Circular Polarization Converter

A prototype of the proposed LTC polarization converter consisting of 71 × 71 cells with a total surface area of 28.1 cm × 26.6 cm is fabricated using the standard photo-lithographic technique. The photograph of the fabricated prototype is shown in Figure 3.7(a) and Figure 3.7(b) shows the measurement set up to carry out the measurement. The measurement of the reflection and transmission characteristics of the polarization converter is carried out with Keysight PNA N52245B using free-space measurement method. The polarization converter with a standard gain, Ka-band (26.50 – 40 GHz) LP horn antenna acts as the transmitter, while another standard gain Ka-band LP horn antenna serves as the receiver, and the prototype is kept in the far-field region of the antennas. The reflection and transmission coefficients for x- and y-polarized waves are measured and agree well with their simulated counterparts as shown in Figure 3.8. It can be seen in Figure 3.8 that in the frequency range of 28.64 – 31.35 GHz, the magnitude of the transmission coefficients remain better than -1.25 dB and the corresponding reflection coefficients are below -10 dB. The AR and ellipticity are calculated from the measured transmission data using (3.5) and (3.6), respectively and plotted as shown in Figure 3.9. The measured 3-dB AR bandwidth of 9.67% (29.50 – 32.50 GHz) is achieved. The ellipticity is also measured and is shown in Figure 3.9. In the frequency band of 29.50 – 32.0 GHz, the measured ellipticity greater than 0.94 is obtained. Thus an LHCP wave is transmitted within this frequency band. The comparison of some of the important parameters of the unit cell of the proposed LTC polarization converter with the corresponding parameters of the other polarization converters available in the literature is presented in Table 3.1. The proposed LTC polarization converter is single substrate layered, compact in size, possesses high angular stability and ellipticity as compared to the converters reported in [49], [113], [120], [121], [135], [161], [165] and [166].

Table 3.1: Performance comparison of the proposed linear-to-circular polarization converter with the other single band polarization converters available in the literature.

Reference	Frequency (GHz)	Number of Substrate Layers	Size (λ_o^3)	Angular Stability	Ellipticity
[49]	10	4	0.021	—	—
[113]	25	1	0.0024	30°	—
[120]	10	4	0.004	45°	—
[121]	9	4	0.0486	20°	—
[135]	21	4	0.046	25°	—
[161]	30	1	0.0418	20°	—
[165]	30	Multilayer	0.0624	30°	—
[166]	15.1	1	0.0456	25°	—
Proposed	30	1	0.022	60° (TE), 45° (TM)	> 0.94

λ_o is the w.r.t center frequency of the operating band of the converter.

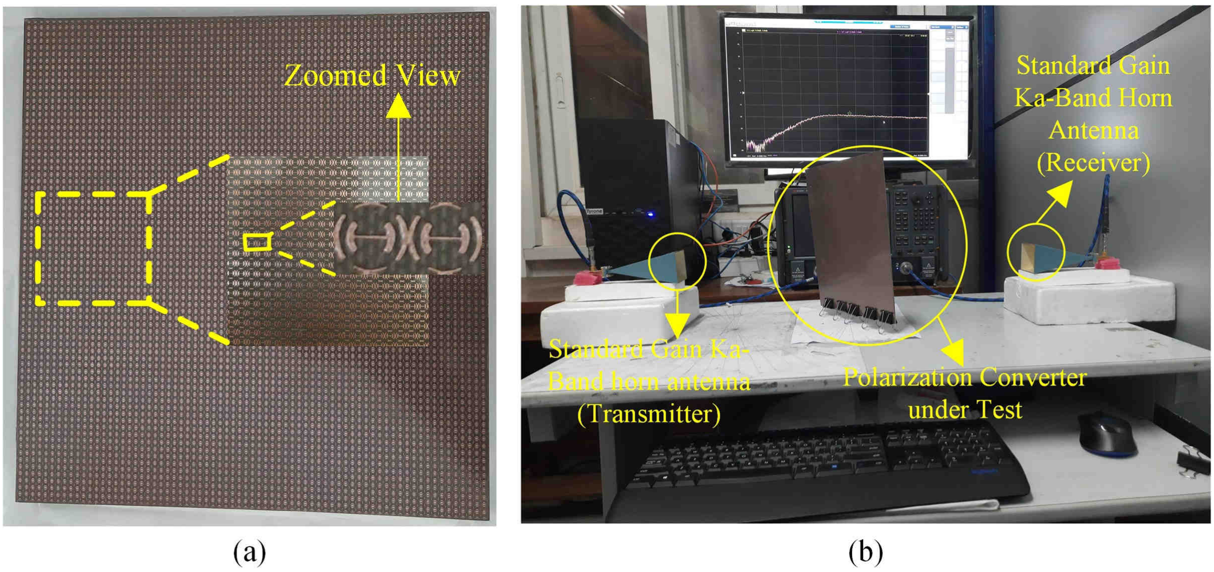

Figure 3.7: (a) Fabricated prototype and (b) measurement setup of the proposed linear-to-circular polarization converter.

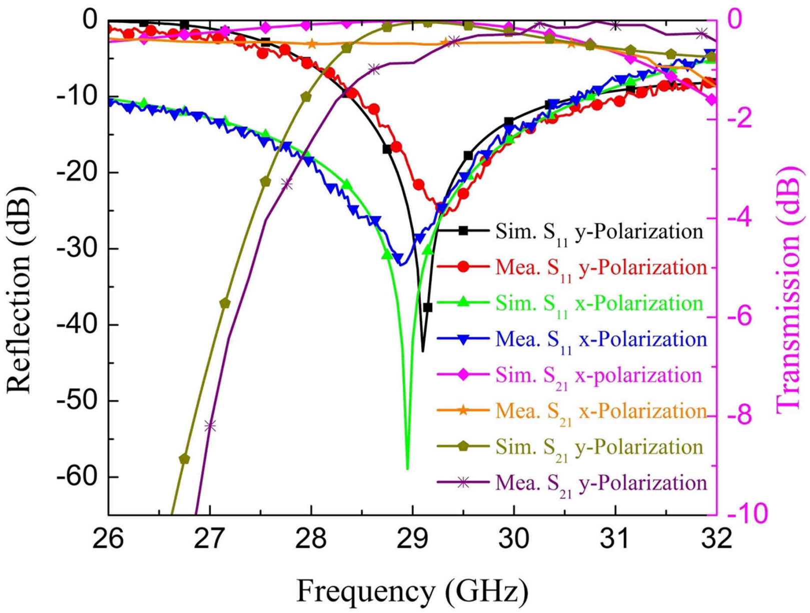

Figure 3.8: Magnitude of simulated and measured reflection and transmission coefficients of the proposed linear-to-circular polarization converter.

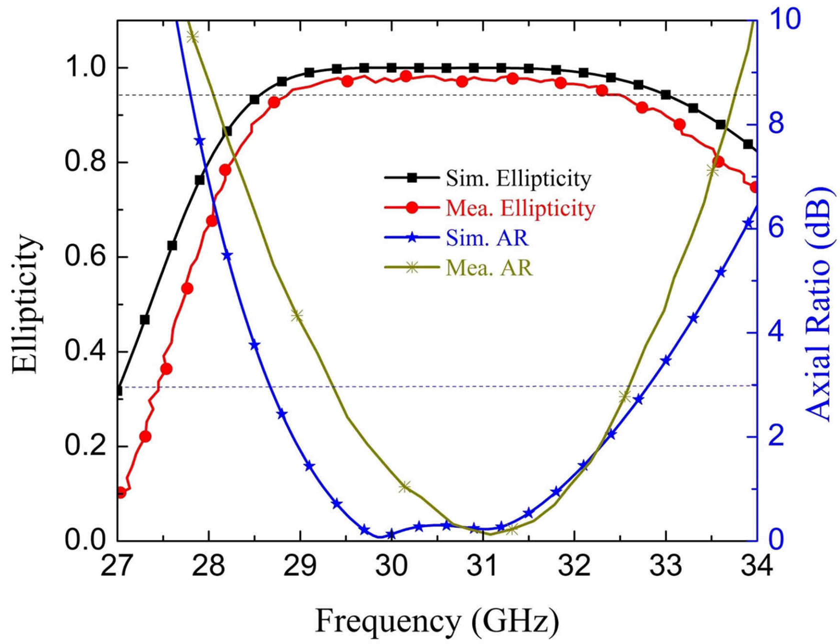

Figure 3.9: Magnitude of simulated and measured ellipticity and axial ratio of the proposed linear-to-circular polarization converter.

3.4 Integration of the Proposed Polarization Converter with 1 × 4 and 4 × 4 Patch Antenna Array

In this section the proposed LTC polarization converter discussed in section 3.1.1 is integrated with 1 × 4 and 4 × 4 LP antenna arrays to realize the CP antenna arrays. Firstly, the proposed LTC polarization converter is integrated with a single patch antenna de-

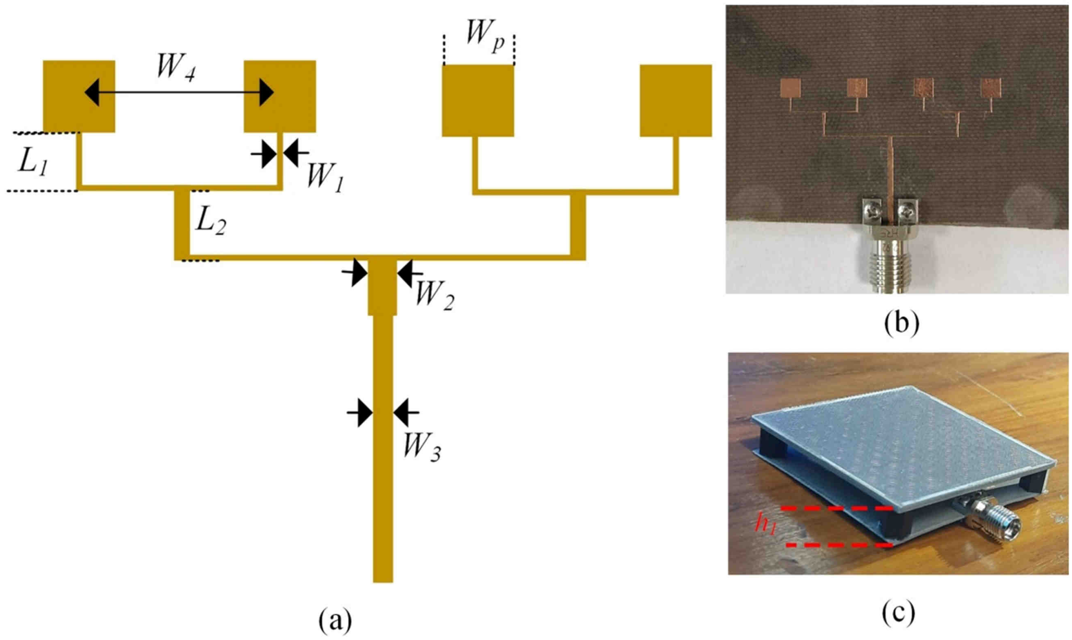

Figure 3.10: (a) Schematic and (b) fabricated prototype of the 1 × 4 LP patch antenna array. (c) Fabricated prototype of 1 × 4 patch antenna array with polarizer. $W_p = 2.9$, $L_1 = 2$, $W_1 = 0.20$, $L_2 = 1.6$, $W_2 = 0.45$, $W_3 = 0.76$ and $h_1 = 5.75$ (all in mm).

signed around the same operating frequency as that of the polarization converter and fabricated. The results of the integrated single patch antenna with polarization converter are not discussed and shown here for brevity.

3.4.1 1 × 4 CP Antenna Array

The proposed LTC polarization converter is integrated with a 1 × 4 and 4 × 4 LP patch antenna array as an application to design and realize CP antenna arrays. A 1 × 4 and 4 × 4 LP patch antenna array is designed [1], resonating at around the same frequency as that of the proposed LTC polarization converter using the Diclad 880 substrate with a thickness of 0.508 mm. The schematic of the 1 × 4 is shown in Figure 3.10. A 15 × 15 array of the converter's unit cell, 45° clockwise rotated, is used atop the LP patch antenna array at a height of $\lambda_o/2$ (λ_o is wavelength with respect to operating frequency of the array antenna). It is found that the minimum AR is obtained at a height of around $\lambda_o/2$ after performing the parametric studies. The overall dimension of the 1 × 4 patch antenna array with the converter is 34 × 34 × 7.62 mm^3 (3.4 × 3.4 × 0.76 λ_o^3). A prototype of the 1 × 4 LP patch antenna array (Figure 3.10(b)) with the polarization converter is fabricated (Figure 3.10(c)) and measured. The simulated and measured results of

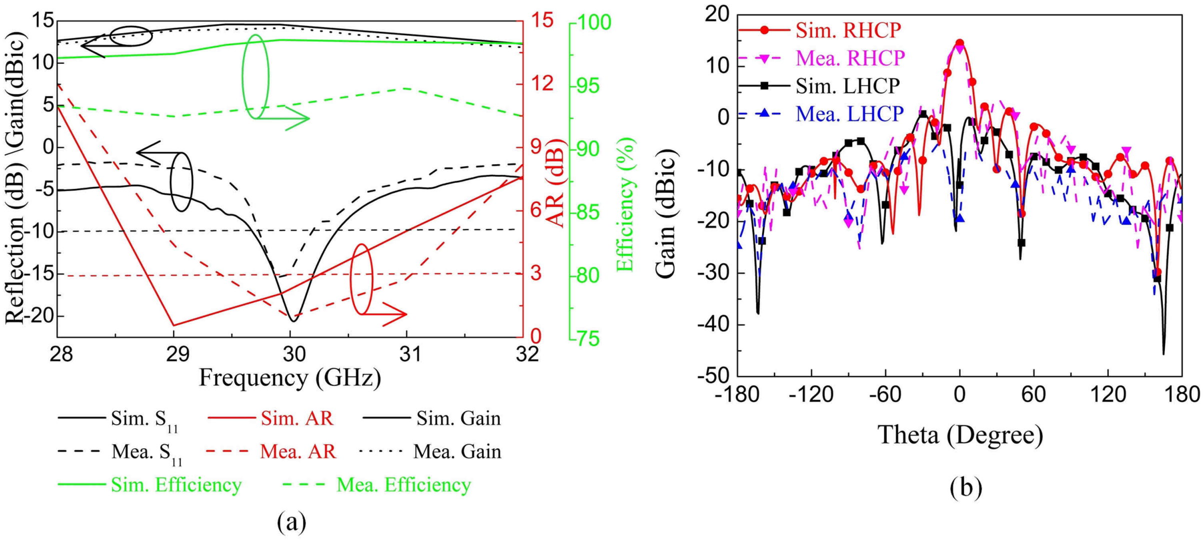

Figure 3.11: Simulated and measured (a) reflection coefficient, AR, gain, efficiency and (b) radiation pattern in xz-plane of the 1 × 4 CP patch antenna array.

the reflection coefficient and the AR of the integrated 1 × 4 array antenna is shown in Figure 3.11(a). The measured overlapping CP bandwidth of 1.67% (29.75 – 30.25 GHz) is exhibited by the designed 1 × 4 CP patch antenna array. Furthermore, the gain of the CP antenna array is measured following the procedure adopted in [82] and a good agreement between simulated and measured gain and efficiency is observed as shown in Figure 3.11(a). The LHCP and RHCP radiation patterns in the xz-plane of the 1 × 4 CP antenna array is measured and is shown in Figure 3.11(b). A measured peak gain and radiation efficiency of 14.1 dBic and 97.45%, respectively is obtained for the designed 1 × 4 CP antenna array.

3.4.2 4 × 4 CP antenna array

A similar procedure discussed in Section 3.4.1 is followed to design a 4 × 4 LP patch antenna array with same substrate material. The schematic of the 4 × 4 is shown in Figure 3.12(a). The overall dimension of the 4 × 4 patch antenna array with the converter is 44 × 44 × 7.62 mm^3 (4.38 × 4.38 × 0.75 λ_o^3). A prototype of the 4 × 4 LP patch antenna array (Figure 3.12(b)) with the polarization converter is fabricated (Figure 3.12(c)) and measured. Figure 3.12(d) shows the measurement set up of the proposed CP antenna array.

The simulated and measured results of the reflection coefficient and the AR of the integrated array antenna is shown in Figure 3.13(a). It can be observed that an impedance

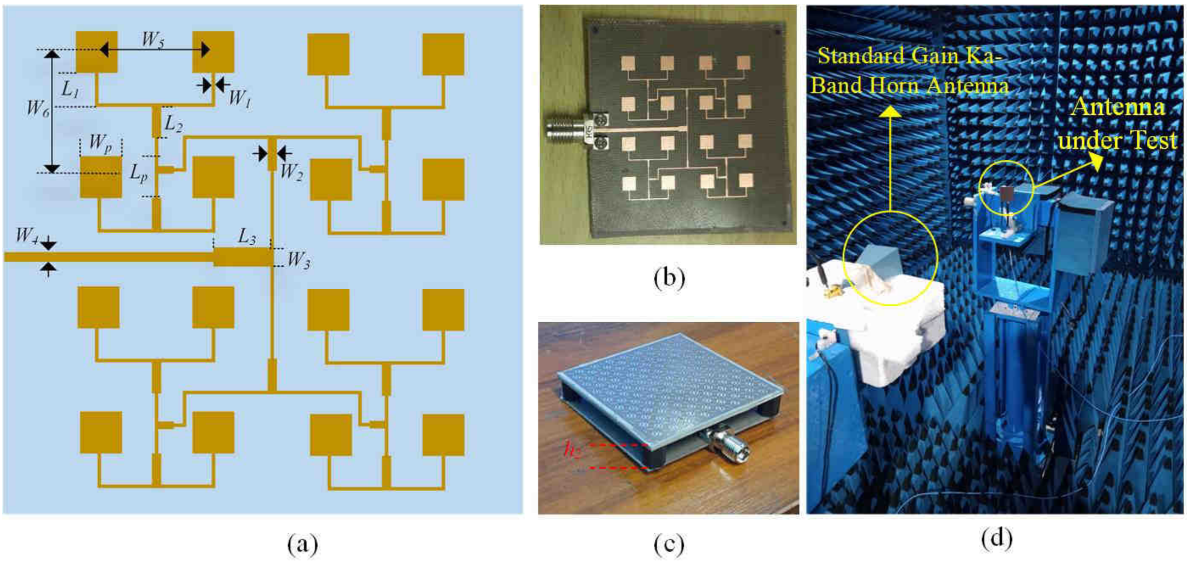

Figure 3.12: (a) Schematic and (b) fabricated prototype of 4 × 4 patch antenna array. (c) Fabricated prototype and (d) measurement setup of 4 × 4 patch antenna array with polarizer. $W_p = L_p = 3.1$, $L_1 = 2.20$, $W_1 = 0.20$, $L_2 = 1.6$, $W_2 = 0.38$, $L_3 = 1.84$, $W_3 = 1.17$, $W_4 = 0.76$ and $W_5 = W_6 = 9$ (all in mm).

bandwidth of 2.03% (29.65 – 30.25 GHz) and ARBW of 2.52% (29.35 – 30.10 GHz) is achieved for the designed CP patch antenna array. Hence, an overlapping CP bandwidth of 1.51% (29.65 – 30.10 GHz) is realized. Furthermore, the gain of the CP antenna array is measured and a good agreement between simulated and measured gain and efficiency is observed as shown in Figure 3.13(a). The measured results of the CP antenna array show that the peak realized gain of 18.7 dBic with the radiation efficiency greater than 96%

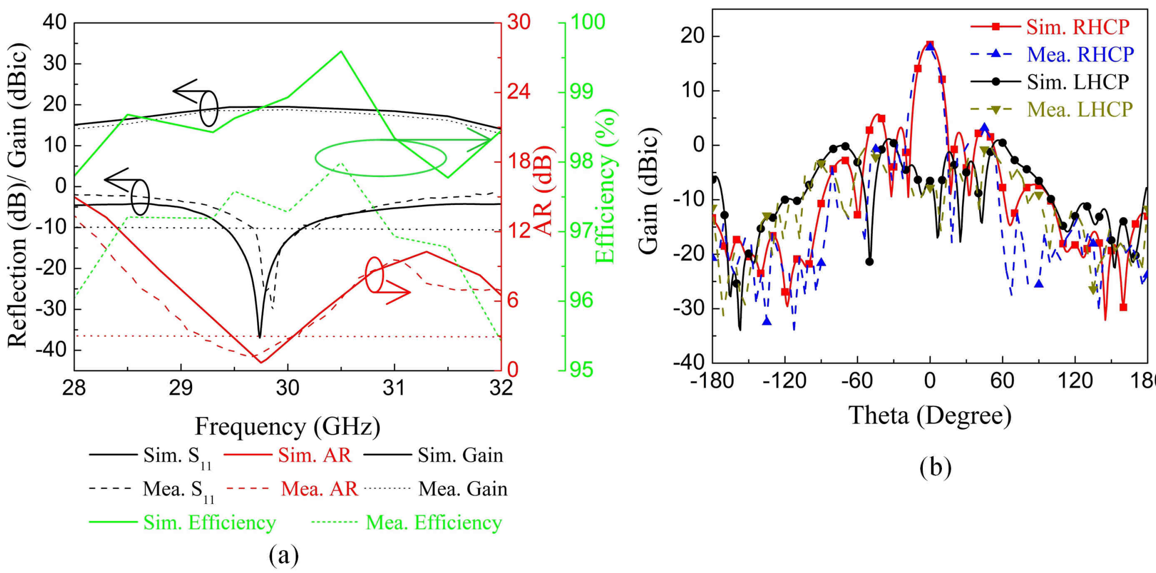

Figure 3.13: Simulated and measured (a) reflection coefficient, AR, gain, efficiency and (b) radiation pattern in xz-plane of the 4 × 4 CP patch antenna array.

are obtained in the frequency band of 28.0 – 32.0 GHz. The LHCP and RHCP radiation patterns in the xz-plane of the CP antenna array is measured and is shown in Figure 3.13(b). It is observed that the difference between LHCP and RHCP radiated fields in the broadside direction is more than 23 dB which depicts a good isolation between them. The measured 3-dB angular beamwidth of 10.19^0 in xz-plane is obtained for the 4×4 CP antenna array. The performance of the proposed CP antenna arrays with some of the CP antenna arrays available in the literature is shown in Table 3.2. The proposed CP antenna array use a LTC polarization converter with simple microstrip feeding and provides high gain and radiation efficiency as compared to [146] – [151] and [167] – [169].

Table 3.2: Performance of the proposed 1×4 and 4×4 CP Antenna Array with the other CP Array antennas available in the literature.

Reference	Frequency (GHz)	Array Scale	Gain (dBic), Efficiency(%)	Note
[146]	17.25	2×2	12.5, > 80	Complex SIW feeding network
[147]	37.5	1×4	12.8, —	Complex SIW feeding
[148]	28.35	4×4	18.2, > 65	Complex SIW feeding with sequential rotation
[149]	25.5	2×2	11.53, —	Complex SIGW feeding
[150]	24.5	8×8	20, 34	Dielectric based inverted microstrip gap waveguide
[151]	30	1×4	7.4, 60	Complex due to grounding vias
[167]	29.25	4×4	14.69, > 84	Complex due to multi-layer structure
[168]	60	4×4	15.98, —	Sequential feeding
[169]	28	1×4	13.5, >76	Complex SIW feeding
Proposed	29.85 30	4×4 1×4	18.7,>96 14.1, >97	Microstrip line feeding

3.5 Conclusion

A compact LTC polarization converter working in transmission mode with oblique incidence response remaining relatively stable up to 45° is studied and its ECM is developed. The polarization converter exhibits ellipticity (e) better than 0.94 ($0.94 < e < 0.98$) and an axial ratio less than 3 dB in the frequency band of 29.50 – 32.65 GHz (10.13%). Furthermore, the converter's 45° rotated 15×15 cells are used as a superstate with a 1×4 and 4×4 LP patch antenna arrays to obtain a CP antenna array showing an RHCP peak gain of 14.1 dBic and 18.7 dBic, respectively. The measured CP overlapping bandwidth of 1.67% (29.75 – 30.25 GHz) and 1.51% (29.65 – 30.10 GHz) is exhibited by 1×4 and 4×4 CP antenna array, respectively. The CP antenna arrays designed using the proposed polarization converter can act as a feed source to a large transmit array for fixed satellite services uplink frequency band (29.5 – 30.0 GHz).

Chapter 4

Dual-band Linear-to-Circular Polarization Converter

In the previous chapter a single-band LTC polarization converter designed and fabricated on single substrate layer has been presented. The work presented here is the extension of the work presented in chapter-3, where a LTC operating around 30 GHz is presented. In this chapter a dual-band LTC is proposed by modifying the unit cell presented in previous chapter.

In this chapter, a compact dual-band LTC polarization converter designed on a single layer substrate is proposed. The unit cell of the converter has a size of $3.72 \times 3.90 \times 1.52$ mm^3 ($0.0072\lambda_o^3$, λ_o is calculated with respect to 20.67 GHz). The converter consists of split-rings with horizontal and vertical metallic strips printed on both sides of a single layer substrate for dual-band operation. The proposed converter has a measured 3-dB ARBW of 5.56% ($20.10 - 21.25$ GHz) in the lower band and 3.97% ($29.12 - 30.30$ GHz) at the upper band. The converter transmits a right hand circularly polarized (RHCP) wave at lower band and left hand circularly polarized (LHCP) wave at the upper band for an LP incident wave. The characteristics of the polarization converter are validated by integrating an array of 7×7 elements of its unit-cell in the end-fire direction of a dual-band LP dipole antenna operating in the same frequency bands like that of the polarization converter. The antenna integrated with the polarization converter exhibits measured CPBW of 7.80% and 6.57% in lower frequency band: $20.10 - 21.75$ GHz and upper frequency band: $29.4 - 31.4$ GHz, respectively. The integrated antenna can act as a feed source of a high gain dual-band transmit-array for uplink ($30.0 - 31.0$ GHz) and downlink (20.2 – 21.2 GHz) of Ka-band military satellite communication.

4.1 Design and Characterization of Dual-Band Linear to Circular Polarization Converter

4.1.1 Theoretical Analysis and Principle of Operation

The topology of the proposed converter is illustrated in Figure 4.1. When a plane wave is incident on it, the transmitted wave would consist of both x- and y-polarized components. Transmission matrix T can be utilized to relate the complex amplitude of incident field to those of the transmitted field [157] as:

$$\begin{bmatrix} E_x^t \\ E_y^t \end{bmatrix} = T \begin{bmatrix} E_x^i \\ E_y^i \end{bmatrix} = \begin{bmatrix} t_{xx} & t_{xy} \\ t_{yx} & t_{yy} \end{bmatrix} \begin{bmatrix} E_x^i \\ E_y^i \end{bmatrix} \tag{4.1}$$

where, $t_{ij} = E_i^t/E_j^i$, the first and second subscripts i and j corresponding to the polarized components of the transmitted and incident fields respectively. The transmitted wave in general can be represented as a composition of two orthogonal components with equivalent magnitude. Hence,

$$\overrightarrow{E^t} = \overrightarrow{E_x^t} + \overrightarrow{E_y^t} = E_0^t(T_x\hat{x} + T_y\hat{y})e^{-jkz} \tag{4.2}$$

where E_0^t is the amplitude and

$$\begin{bmatrix} T_x \\ T_y \end{bmatrix} = \begin{bmatrix} |T_x|e^{j\phi} \\ |T_y|e^{j\phi} \end{bmatrix} \tag{4.3}$$

is the linear transmission matrix. As a result, a phase change of $\triangle\phi = \phi_x - \phi_y$ appears at the output of the converter among two orthogonal components. Therefore, if $|T_x| = |T_y|$ and $\triangle\phi = \pm 90^o$, the polarizer converts an LP incident wave into a CP wave. For a dual-band converter, this condition must be satisfied at both the bands.

Transmission coefficient (T.C) can be expressed as

$$T.C = E^t/E^i \tag{4.4}$$

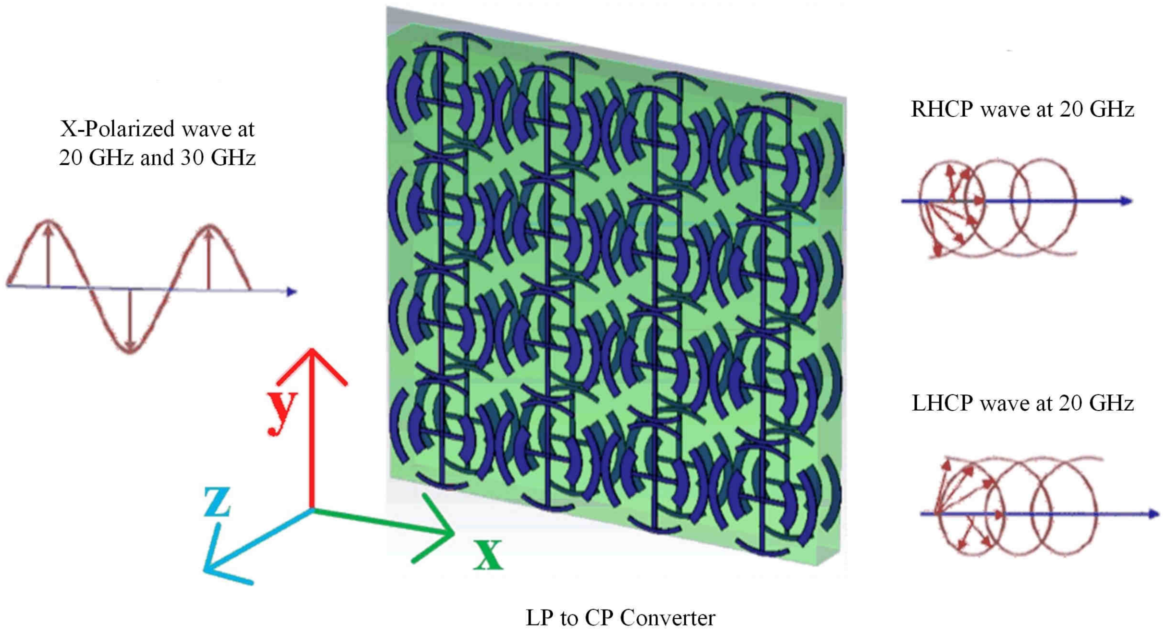

Figure 4.1: Schematic of proposed dual-band linear-to-circular polarizer.

The circularly polarized transmitted wave can be defined as [52]

$$\begin{bmatrix} E^t_{RHCP} \\ E^t_{LHCP} \end{bmatrix} = \begin{bmatrix} E^t_x + jE^t_y \\ E^t_x - jE^t_y \end{bmatrix} = (T.C)_{Circular} \begin{bmatrix} E^i_x \\ E^i_y \end{bmatrix} \tag{4.5}$$

$$\begin{aligned} (T.C)_{Circular} &= \begin{bmatrix} T_{RHCP_x} & T_{RHCP_y} \\ T_{LHCP_x} & T_{LHCP_y} \end{bmatrix} \\ &= 1/\sqrt{2} \begin{bmatrix} T_{xx} + jT_{yy} & T_{xy} + jT_{yy} \\ T_{xx} - jT_{yx} & T_{xy} - jTyy \end{bmatrix} \end{aligned} \tag{4.6}$$

where $1/\sqrt{2}$ in (4.6) is due to power normalization and this equation reveals the ability of the polarization converter to transform an LP wave into a CP wave. Since the proposed polarization converter has negligible cross transmission coefficients ($T_{xy} \approx T_{yx} \approx 0$). Therefore, we have

$$E^t_{RHCP} = 1/\sqrt{2} \left[(T_{xx})E^i_x + (jT_{yy})E^i_y \right] \tag{4.7}$$

$$E^t_{LHCP} = 1/\sqrt{2} \left[(T_{xx})E^i_x - (jT_{yy})E^i_y \right] \tag{4.8}$$

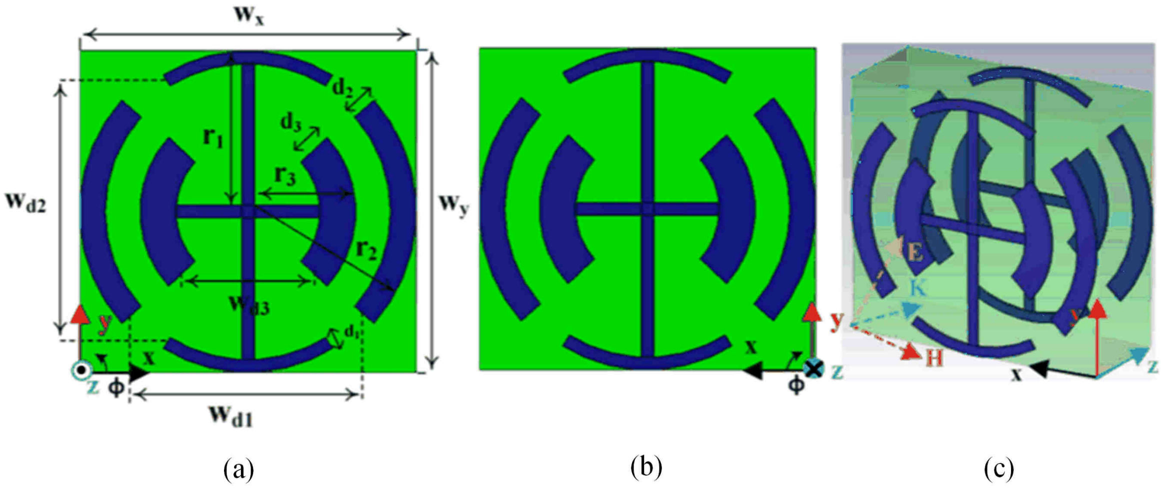

Figure 4.2: Schematic of the proposed dual-band unit-cell for the linear-to-circular polarization converter (a) front, (b) back and (c) perspective view. d_1=0.15, d_2= 0.3, d_3=0.42, r_1=1.86, r_2=1.95, r_3= 1.25, w_{d1}= 2.2, w_{d2}= 3, w_{d3}= 1.35, w_x =3.90, w_y =3.72 (All dimensions are in mm).

4.1.2 Unit Cell Design

The unit cell of the proposed converter is depicted in Figure 4.2. The structure is composed of a single dielectric substrate layer with dimensions along x- and y-direction as w_x =3.90 mm and w_y =3.72 mm, respectively. The material of the substrate is chosen as 1.52 mm thick Diclad 880 with relative permittivity of 2.2 and loss tangent of 0.0009. The metallic split-rings with the strips are printed on both sides of substrate to improve transmission. The conducting material for all metallic strips is 0.035 mm thick copper. The performance of the converter can be shaped by appropriately adjusting the geometrical parameters. Since the design is asymmetric along x-and y-axis, the cell reacts to two orthogonal LP incident waves differently. For the cell to function as LTC polarization converter, the two orthogonally polarized waves should be transmitted with equal amplitude and 90° phase difference between them. To illustrate the CP wave in an instinctive way, the AR is used to reveal the degree of the CP, which is mathematically calculated from (4.9) taking the magnitude of transmission coefficients and phase difference between them into account [153].

$$AR = 10log_{10}\frac{(T_{xx}cos\tau+T_{yy}cos\triangle\phi sin\tau)^2+\ T_{yy}^2 sin^2\triangle\phi sin^2\tau}{(T_{xx}sin\tau+T_{yy}cos\triangle\phi cos\tau)^2-T_{yy}^2 sin^2\triangle\phi cos^2\tau} \tag{4.9}$$

Where, $\tau = 1/2arctan((2T_{xx}T_{yy}cos\triangle\phi)/(T_{xx}^2 - T_{yy}^2))$

4.1.3 Response of the Dual-Band Polarization Converter for a ϕ=45° Polarized Incident Wave

To explore and justify the performance of the dual-band LTC converter full wave simulation is carried out using CST Microwave Studio 2019. An infinite array of this design is simulated under the boundary conditions unit cell along x- and y-directions and open along the z-direction. Due to uneven elements along x- and y-axes the unit cell behaviour is different for two orthogonal LP waves. The cell is excited by an incident wave polarized along ϕ=45° as shown in Figure 4.2. For the cell to act as LTC polarization converter, the orthogonal components of the transmission coefficients should be nearly equal and in phase quadrature.

The design of the proposed dual-band polarization converter is arrived by modifying the split-ring structure as shown in Figure 4.3. Reflection and transmission response

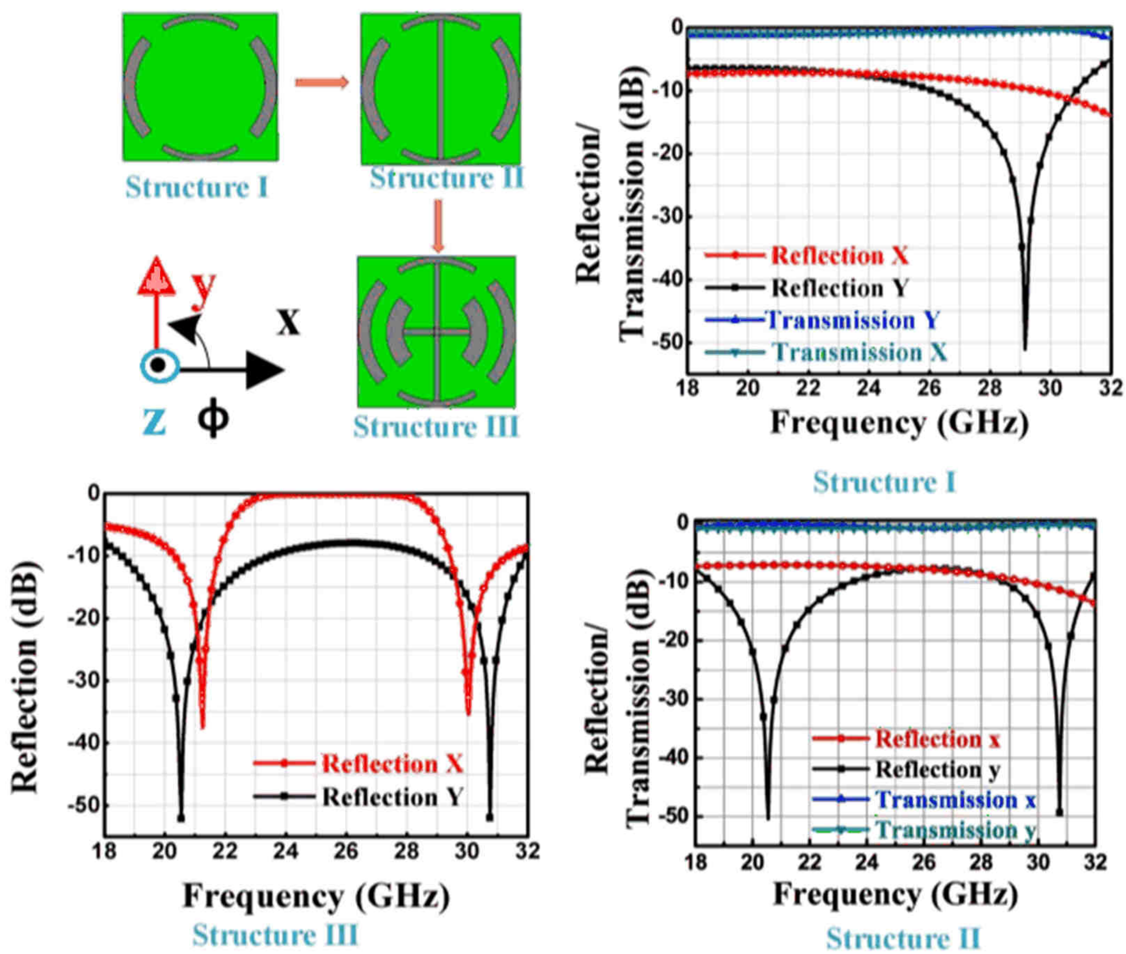

Figure 4.3: Evolution of dual-band LTC polarization converter and their reflection/transmission responses.

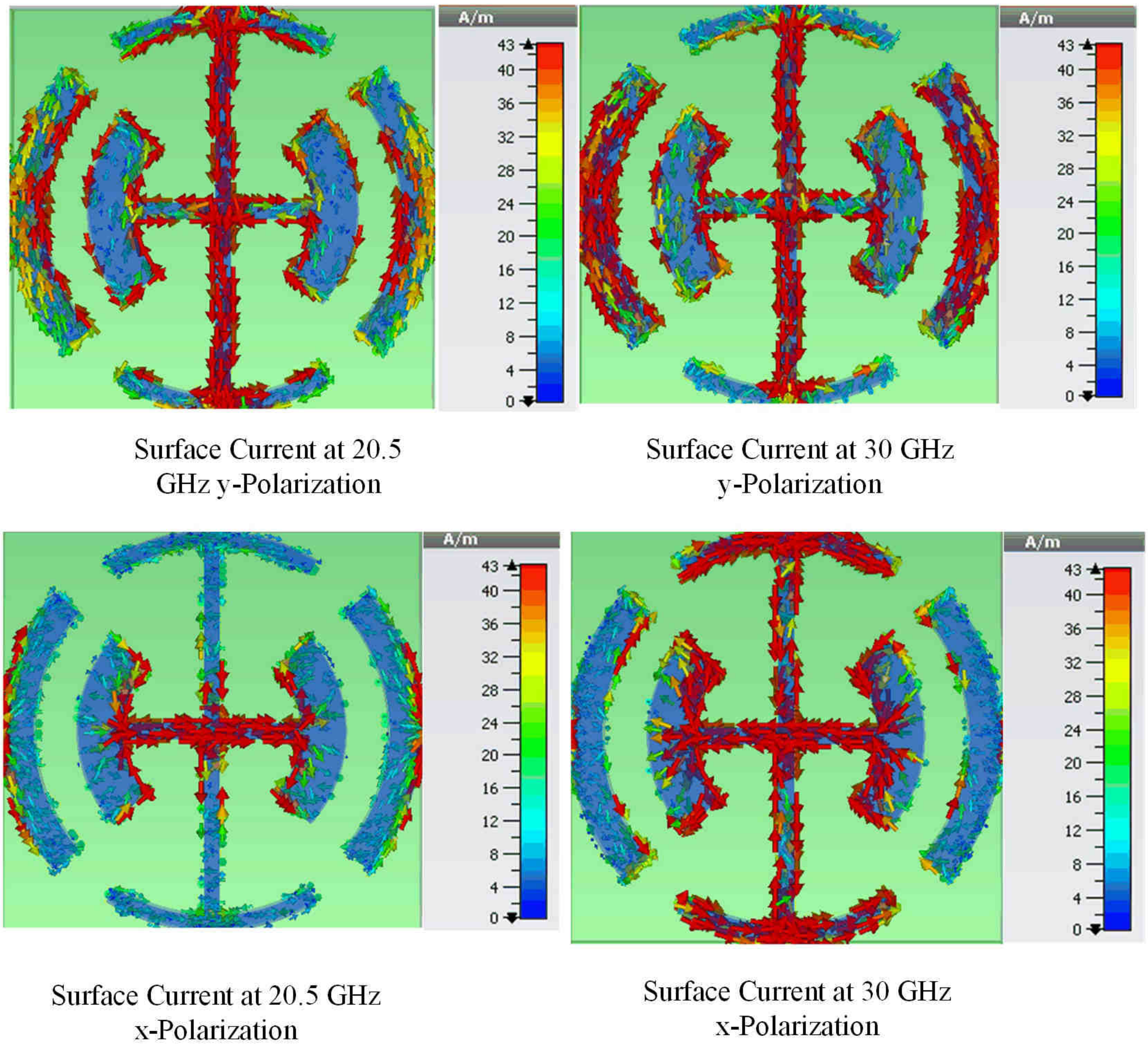

Figure 4.4: Surface current distribution at 20.5 GHz and 30 GHz for y-and x-polarized waves of proposed dual-band LTC polarization converter.

for the different stages of the design are represented in Figure 4.3. It is observed that Structure I show a single band operation at around 30 GHz with reflection below -10 dB and transmission better than -0.5 dB for both x- and y-polarization. Structure II with vertical metallic strip connecting thin metallic strips of outer split-ring excites another frequency band close to 20 GHz with a reflection below -10 dB only for y-polarization. In order to get reflection below -10 dB for both x- and y-polarization horizontal metallic strip and inner split-ring is included in the design (Structure III) representing the final design of dual-band LTC polarization converter.

In order to verify the results shown in Figure 4.4, the surface current distribution along the unit cell of the proposed dual-band LTC polarization converter is examined. As shown in Figure 4.4, for y-polarization of the incident wave at 20.5 GHz the current

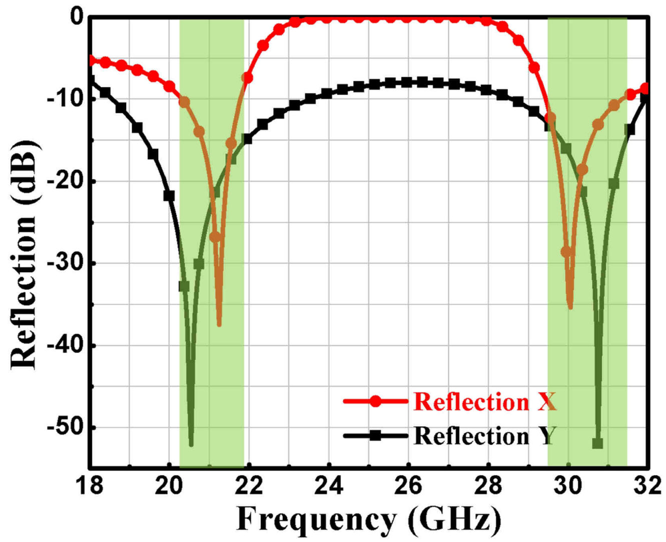

Figure 4.5: Reflection coefficient of proposed dual-band LTC polarization converter.

is more concentrated in the central vertical strip. This verifies that by introduction of vertical dipole in the structure as shown in Figure 4.3, a second resonance is generated around 20 GHz. At 30 GHz for same polarization current is more in thick metallic strips of outer split-ring. For x-polarization, the current is more concentrated in inner split-ring and horizontal strip at 30 GHz and horizontal strip only at 20.5 GHz. This verifies the results as presented in Figure 4.3.

The reflection response of the proposed cell is depicted in Figure 4.5 and it can be observed that in the reflection curve of the cell, there are two frequency bands centered at 20.92 GHz ($\approx$ 20.10 $-$ 21.75 GHz) and 30.25 GHz ($\approx$29.10 $-$ 31.40 GHz) with reflection coefficient lower than -10 dB. The magnitude of transmission coefficients for both of the polarizations are presented in Figure 4.6 and at both the frequency bands, the transmission magnitude remains better than -0.5 dB. The phase difference of 78.2^o $-$ 107.45^o in the lower frequency band: 20.10 $-$ 21.75 GHz and -75.72^o $-$ -95.66^o in the upper frequency band: 29.12 $-$ 31.4 GHz is obtained for the dual-band LTC polarization converter, as depicted in Figure 4.7. It can be observed that in the transmission response, there are two nulls for T_{xx}. A 180^o phase shift is obtained in the transmission of T_{xx}, which can be attributed to the fact that for x-polarized wave, the split-rings in the structure behave as coupled resonators and for y-polarization, they are non-resonant, resulting in the opposite polarizations of the transmitted CP wave in the two frequency bands.

The polarization state of the electromagnetic wave can be represented using (4.1) $-$ (4.3). If the magnitudes of the transmission coefficients T_{xx} and T_{yy} are equal and have

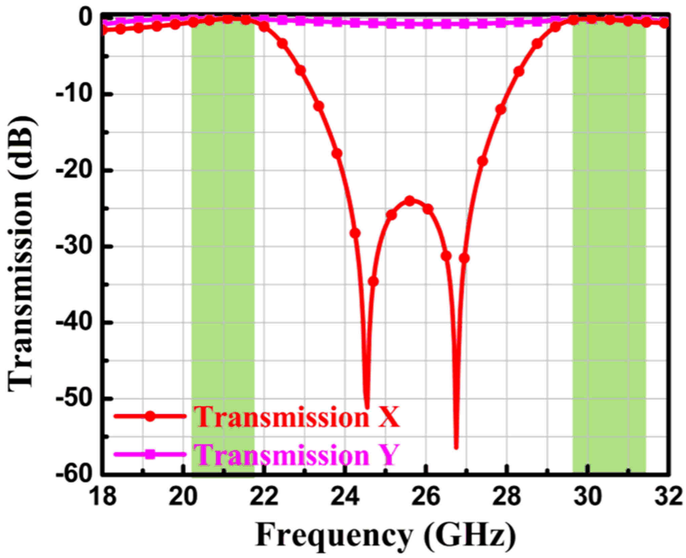

Figure 4.6: Transmission coefficient of proposed dual-band LTC polarization converter.

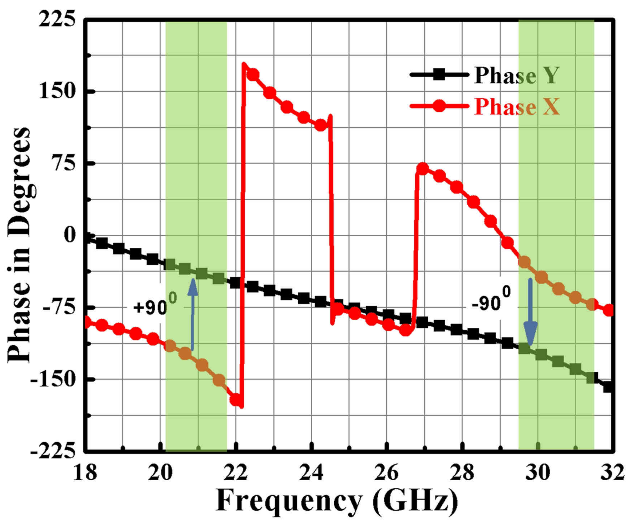

Figure 4.7: Phase response for x- and y-polarized transmitted waves of proposed dual-band LTC polarization converter.

a phase difference of $\pm$ 90^o, the CP wave is generated. Therefore, based on the results as discussed, the cell presents a unique response to x- and y-components of the incident wave and converts the LP incident wave into CP wave with RHCP at lower band and LHCP at the upper band. The AR is calculated from transmisson coefficients using (4.9). Figure 4.8 shows the AR and the transmission phase difference of the proposed dual-band LTC polarization converter. A minimum AR of 0.48 dB and 0 dB is observed at lower and upper frequency band, respectively. This justifies the transmission responses as discussed above.

Another important parameter to characterize the CP wave is the linear to circular

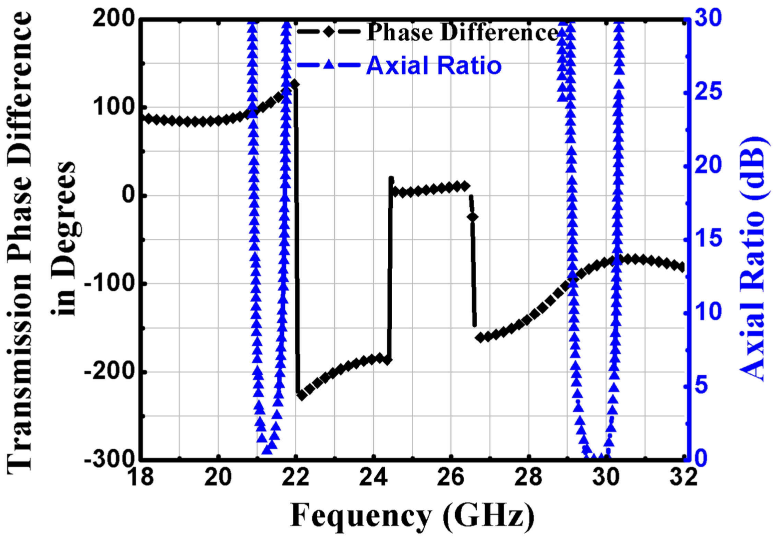

Figure 4.8: Axial ratio and phase difference between x- and y-polarized transmitted waves of proposed dual-band LTC polarization converter.

transmission coefficient. The magnitude of LHCP and RHCP transmission coefficient is calculated following [82], and the result is shown in Figure 4.9 for ϕ=45^o polarized incident LP wave. The magnitude of LHCP transmission remains better than -0.5 dB in the frequency band (29.40 − 31.40 GHz). The RHCP transmission magnitude in the lower frequency band (20.10 − 21.75 GHz) is also better than -0.8 dB. For ϕ=-45^o polarized incident wave, these coefficients will remain the same with the difference that ϕ=-45^o polarized wave will be converted to LHCP wave in the lower frequency band and RHCP in upper frequency band.

4.1.4 Design Guidelines

The design of a dual-band LTC polarization converter by printing identical metallic cells on both sides of a single layer substrate can be achieved by some of the guidelines, as mentioned below.

1. The size of the unit cell of the converter should be close to $0.25\lambda_o \times 0.25\lambda_o$, where λ_o is the wavelength at the lower operating frequency. In the proposed design, the unit cell size is $0.27\lambda_o \times 0.26\lambda_o \times 0.10\lambda_o$ (λ_o is wavelength at 20.67 GHz).

2. The unit cell must exhibit two planes of symmetry. In the present case, the cell is symmetric along xz- and yz-planes, which ensure that there is no cross-coupling between the transmitted component of fields polarized along x- and y-directions.

3. The reflection and transmission coefficients for an incident ϕ=45^o polarized wave must

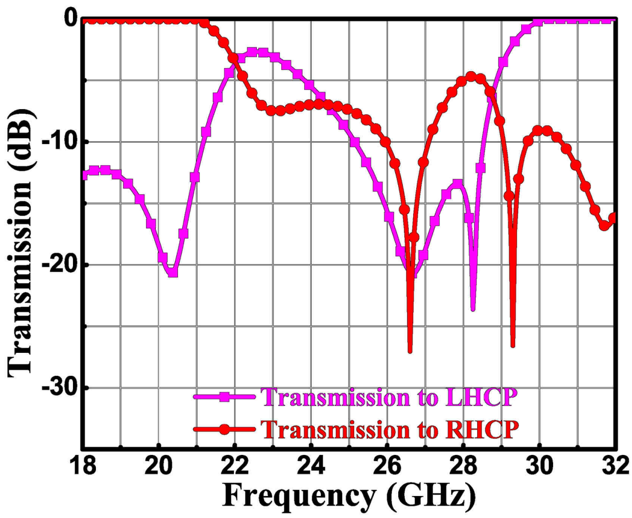

Figure 4.9: Magnitude of LHCP/RHCP transmission coefficients of proposed dual-band LTC polarization converter.

follow the similar behavior as shown in Figure 4.5 and Figure 4.6, respectively.

a. The orthogonal components of the transmitted waves should exhibit two resonances in their reflection coefficient, which should fall within the two operating bands of the polarization converter. In the present design, f_{xr1} = 21.5 GHz and f_{xr2} = 30.45 GHz are lower and upper resonances, respectively in the reflection coefficient for x-polarization. Similarly, the y-polarization has resonances f_{yr1}=20.65 GHz and f_{yr2} = 30.75 GHz. The range of frequencies around f_{xr1} and f_{yr1}, where reflection for both the x- and y-polarization is less than at least -10dB, determines the lower operating band of the polarization converter. In a similar manner, the overlapping frequency range around f_{xr2} and f_{yr2} with reflection less than -10 dB for both the polarization determines the upper frequency range of the converter.

b. The transmission coefficient for one of the orthogonal components should show a non-resonant behavior, while the other one should exhibit two zeros close to the middle of the band. In the present design, the structure shows a non-resonant transmission for y-polarized wave, but shows two zeros (f_{xt1} = 24.90 GHz and f_{xt2} = 27.20 GHz) for x-polarized wave. The value of f_{xt1} and f_{xt2} should lie close to the middle of the band, 0.50 $*$ (f_{c1}+f_{c2}), where f_{c1} and f_{c2} are the center frequencies of lower and upper CP bands, respectively.

c. The presence of two nulls in the transmission coefficient for one of the orthogonal components leads to a phase jump of 180° in the middle of the band of its phase characteristic (Figure 4.6), which results in opposite handedness of transmitted CP waves in

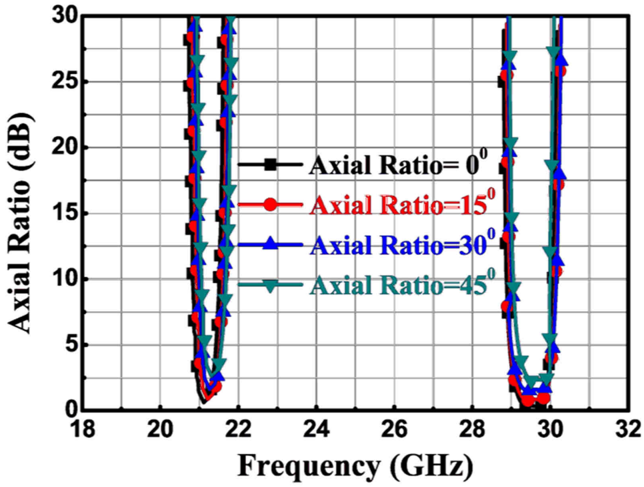

Figure 4.10: Performance of proposed dual-band LTC polarization converter for various incident angles in terms of AR.

the lower and upper bands. In the present design, the transmission response of the cell to an x-polarized wave shows a phase jump of 180° to provide opposite handedness (RHCP at lower band and LHCP at the upper band) at two frequency bands of operation.

In order to design a similar cell with split-rings and a pair of metallic strips for other frequencies, the initial choice of r_1 and r_3 should be done such that $c/2\pi\ r_1 \sqrt{\epsilon_{reff}}) \approx f_{c1}$ and $c/2\pi\ r_3 \sqrt{\epsilon_{reff}} \approx f_{c2}$, where c is speed of light in free space and $\epsilon_{reff} = (\epsilon_r + 1)/2$. The dimensions of the slots of the split-rings can be chosen, such that $w_{d3} \approx 2r_2/3$ (r_2 is

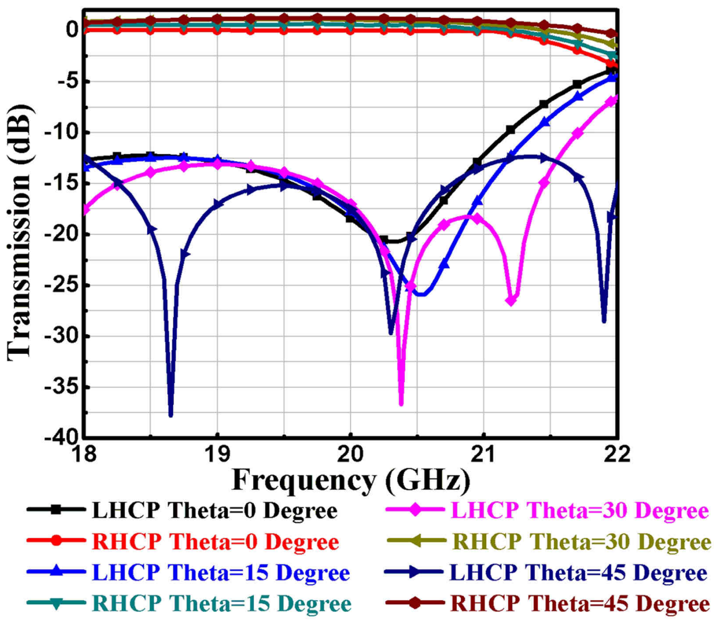

Figure 4.11: Magnitude of LHCP/RHCP transmission coefficients of proposed dual-band LTC polarization Converter for different incident angles (lower band).

initially taken close to r_1), $w_{d2} \approx 3r_2/2$ and $w_{d1} \approx w_{d2}/w_{d3}$. Furthermore, width of the strips: d_1, d_2, and d_3 should obey relations: $d_3/d_2 \approx f_{c2}/f_{c1}$ and $d_1 \approx w_{d3}/10$.

4.1.5 Study under Oblique Incidence

In practice, the incident wave may always not be normal to the plane of the polarization converter. It can be oblique or deflected due to the type of radiation antenna or other sources. Therefore, the performance of the polarization converter under oblique incidence must be studied. The proposed dual-band polarization converter is also analyzed with respect to different incident angle in the xz-plane. Figure 4.10 shows the simulated axial ratio for different incident angle from 0° to 45°. The axial ratio is below 3-dB for incident angle upto 45° at both lower and upper frequency bands of operation. However, AR above 3-dB is obtained for incident angle greater than 45°. Hence angular stability of the proposed dual-band LTC polarization converter can be maintained upto 45° incident angles. The variation of LHCP and RHCP transmission coefficients in the lower and upper frequency bands for different incident angles is also presented in Figure 4.11 and Figure 4.12, respectively. It is observed that the co-polarized transmission better than -1dB is maintained up to an oblique incidence angle of 45°. Therefore, by varying incident angle transmission performance is approximately stable.

4.2 Equivalent Circuit Model (ECM) of Dual-Band Linear to Circular Polarization Converter

The dual-band LTC polarization converter used in this work consists of center connected metallic-strips and therefore it possess weak coupling between orthogonal components [162] of E-fields. Thus, the cross-polarization transmission coefficients of the dual-band LTC polarization converter are negligible. The two metallic layers on the top and bottom of the dielectric substrate provide ample isolation due to the fact that ratio of element length to thickness of dielectric substrate lies within the range of $1.3 - 3.0$ according to [163]. Due to the properties of the polarization converter stated, the equivalent circuit model (ECM) can be separated for x- and y-polarizations. The ECM for x- and y-directions of the dual-band polarization converter is shown in Figure 4.13(a) and Figure 4.13(b), respectively. In the equivalent circuit, L_{x1}, C_{x1} and L_{y1}, C_{y1} are the inductances

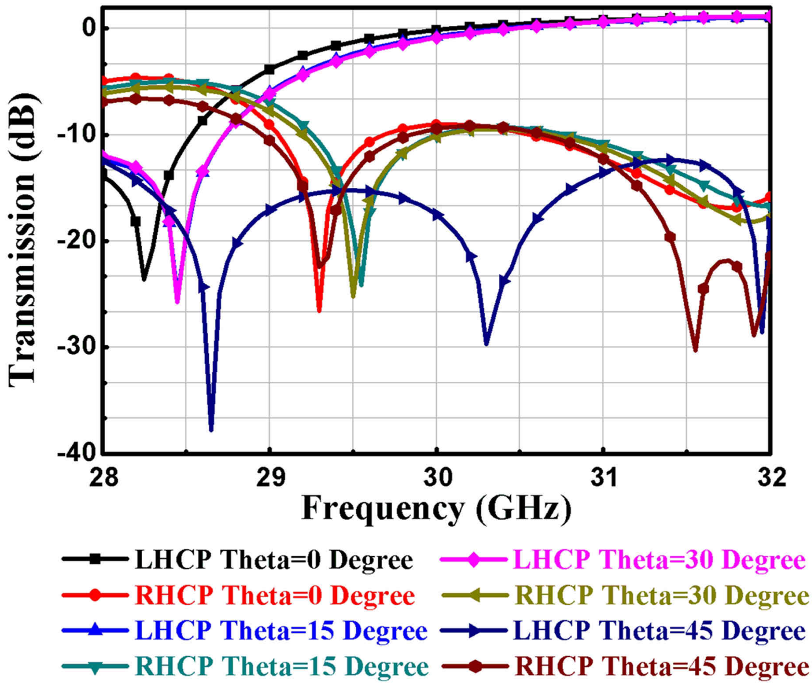

Figure 4.12: Magnitude of LHCP/RHCP transmission coefficients of proposed dual-band LTC converter for different incident angles (upper band).

and capacitances of outer split-ring along x- and y-directions, respectively. C_{x2} is the capacitance between inner and outer split-ring along x-direction while L_{x2} and L_{y2} represent the inductance of inner metalic strip along x- and y-directions, respectively. The dielectric between the top and bottom metal layer is modelled by a transmission line with characteristic impedance Z_d given by (4.10), where Z_0 is free space impedance and ε_r is relative dielectric permittivity. The equivalent circuit of the dual-band LTC polarization converter is simulated in Keysight Advanced Design System (ADS). The initial dimensions of the circuit elements have been approximated using (4.11) and (4.12) [164], where μ_0 and ε_0 represent the permeability and permittivity, respectively of the vacuum, W_x is unit cell length, d_1 is thickness of metallic split-ring along y-axis and $\varepsilon_{eff} = \sqrt{\varepsilon_r + 1)/2}$ is the equivalent permittivity of the substrate.

$$Z_d = \frac{Z_0}{\sqrt{\varepsilon_r}} \tag{4.10}$$

$$L = \frac{\mu_0 W_x}{2\pi} \ln\left(\left(\sin\frac{\pi d_1}{2W_x}\right)^{-1}\right) \tag{4.11}$$

$$C = \frac{2\varepsilon_0 \varepsilon_{eff} W_x}{\pi} \ln\left(\left(\sin\frac{\pi d_1}{2W_x}\right)^{-1}\right) \tag{4.12}$$

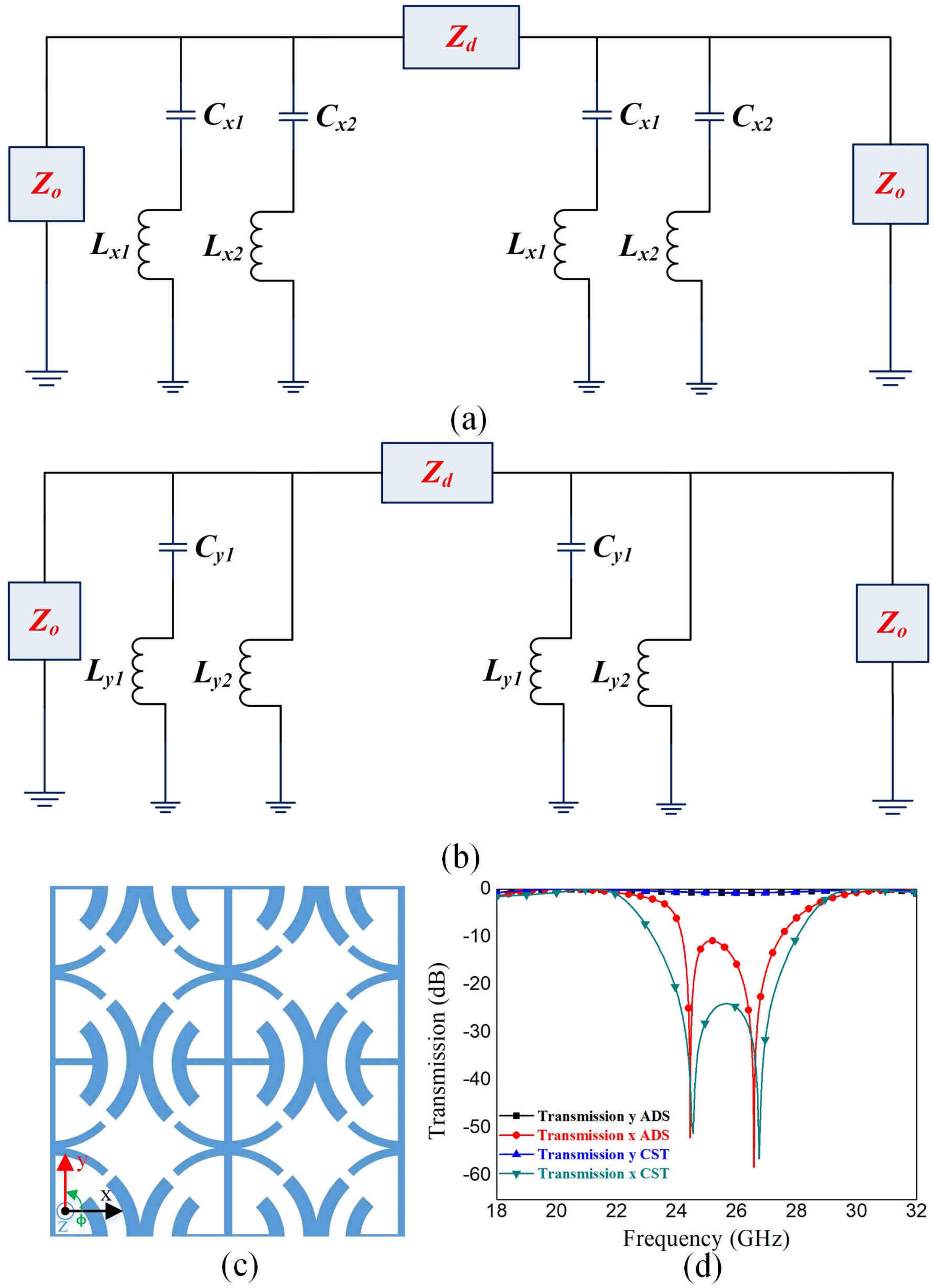

Figure 4.13: (a) Equivalent circuit model of dual-band LTC polarization converter for (a) x-direction ($C_{x1} = 0.5$ fF, $C_{x2} = 4.25$ fF, $L_{x1} = 8.44$ nH, $L_{x2} = 9.6$ nH), (b) y-direction ($C_{y1} = 0.63$ fF, $L_{y1} = 1$ nH, $L_{y2} = 99.94$ nH), (c) ECM model and (d) response of ECM.

The ECM response of the dual-band LTC polarization converter for the x- and y-polarization of incident wave is shown in Figure 4.13(d). The ECM response shows two transmission nulls for x-polarized wave similar to that of response from electromagnetic solver which is required to obtain opposite nature of CP at lower and upper frequency bands. The impedance of the top and bottom metallic layers derived for the x- and y-direction is represented in (4.13) and (4.14), respectively.

$$Z_x = \frac{(1-\omega^2 L_{x1}C_{x1})(1-\omega^2 L_{x2}C_{x2})}{j\omega(C_{x2}+2C_{x1}-2\omega^2 L_{x2}C_{x1}C_{x2}-\omega^2 L_{x1}C_{x1}C_{x2})} \tag{4.13}$$

$$Z_y = \frac{j\omega L_{y2}(1-\omega^2 L_{y1}C_{y1})}{1-\omega^2 C_{y1}(L_{y1}+2L_{y2})}. \tag{4.14}$$

4.3 Experimental Verification of Proposed Dual-Band Linear to Circular Polarization Converter using Standard Gain K/Ka-Band Horn Antennas

In order to validate the proposed design of dual-band LTC polarization converter design, an array of 21 $\times$ 21 elements of unit-cell of the polarization converter introduced in Section 4.1.2 is fabricated using the standard photolithography technique. The array is printed on 1.52 mm thick Diclad 880 substrate material with overall dimensions of the fabricated sample as 78 $\times$ 82 mm^2 as shown in Figure 4.14. As illustrated in Figure 4.15, the transmission coefficient of the fabricated prototype of LTC polarization converter is acquired based on free space measurement technique. A pair of standard gain horn antennas operating in *K/Ka*-band are connected to PNA E8364C from Agilent Technologies to act as transmitting and receiving antenna. The fabricated converter is tested in its transmission mode by placing it in the middle of the two identical *K/Ka*-band standard gain horn antennas so that it lies in the far-field region of both the antennas. The measurement is separately taken in the lower and upper frequency band using K -band and Ka-band horn antennas, respectively. The transmission coefficient without the converter is recorded for calibration purposes.

The simulated and measured magnitude and phase difference of transmission coefficients of the dual-band LTC polarization converter in the frequency band from 18 $-$ 22 GHz is shown in Figure 4.16. It can be seen that the measured results agree well with simulated results, and a phase difference of 82^o $-$ 102.4^o in the frequency range 20.10 $-$ 21.25 GHz is obtained where magnitude of the total transmission coefficient remains better than -1.25 dB. Therefore, based on the results obtained, an RHCP wave is trans-

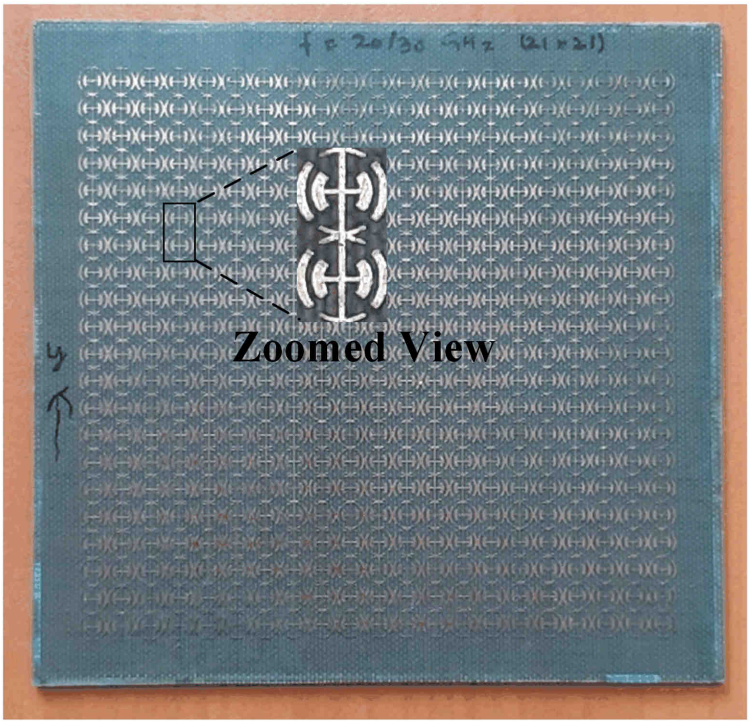

Figure 4.14: Fabricated dual-band LTC polarization converter.

mitted in the frequency band 20.10 − 21.25 GHz. The same measurements are taken in the frequency band from 28 − 32 GHz and the results so obtained are shown in Figure 4.17. The simulated and measured results follow a good concurrence in the frequency range from 29.12 − 30.3 GHz. The transmission magnitude is better than -1 dB in this frequency band with a transmission phase difference of -96^o − -72^o. Therefore, a LHCP wave is transmitted in the upper frequency band from 29.12 − 30.3 GHz. Based on the measured results of magnitude and phase difference of transmission coefficients for x- and y-polarized waves, AR is calculated using (4.9) and the result is shown in Figure 4.18. The minimum AR equal to 0.67 dB and 1.42 dB is obtained at lower and upper operating frequency bands, respectively. The measured 3-dB AR bandwidth is about 5.56% (20.10 − 21.25 GHz) and 3.97% (29.12 − 30.30 GHz) in the lower and upper frequency bands respectively. A widening of AR bandwidth in the lower frequency band in measurement as compared to simulation can be attributed to the consideration of an infinite array of unit-cells in the simulation.

The proposed dual-band LTC polarization converter is also tested in the receiving mode. In the receiving mode, the polarization converter is placed at a distance of 2.5 cm from a standard gain K/Ka-band horn antenna. The polarization converter with the horn antenna acts as the receiver antenna. The transmitting antenna comprises of another

Figure 4.15: Measurement set up for characterization of dual-band LTC polarization converter.

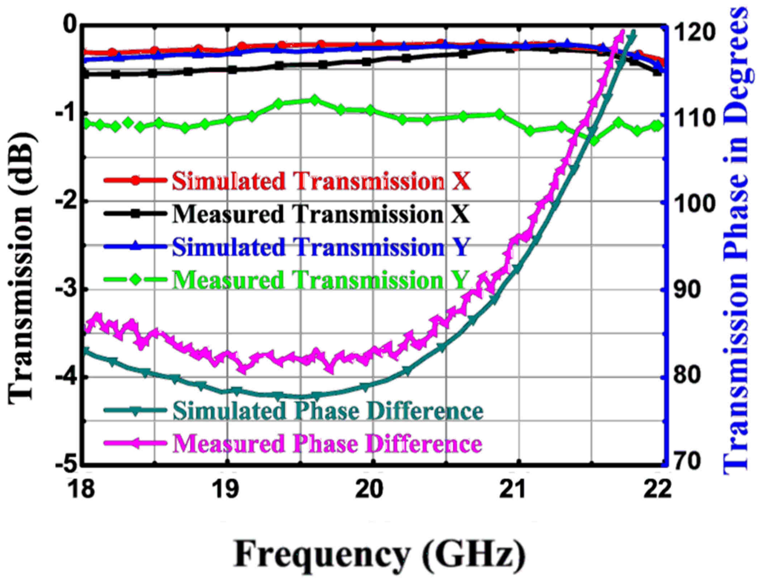

Figure 4.16: Simulated and measured magnitude and phase difference of transmission coefficients for x- and y-polarized waves at lower frequency band of proposed dual-band LTC polarization converter.

standard gain *K*/*Ka*-band horn antenna placed in the far-field of the receiver antenna. The magnitude and phase of the transmission coefficients for the orthogonally polarized (x- and y-polarized) incident waves are recorded and the axial ratio is calculated using (4.9). The axial ratio in the lower and upper frequency bands is shown in Figure 4.19 (a) and (b) respectively, and it can be observed that the axial ratio at both bands is above 15 dB which signifies the linear polarization of the received wave. Hence, it can be concluded that the proposed polarization converter works as LTC polarization converter in transmission mode only.

A comparison of the electrical size and other parameters of the proposed dual-band po-

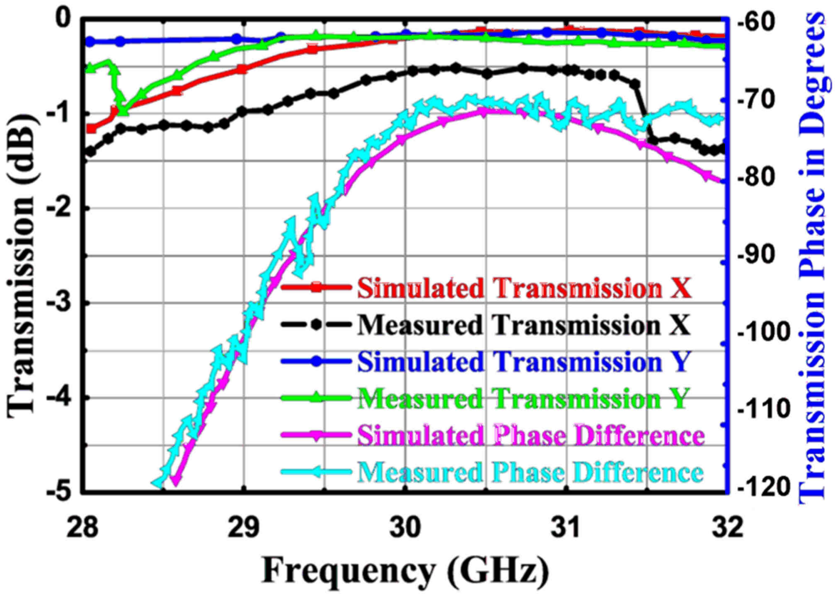

Figure 4.17: Simulated and measured magnitude and phase difference of transmission coefficients for x- and y-polarized waves at upper frequency band of proposed dual-band LTC polarization converter.

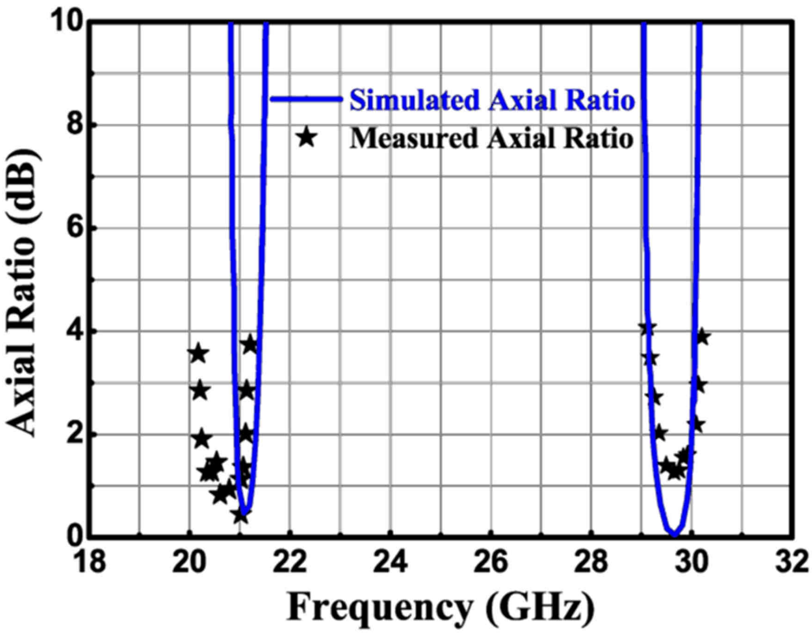

Figure 4.18: Simulated and measured axial ratio of dual-band LTC polarization converter.

larization converter with respect to some of the dual-band polarization converters available in recent literature is presented in Table 4.1. It can be concluded that proposed design of the proposed dual-band polarization converter is compact in terms of volume, composed of only one substrate layer and exhibits a better AR bandwidth as compared to the converter designs available in literature [4] [120], [121], [123] – [125], [129], [130], [170] – [172].

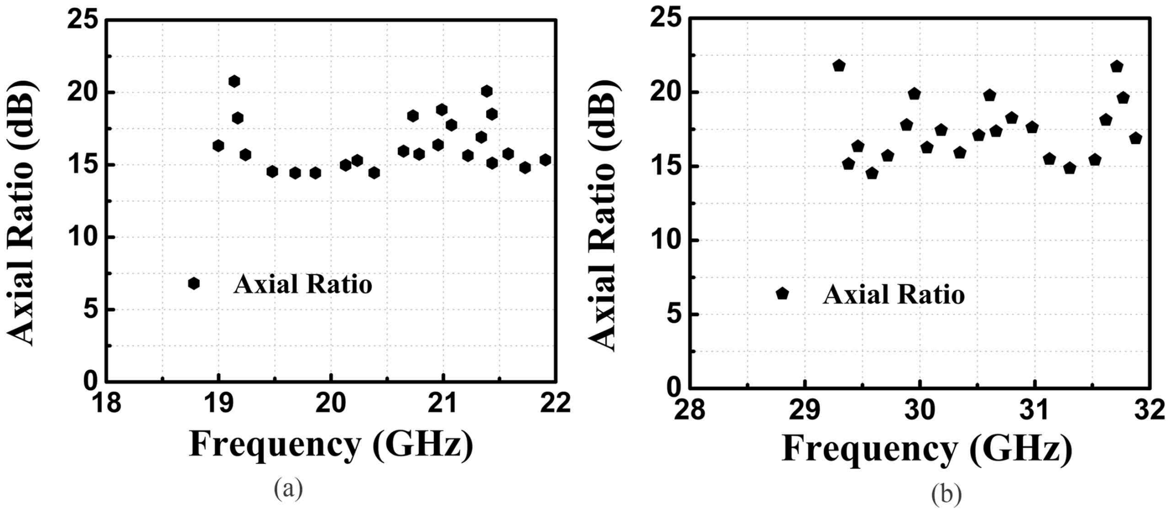

Figure 4.19: Measured axial ratio of the polarization converter in the (a) lower and (b) upper frequency band for the receiving mode.

Table 4.1: Performance Comparison of the Proposed Dual-Band Linear to Circular Polarization Converter with the other Converters available in Literature

Reference	Frequency (GHz)	Number of Substrate Layers	Polarization Modes at Different Frequency Bands	AR Bandwith	Volume of Unit Cell mm^3
[4]	20, 30	2	orth.	4%, 1.3%	$0.0093\lambda_o^3$
[120]	10	7	-	40%	$0.027\lambda_o^3$
[121]	8.4	4	-	64%	$0.0714\lambda_o^3$
[123]	9.77, 11.8	2	orth.	-	$0.0063\lambda_o^3$
[124]	7, 10.9	2	orth.	-	$0.0047\lambda_o^3$
[125]	7.6, 13	4	orth.	31.6%, 13.8%	$0.01248\lambda_o^3$
[129]	19.6, 29.6	5	same	4%, 2.7%	$0.31\lambda_o^3$
[130]	29.8, 39.2	4	same	-	-
[170]	13.1	2	-	112%	$0.0388\lambda_o^3$
[171]	10.75	1	-	-	$0.0084\lambda_o^3$
[172]	18.5, 29	1	orth.	29%, 12%	$0.025\lambda_o^3$
This Work	20.67, 29.71	1	orth.	5.56%, 3.97%	$0.0072\lambda_o^3$

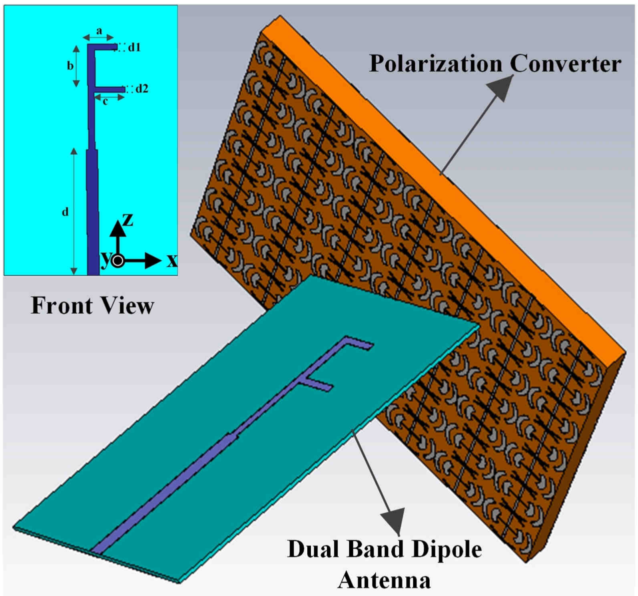

Figure 4.20: Proposed dual-band LP dipole antenna integrated with polarization converter. a= 2.6, b= 3.75, c= 2.65 , d_1=d_2= 0.5, d=11 (All Dimensions are in mm)

4.4 Integration of Proposed Dual Band Polarization Converter with a Dual Band Dipole Antenna

In this section, a dual-band dipole antenna resonating around the center frequencies of dual-band LTC polarization converter introduced in section 4.1.2 is discussed. First, a dual-band LP dipole antenna is designed in CST on a Diclad 880 substrate material having thickness of 0.254 mm. The geometry of this antenna is shown in Figure 4.20. The simulation results obtained are not shown here for brevity. However, it is observed that the antenna resonates in two frequency bands with center frequencies as 21.5 GHz and 30 GHz, where return loss is $-$ 31.50 GHz. The AR observed in the two mentioned frequency band is greater than 20 dB.

Next, this LP dual-band dipole antenna is integrated with the dual-band LTC polarization converter. An array of 7 $\times$ 7 elements of unit-cell of polarization converter introduced in section 4.1.2 is placed in the end-fire direction of the LP dipole antenna, as also depicted in Figure 4.20. The polarization converter is oriented along $\theta = 45^o$, with respect to the axis of the dipole antenna, as shown in Figure 4.20. The $\theta = 45^o$ orientation of polarization converter ensures that the linearly polarized wave of dipole excites the polarization converter diagonally. The simulated results of this integrated antenna reveal that the return loss of the antenna is still better than -10 dB in the frequency bands:

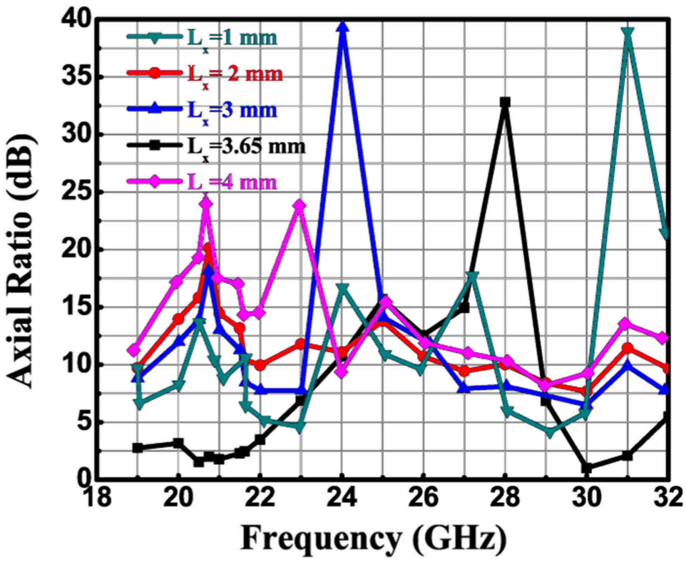

Figure 4.21: Variation of the axial ratio (in the end-fire direction) with the change in the spacing between the dipole and polarization converter.

20.10 − 22.75 GHz and 27.10 − 31.30 GHz. The AR lower than 3-dB is obtained in the lower frequency band: 19.10 − 21.90 GHz and upper frequency band: 29.30 − 31.75 GHz.

The effect of distance between dipole and polarization converter on the axial ratio in the end-fire direction has been studied. The variation in the axial ratio with the change in the spacing of the converter and dipole (L_x) is shown in Figure 4.21. It can be observed that the minimum value of the axial ratio in the lower and upper frequency bands is obtained for $L_x = 3.65$ mm. For values of L_x, less than and more than 3.65 mm, the axial ratio increases, at both the frequency bands of operation indicating that dipole transmits LP waves without being transformed into CP waves. The optimum distance: $L_x = 3.65$ mm at which polarization converter is placed from the dipole antenna is nearly equal to $\lambda_o/4$ (λ_o being the free space wavelength corresponding to the central frequency of lower frequency band).

A prototype of the LP dipole antenna is fabricated, as shown in Figure 4.22. Next, an array of 7 × 7 elements of the unit-cell of polarization converter is fabricated, integrated with this designed LP dipole antenna, and tested to validate the results obtained in simulation. The photograph of the fabricated dual-band LP dipole antenna integrated with the polarization converter is shown in Figure 4.23. The reflection coefficients of this prototype are measured using PNA E8364C. The simulated and measured results of the reflection coefficient of the dual-band LP dipole antenna integrated with the polarization converter are shown in Figure 4.24. The measured fractional impedance bandwidth of

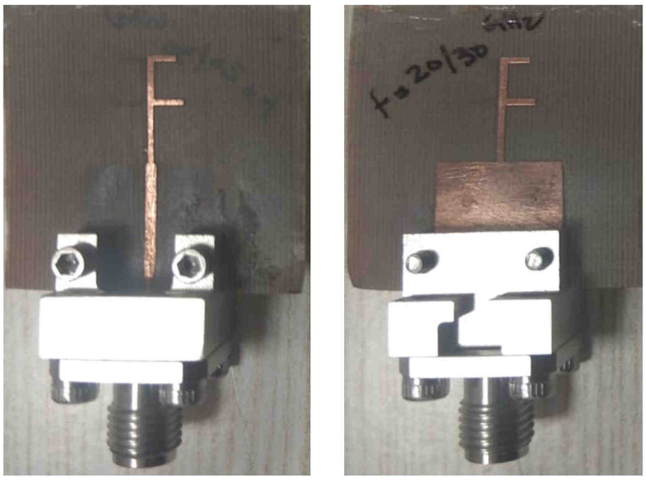

Front View of LP Dipole Antenna **Back View of LP Dipole Antenna**

Figure 4.22: Fabricated prototype of dual-band LP dipole antenna.

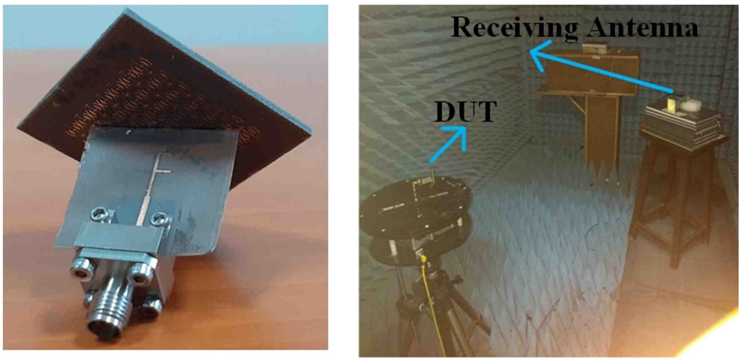

Fabricated CP Dipole Antenna **Measurement of CP Dipole Antenna**

Figure 4.23: Fabricated prototype of dual-band LP dipole antenna integrated with polarization converter.

the antenna is 22.22% (20.0 − 25.0 GHz) and 9.05% (29.0 − 31.75 GHz) in the lower and upper frequency band, respectively. The simulated and measured AR of dual-band LP dipole antenna with the polarization converter is illustrated in Figure 4.25. It can be observed that in the operating frequency bands, there is a close agreement between the simulated and measured axial ratios. The measured 3-dB axial ratio bandwidths of 7.80% (20.10 − 21.75 GHz) and 6.57% (29.4 − 31.4 GHz) are obtained in lower and upper frequency bands, respectively. The measured axial ratio bandwidths lie within respective impedance bandwidths of both the bands and can thus be treated as operating CP bandwidths of the dual-band CP antenna.

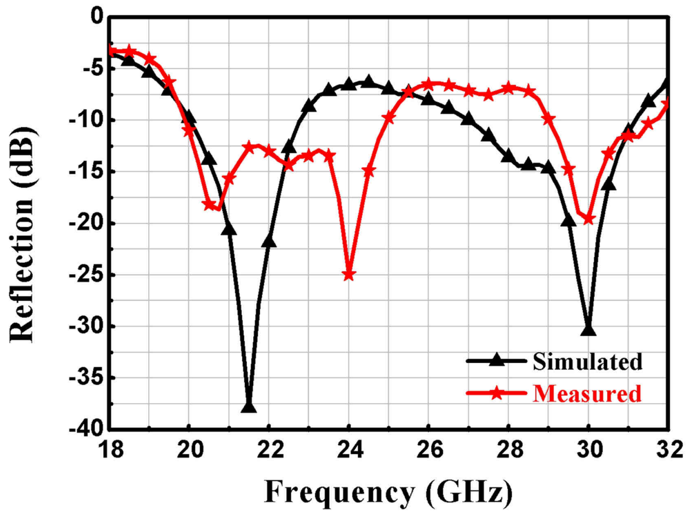

Figure 4.24: Reflection coefficient of dual-band LP dipole antenna integrated with polarization converter.

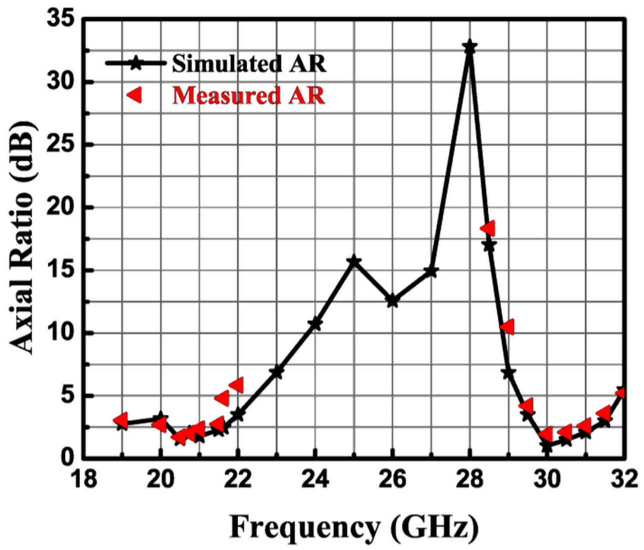

Figure 4.25: Axial ratio of dual-band LP dipole antenna integrated with polarization converter.

4.5 Conclusion

In this chapter, a single substrate layer dual-band LTC polarization converter capable of generating dual CP waves is presented. The proposed polarization converter functions in transmission mode and transforms an LP wave into orthogonal CP waves in two frequency bands for 45° polarization of the incident wave. For -45° polarization of the incident wave, the polarization reversal in the two frequency bands can be obtained. These features are most suited for satellite communications. The unit-cell of the proposed dual-band polarization converter is compact, having a volume of $0.0072\lambda_o^3$. An array of 21 $\times$ 21 elements of unit-cell of proposed polarization converter with overall dimensions of 78 $\times$ 82 mm^2 is fabricated and measured using a pair of standard gain K/Ka-band horn antennas. Furthermore, the presented polarization converter is single substrate layered reducing the fabrication complexity associated with multilayered structures, exhibits a better AR bandwidth and less volume of the unit cell as compared to reported designs available in literature [4], [120], [121], [123] − [125], [129], [130], [170] − [172].

The proposed dual-band polarization converter is integrated with a dual-band LP dipole antenna with overlapping operating bands to arrive at the design of a dual-band CP antenna. The CP antenna exhibits measured CP bandwidths of 7.80% (20.10 − 21.75 GHz) and 6.57% (29.4 − 31.4 GHz) in lower and upper frequency bands, respectively. The proposed dual-band CP antenna which is a combination of a dual-band LP antenna with a dual-band LTC polarization converter can act as a feed element to illuminate a highly directive dual-band transmit-array designed in the uplink (30.0 − 31.0 GHz) and downlink (20.2 − 21.2 GHz) military satellite communication bands. Thus, the proposed feed element along with a transmit-array can be useful as a ground station antenna for the *Ka*-band satellite communication [173] − [178].

Chapter 5

Orthogonal Circularly Polarized Dual-Band Four-Port MIMO Antenna

In the previous chapter, a dual-band LTC polarization converter with orthogonal circular polarization at the lower and upper frequency bands of operation is discussed. In the present chapter, the polarization converter explained in chapter 4 is utilized to design a four port dual-band CP MIMO antenna. A dual-band circularly polarized (CP) four-port multiple-input multiple-output (MIMO) antenna for K/Ka-bands fixed-satellite service is proposed in this chapter. The single element of MIMO is composed of a cascade of two dipoles of different lengths resonating at around 20 and 30 GHz. An array of 7×7 elements of the unit cell of dual-band LTC polarization converter is placed at a distance of $\lambda_o/4$ (λ_o is calculated with respect to 19.51 GHz) in the end-fire direction of MIMO antenna to obtain an orthogonal CP wave at the two frequency bands. The proposed CP antenna shows good MIMO performance with correlation coefficient (CC) less than 0.19 and diversity gain (DG) better than 0.97 at both the frequency bands. The four-port MIMO also agrees with polarization and spatial diversity, and the CP nature at lower and upper frequency bands can be interchanged by exciting the orthogonal ports. A prototype of the MIMO antennas is fabricated and the measured CPBW of 11.51% and 3.69% is obtained in the lower ($19.65 - 22.05$ GHz) and upper ($29.25 - 30.35$ GHz) frequency bands, respectively. The proposed antenna can be used for Ka-band: $29.5 - 30.0$ and $19.7 - 20.2$ GHz fixed satellite service as uplink and downlink frequencies, respectively.

5.1 Design and CP Mechanism of Proposed MIMO

5.1.1 Four-Port CP MIMO Design

The radiating element of the proposed MIMO consists of an F-shaped dipole as shown in Figure 5.1(a) formed by cascading two dipoles of different lengths to achieve dual-band operation. The planar half-dipoles are fed by striplines on top and bottom, constituting

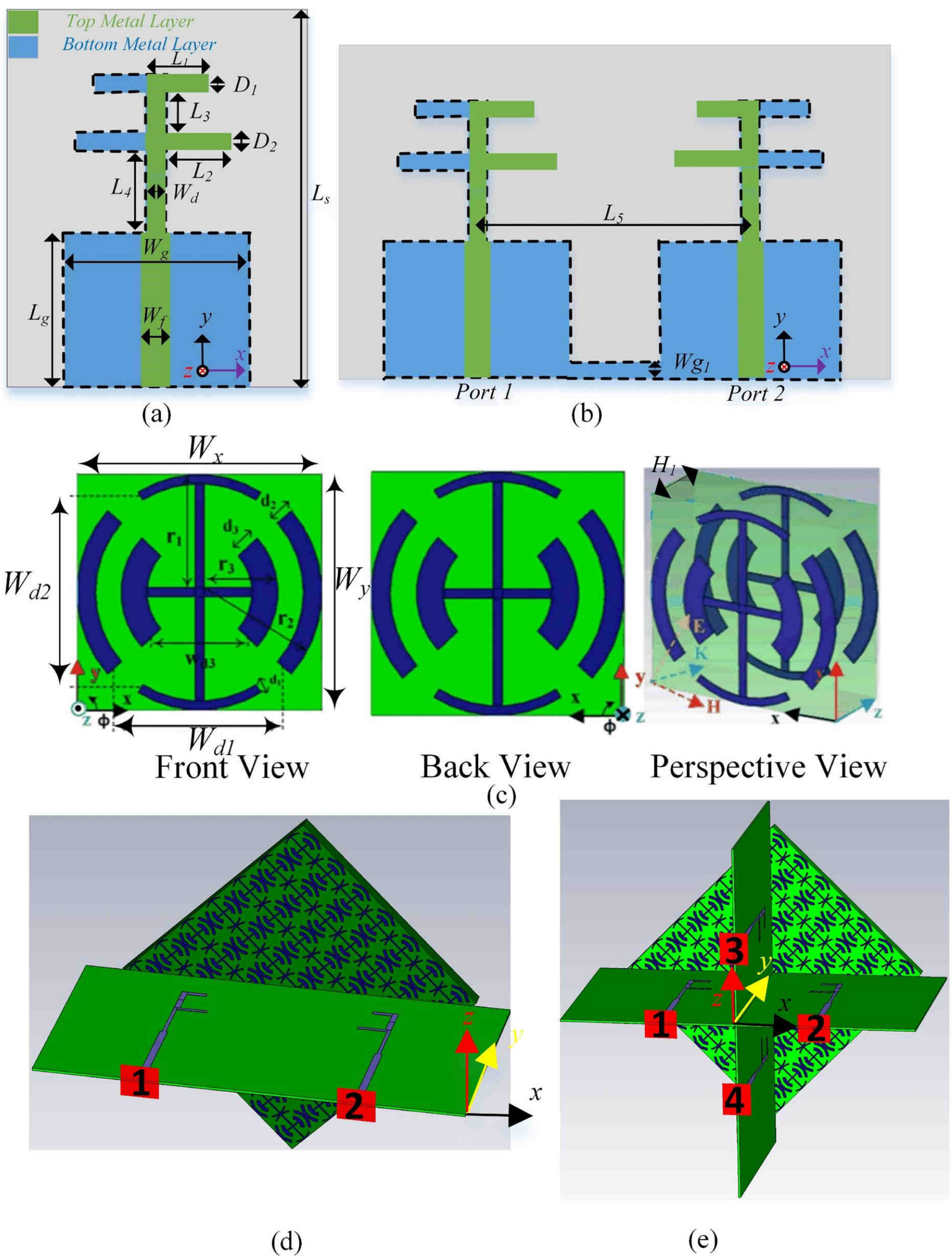

Figure 5.1: Schematic of (a) single element of MIMO, (b) two-port MIMO and (c) unit-cell of dual-band linear-to-circular polarization converter. Perspective view of CP MIMO antenna (d) two-port and (e) four-port. $L_1 = 2.05, L_2 = 3.13, L_3 = 3.75, L_4 = 5.5, L_5 = 19.60, D_1 = 0.5, D_2 = 0.4, W_d = 0.35, W_f = 0.75, W_g = 11, L_g = 11, L_s = 23.85, H_1 = 1.52, W_{g1} = 0.5, d_1 = 0.15, d_2 = 0.3, d_3 = 0.42, r_1 = 1.86, r_2 = 1.95, r_3 = 1.25, W_{d1} = 2.2, W_{d2} = 3, W_{d3} = 1.35, W_x = 3.90, W_y = 3.72$ (all dimensions are in mm).

two back-to-back F-shaped dipoles separated by a dielectric layer of Diclad 880, with dielectric permittivity equal to 2.2 and loss tangent equal to 0.0009. Analysis of the radiating element shows that the operating frequency of the antenna is determined by lengths of the dipoles L_1 and L_2. Upper and lower frequency resonances are controlled by the shorter and longer dipole, respectively. The schematic of the two-port MIMO antenna is shown in Figure 5.1(b). It consists of two dual-band dipole antennas placed in parallel at a distance of L_5 ($1.27\lambda_o$ at the lowest operating frequency of the antenna). The dual-band transmissive LTC polarization converter unit cell used to convert the LP wave from the dipole antenna into CP wave is shown in Figure 5.1(c). The unit-cell of the converter is designed using the same substrate as that of the dipole antenna with thickness H_1. The dual-band polarization converter is composed of split-rings and metallic strips that are printed on both sides of the substrate to improve transmission. Furthermore, an array of 7×7 elements of the unit cell of the dual-band polarization converter is positioned at H_2 ($\lambda_o/4$) from the dipole in the end-fire direction of the antenna. The array is rotated with respect to the z-axis so that the incident wave strikes the polarization converter at 45^o. Initially a two-port CP MIMO antenna is designed as shown in Figure 5.1(d) which is then transformed into a four-port by placing another two-port MIMO antenna orthogonal to it so that all four MIMO elements are placed at orthogonal to each other with common ground plane (See Figure 5.1(e)). The results of two-port CP MIMO are not shown here for brevity.

5.1.2 Linear to Circular Polarization Converter

The 7×7 array of unit-cell shown in Figure 5.1(c) placed in the end-fire direction of the antenna acts as LTC polarization converter. The converter divides the LP wave from dipole antenna into two orthogonal components of equal magnitude with a phase difference of $\pm 90^o$ thereby generating a CP wave in the working frequency. The transmission magnitudes for x- and y-polarization are nearly identical as shown in Figure 5.2(a) in the lower frequency band ($19.0 - 22.0$ GHz) and upper frequency band ($29.0 - 31.0$ GHz), while the phase difference between them as shown in Figure 5.2(b) is -90^o and $+90^o$ in the lower and upper frequency bands, respectively. This meets the criteria of CP conversion of a LTC polarization converter expressed as $|T_x| = |T_y|$, $\phi(T_x) - \phi(T_y) = \pm 90^o$, where T_x and T_y represent the transmission coefficients for x- and y-polarizations, respectively

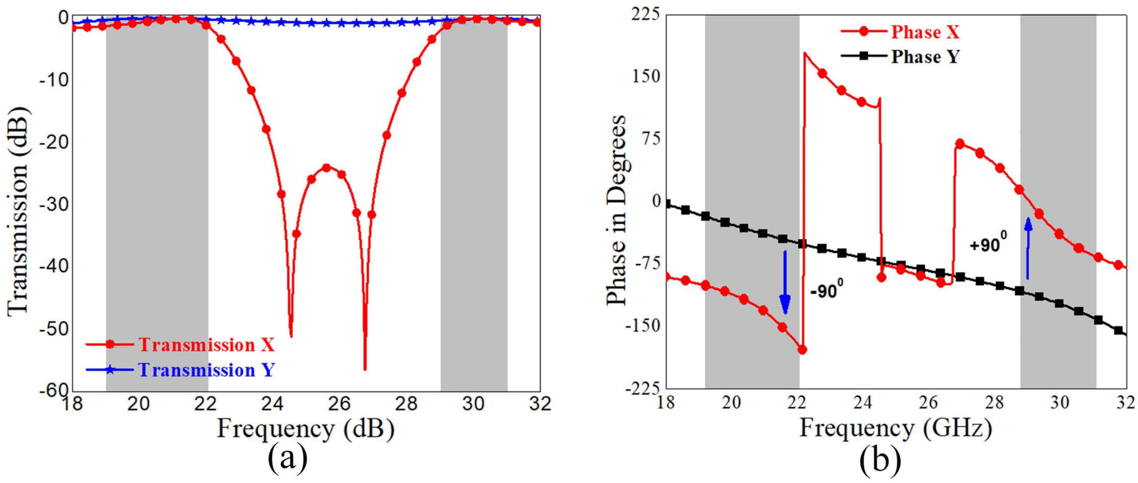

Figure 5.2: Simulated (a) transmission coefficients and (b) phase of dual-band linear-to-circular polarization converter.

[179]. Hence, a left-hand circular polarization (LHCP) and right-hand circular polarization (RHCP) is achieved at lower and upper operating frequency bands, respectively. It is to be noted that the orthogonal CP can be reversed by changing the polarization of the incident wave.

5.2 Numerical Results and Experimental Validation of four-port CP MIMO Antenna

The proposed CP MIMO antenna is simulated using CST Microwave Studio. The perspective view of the proposed MIMO is shown in Figure 5.3(a). A prototype of the proposed MIMO is fabricated as shown in Figure 5.3(b) using the photolithographic procedure. The antenna elements and an array of 7×7 unit cells of dual-band LTC polarization converter are fabricated on Diclad 880 dielectric material of thickness 0.254 mm and 1.524 mm, respectively. The S-parameters are tested by Keysight N5224B PNA. The simulated and the measured S-parameters of the two-port and four-port CP MIMO antenna are depicted in Figure 5.4(a) and Figure 5.4(b,c), respectively. It is observed that two resonant frequencies centered at 20.0 GHz and 30.25 GHz are achieved. The two resonance frequencies are obtained because of the different lengths of two dipoles in the cascaded configuration. This is also verified from the surface current distribution over the dipole as shown in Figure 5.4(d). The current is more concentrated over the lengths L_2 and L_1 at 20 and 30 GHz, respectively. Hence, the lengths L_2 and L_1 are responsible for the generation

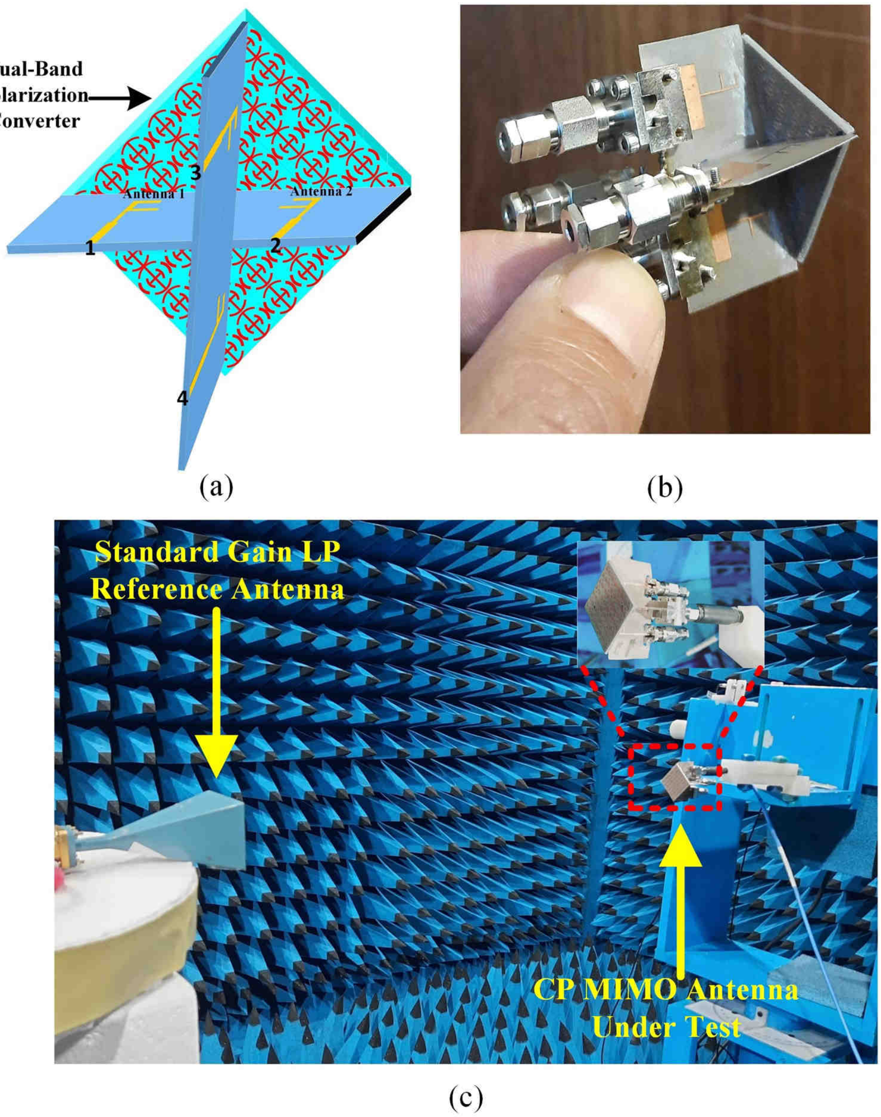

Figure 5.3: (a) Perspective view, photograph of (b) fabricated prototype and (c) measurement setup of the four-port dual-band CP MIMO antenna.

of the resonant frequencies. For the four-port antenna, impedance matching (S_{11} < -10 dB) is achieved for two frequency bands ranging from 18.62 − 20.40 GHz in the lower frequency band and 27.15 − 30.35 GHz in the upper frequency band corresponding to fractional impedance bandwidths of 9.12% and 11.13%, respectively. The antenna covers two major satellite communication bands for uplink (29.5 − 30.0 GHz) and downlink (19.7 − 20.2 GHz) dedicated to fixed satellite services. The measured isolation among all the ports is better than -19 dB and -23 dB in the lower and upper frequency bands, respectively as can be seen from Figure 5.4(c).

The CP performance of the antenna characterized by the axial ratio (AR) is depicted in Figure 5.5(a) and 5.5(b). It can be observed that simulated and measured AR agree

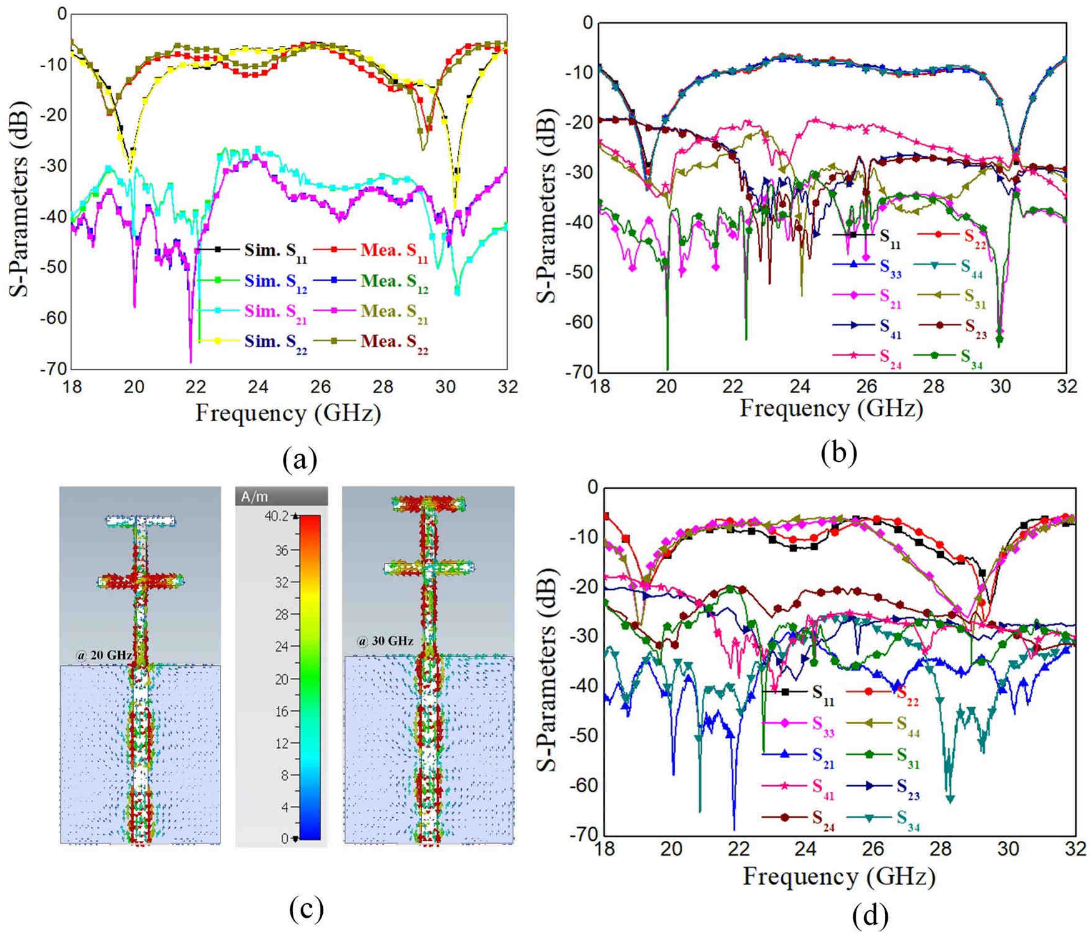

Figure 5.4: (a) Simulated and measured S-parameters of dual-band two-port CP MIMO antenna. S-parameters of four-port CP MIMO antenna (b) simulated and (c) measured. (d) Surface current distribution at 20 and 30 GHz of single element of dual-band CP MIMO antenna.

well in the lower frequency band (19.65 − 22.05 GHz) and upper frequency band (29.25 − 30.35 GHz). Hence, the measured CPBW of 11.51% in the lower frequency band and 3.69% in the upper frequency band is realized for the fabricated dual-band four-port CP MIMO antenna. The overlapping CPBW of 3.74% and 3.69% is obtained respectively, in the lower (19.65 − 20.40 GHz) and upper (29.25 − 30.35 GHz) frequency band. The variation of gain with frequency for the proposed CP MIMO antenna is depicted in Figure 5.5(a) and Figure 4.5(b) at lower (18.0 − 22.0 GHz) and upper (28.0 − 32.0 GHz) frequency bands, respectively. The measured gain of 5.75 dBic and 4.77 dBic is obtained at 20 and 30 GHz, respectively measured along the direction $\theta = 90°$ and $\phi = 90°$.

The isolation performance of an antenna element in a MIMO configuration is described by ρ (cross-correlation (CC)), which determines the achieved channel capacity. For a MIMO antenna zero value of CC is desired, however, a value of CC less than 0.5 is acceptable for MIMO. The CC of the proposed MIMO based on far-field radiation pat-

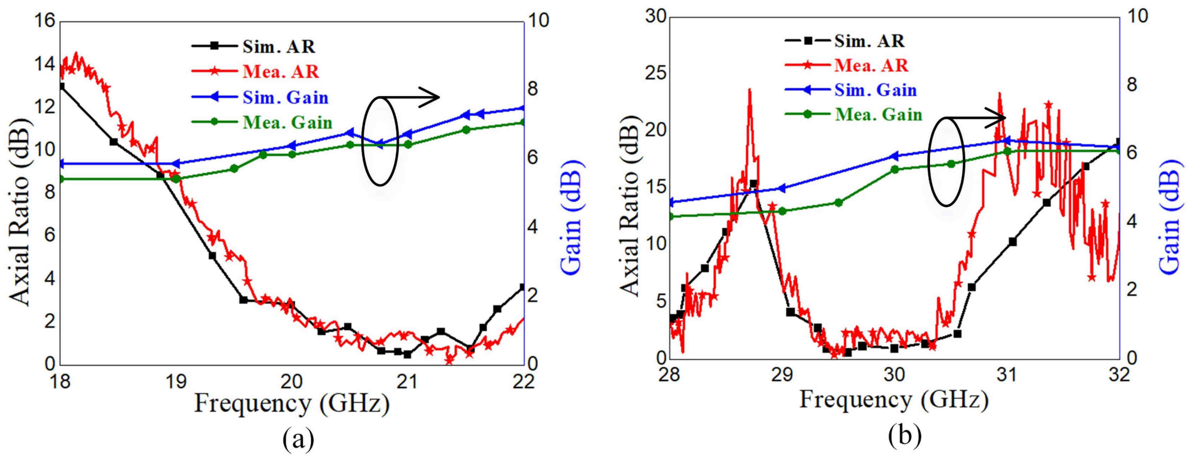

Figure 5.5: Axial ratio and gain of dual-band four-port CP MIMO antenna at (a) lower frequency band and (b) upper frequency band.

terns [180] is evaluated using (5.1), where Ω is the solid angle, E_{porti} is the far-field of the antenna if port i is fed, and E_{portj} is the far-field if port j of the antenna is excited. The normalization of correlation integral is performed with respect to radiated powers of the excitation port with the other ports terminated in a matched load.

$$\rho_{\text{port}i,\text{port}j} = \frac{\frac{1}{2Z_0}\iint\limits_{\Omega} E_{\text{port}i}.E^*_{\text{port}j}d\Omega}{\sqrt{P_{\text{rad,port}i}}\sqrt{P_{\text{rad,port}j}}} \tag{5.1}$$

The CC among all the antennas of the proposed four-port CP MIMO system falls within the acceptable value in the lower and upper frequency bands respectively, as shown in Figure 5.6(a) and Figure 5.6(b). The diversity gain (DG) is another metric linked to the MIMO system that describes the effect of the diversity scheme on the transmitted power.

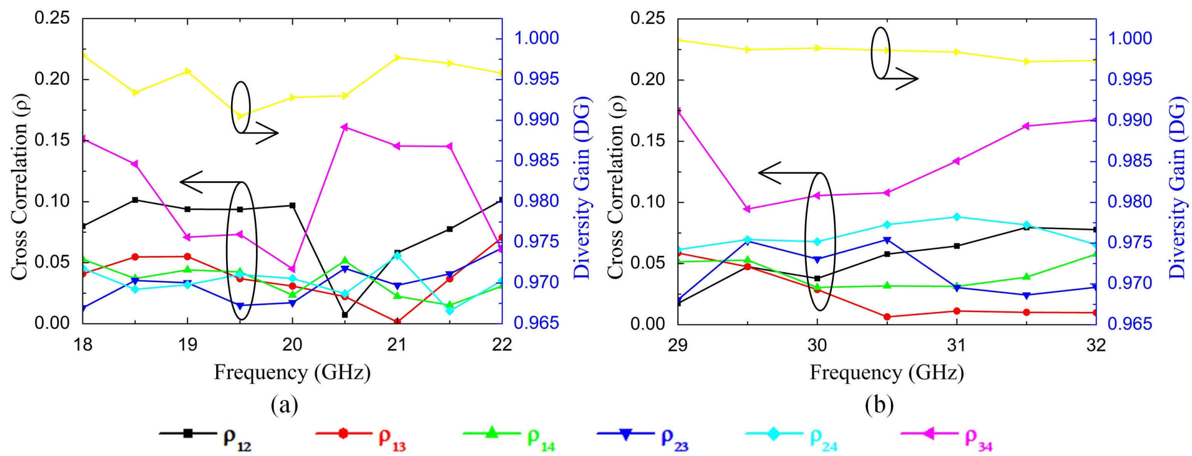

Figure 5.6: Cross correlation and diversity gain of dual-band four-port CP MIMO antenna at (a) lower frequency band and (b) upper frequency band.

The DG of the CP MIMO system is calculated from the correlation matrix R using (5.2) [181].

$$G = \frac{tr\left(R^2\right)}{\|R\|_{Fr}} \tag{5.2}$$

where tr is the matrix trace and $\|R\|_{Fr}$ is the Frobinus norm defined as $\|R\|_{Fr} := \sum_{m,n} |\rho_{mn}|^2$. The matrix trace corresponds to the sum of diagonal elements of the correlation matrix R. The DG in general for a MIMO antenna lies between 0 and 1 [181]. The variation of DG of the proposed CP MIMO with frequency is shown in Figure 5.6(a) and Figure 5.6(b) for lower and upper frequency bands, respectively. The simulated DG of the MIMO system is better than 0.97 at both the frequency bands.

The radiation pattern in the xy-plane and gain plot of the single element of the proposed four-port CP MIMO antenna is presented in Figure 5.7. The gain measured along the direction $\theta = 90°$ and $\phi = 90°$ for single element at lower and upper frequency bands

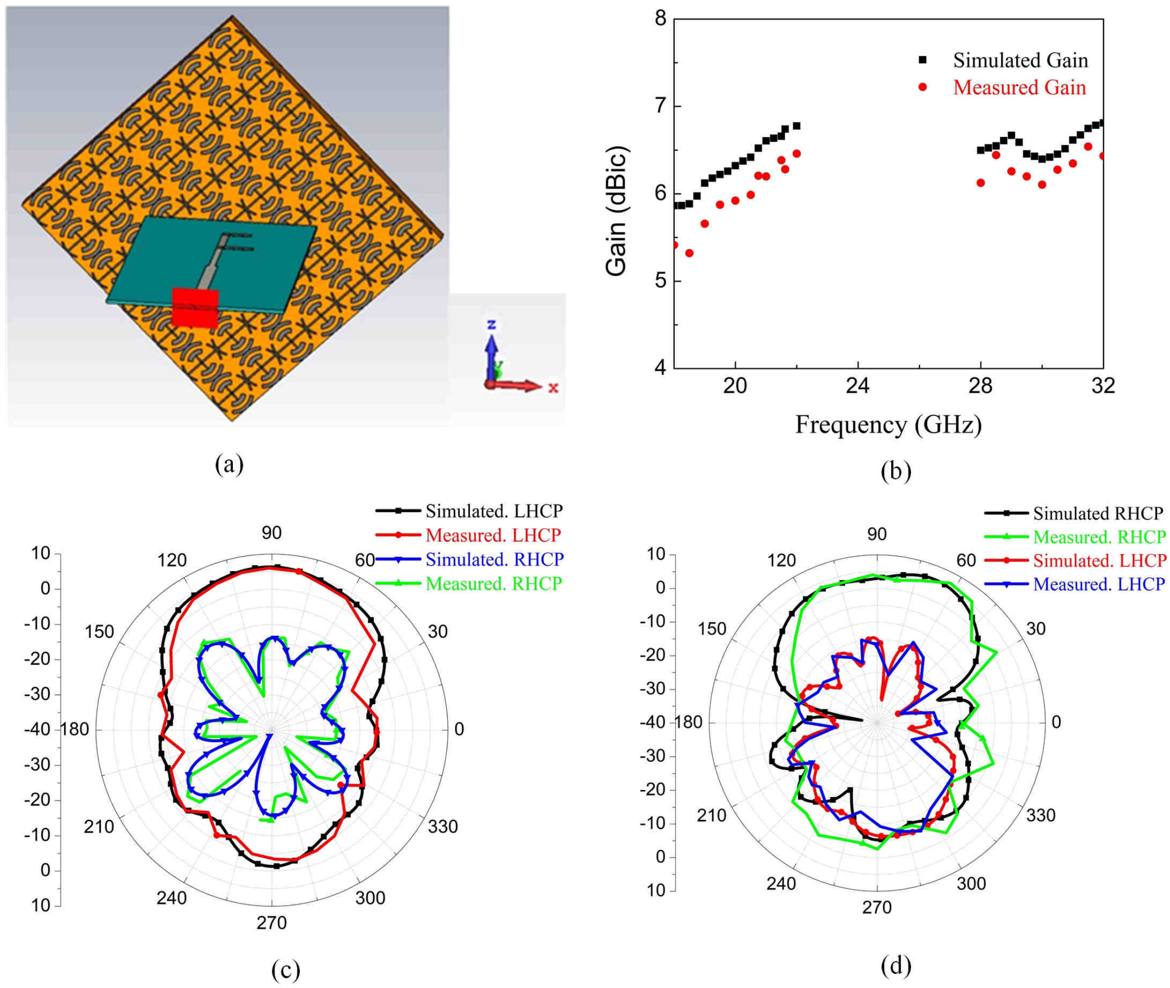

Figure 5.7: (a) Single element, (b) simulated and measured gain, radiation pattern in xy-plane at (c) 20 GHz and (d) 30 GHz of the single element of the proposed CP MIMO antenna.

is 5.92 dBic and 6.10 dBic, respectively as shown in Figure 5.7(b). It can be seen from Figure 5.7(c) and 5.7(d) that there is around 20 dB difference between RHCP and LHCP radiation pattern at both the operating frequencies depicting a good CP performance. Orthogonal CP is obtained due to $-90°$ and $+90°$ phase difference provided by the polarization converter between the orthogonal transmitted components at lower and upper frequency bands, respectively.

The simulated and measured far-field radiation pattern of the four-port CP MIMO antenna system in xz-plane by exciting port 1 and port 3 is shown in Figure 5.8(a) and (b), and Figure 5.8(c) and (d) at 20 and 30 GHz, respectively. A good agreement between simulated and measured results is obtained. It can be seen that CP nature can be

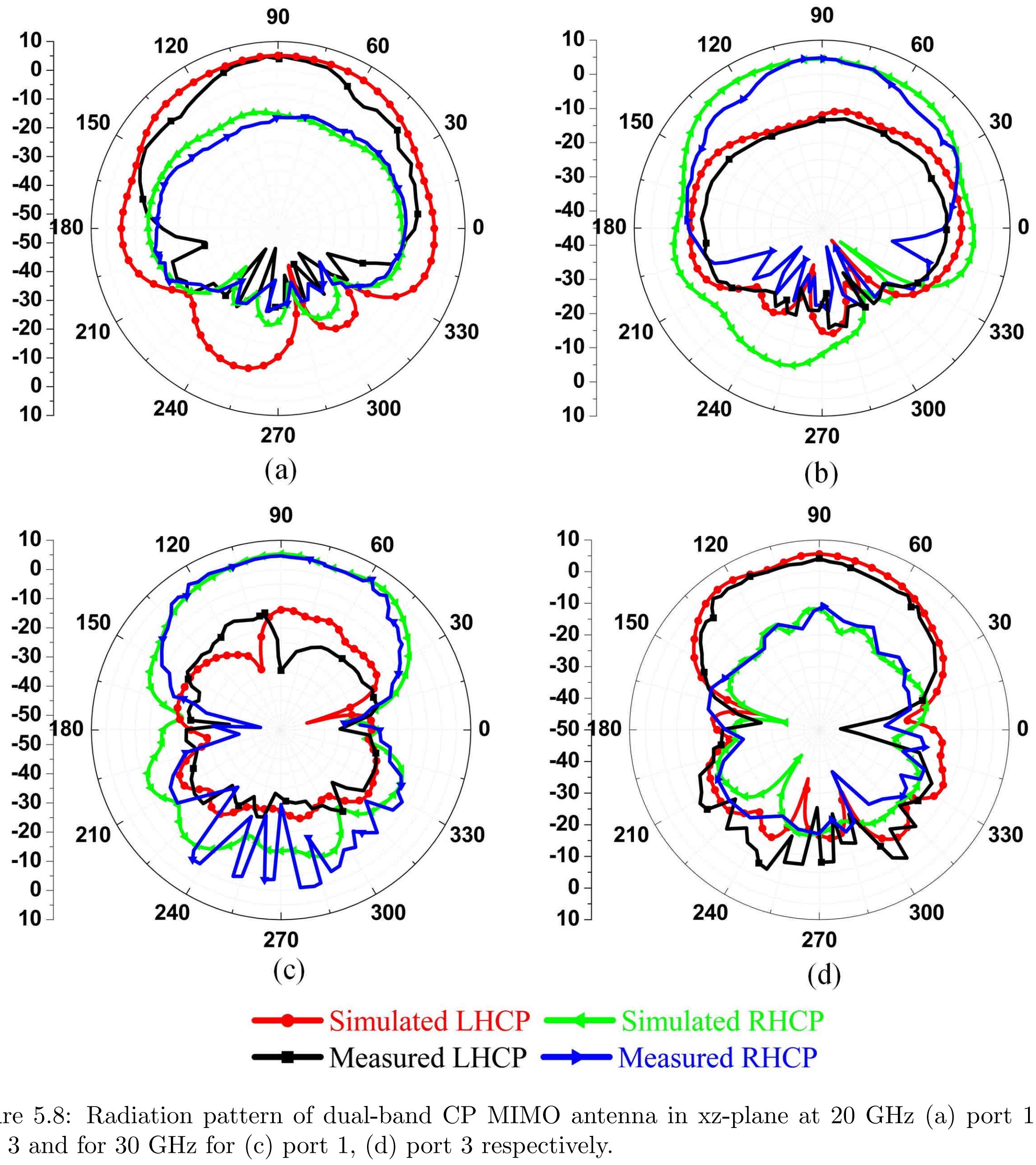

Figure 5.8: Radiation pattern of dual-band CP MIMO antenna in xz-plane at 20 GHz (a) port 1, (b) port 3 and for 30 GHz for (c) port 1, (d) port 3 respectively.

Table 5.1: Performance Comparison of the Proposed Dual-Band CP MIMO Antenna with the other MIMO Antennas available in Literature

Reference	Frequency (GHz)	CP Technique	Polarization	Size (λ_o^2)	CP Bandwidth (%)
[182]	6	Dual Port Feed Network	LHCP	0.8 × 1.3	19.9
[183]	3.7, 4.9	Unequal Feedline Mechanism	LHCP, LHCP	−−	5.4, 4.08
[184]	23.8, 27.93	Aperture Excitation	LHCP, Linear	0.456 × 0.456	2.1
[185]	27.3	Corner Truncation	−−	1× 1	16.8
[186]	2.33	Corner Truncation	LHCP	0.67 × 0.67	43.33
[187]	2.45	Inductor Loaded Metal Strip	LHCP	0.5 × 0.5	4.08
[188]	2.54, 3.52	Aperture Excitation	RHCP, RHCP	0.67 × 0.42	7.89, 7.09
[189]	3.57	−−	Linear	0.41 × 1.07	−−
[190]	2.9	−−	Linear	1.45 × 1.45	−−
[191]	25.64, 38.56	−−	Linear	2.05 × 1.70	−−
[192]	3.15	−−	Linear	0.52 × 1.05	−−
[193]	30	Aperture Excitation	LHCP	2.7 × 2.7	6
[194]	2.375	Using Four Microstrip Arcs	RHCP	0.55 × 0.55	7.71
[195]	28	Corner Truncation	RHCP	1.58 × 1.58	17
This Work	19.51, 28.67	Linear to Circular Polarization Converter	LHCP, RHCP	1.55 × 2.92	11.51, 3.69

reversed at lower and upper frequency bands by exciting the orthogonal ports. A similar radiation pattern at port 2 and port 4 for both the frequency bands is obtained owing to the symmetry of the MIMO elements. The performance comparison of the proposed

CP MIMO antenna with other CP MIMO antennas [182] $-$ [195] is presented in Table 5.1. The proposed CP MIMO antenna is dual-band, with orthogonal circular polarization at lower and upper frequency bands. Furthermore, due to geometry of the proposed CP MIMO antenna, polarization and spatial diversity is also achieved.

5.3 Conclusion

A four-port, CP dual-band MIMO antenna using two back to back F-shaped dipole structures integrated with 7×7 array of unit cells of dual-band LTC polarization converter is presented. The MIMO antenna achieves orthogonal circular polarization at lower frequency band (19.65 $-$ 22.05 GHz) and upper frequency band (29.25 $-$ 30.35) by using a LTC polarization converter. A prototype of the proposed CP MIMO antenna is fabricated and measured. The MIMO antenna exhibits a measured CP overlapping bandwidths of 3.74% and 3.69%, respectively in the lower frequency band (18.62 $-$ 20.40 GHz) and upper frequency band (29.25 $-$ 30.35 GHz) which is greater than the bandwidth required for the *Ka*-band fixed satellite services uplink and downlink frequency. The proposed system shows excellent MIMO properties in terms of isolation better than -19 dB, CC less than 0.19, and DG better than 0.97 at both the bands. A measured gain of 5.75 dBic and 4.77 dBic is achieved at 20 and 30 GHz, respectively for the proposed CP MIMO antenna. The proposed MIMO antenna can find applications on the move vehicle satellite communications.

Chapter 6

Conclusion

In this thesis, FSS based structures performing polarization conversion of an LP incident wave to a CP wave in the transmission mode have been designed, characterized and fabricated. The use of arrays of unit-cells of these LTC polarization converters in LP patch antenna/arrays has also been validated to achieve and realize the design of CP antenna/arrays. Thus a simpler method to design CP antenna arrays which eliminates the feed complexity in conventional methods is demonstrated.

Initially, a single substrate layer LTC polarization converter is designed transmitting an LP and CP wave in state I and state II, respectively determined by the state of PIN diode fitted in the central arm of the unit cell of the polarization converter. The unit cell is composed of half-hexagon and its mirror replica printed on both sides of a 60 mil thick substrate (ε_r= 2.2, $tan\delta$ = 0.0009) with a slot of length 1 mm in its central arm. The slot length is later realized by a PIN diode (BAR63-02LE6327) from Infineon Technologies. The structure transmits an LP and CP wave in state I (Diode On) and state II (Diode OFF), respectively when excited by a LP incident wave. Therefore, linear and circular modes of operation can be controlled and hence achieving polarization reconfigurability. The PRC is compact with an electrical size of $0.046\lambda_o^3$ and PCR higher than 0.9. The performance characteristic of the polarization reconfigurable converter (PRC) is validated by integrating a 45° rotated 6 × 6 array of its unit cell as a superstate in the broadside direction of a LP patch antenna resonating at the same frequency as that of the converter. The superstate is placed at a height of $\lambda_o/3$ from the LP patch antenna. The polarization state of the LP patch antenna is changed from linear to circular in the OFF state of diodes of PRC. The linear polarization of the LP patch antenna remains unaffected in the ON state of diodes. The proposed linear to circular polarization converter can be used with an antenna/antenna array to feed a highly directive transmit array designed in the uplink (14 – 14.5 GHz) of the Ku band satellite communication band for very small aperture terminal (VSAT) from 14 to 14.5 GHz.

A single substrate layer LTC polarization converter designed to achieve a wide angular stability for both TE and TM polarization is discussed in this thesis. The unit cell of the proposed polarization converter consists of split rings and a horizontal metallic strip printed on both sides of 1.52 mm thick dielectric substrate (ε_r= 2.2, $tan\delta$ = 0.0009). A LP wave incident on this converter is transformed into a CP wave in the frequency band of 28.75 – 32.85 GHz. The AR below 3 dB remains quite stable for varying incident angle upto 60° and 45° under TE and TM polarization, respectively. The ellipticity (e) in the range of 0.94 – 0.98 is obtained in the frequency band of 29.50 – 32.65 GHz upto 45° of oblique incidence. The equivalent circuit model of the polarization converter is also developed. A prototype of the wide angular stable LTC polarization converter consisting of 71 × 71 cells is fabricated. The measured ARBW of 10.13% (29.50 – 32.65 GHz) is exhibited by the proposed polarization converter. A unique technique to design and realize CP antenna arrays using the proposed LTC polarization converter is demonstrated. A 15 × 15 array of the unit cells of the proposed LTC 45° clockwise rotated is placed at a distance of $\lambda_o/2$ in the broadside direction of 1 × 4 and 4 × 4 LP antenna arrays operating at the same frequency as that of the LTC polarization converter to transform an LP antenna array into a CP antenna array. The integrated 1 × 4 and 4 × 4 CP antenna arrays are fabricated and exhibit a measured gain of 14.1 dBic and 18.7 dBic, respectively. The CP antenna arrays achieve a radiation efficiency higher than 96%. Therefore, a simple technique to design CP antenna arrays with high efficiency and radiation efficiency is realized eliminating feed complexities with conventional methods of obtaining CP radiation. The proposed polarization converter and CP antenna arrays can be used for uplink Ka-band fixed-satellite service (29.5 – 30.0 GHz) and military satellite communication (30.0 – 31.0 GHz) applications.

Dual-band LTC polarization converter with orthogonal CP at the lower and upper frequency bands of operation is also reported in this thesis. The unit cell of the polarization converter is the extension of the work presented in chapter-3 where a single band operation around 30 GHz is achieved. To obtain a dual-band operation a metallic strip along the vertical direction is added which resonates at around 20 GHz. The unit cell of the converter has a size of 3.72×3.90×1.52 mm^3 (0.0072λ_o^3, λ_o is calculated with respect to 20.67 GHz). The converter transmits a right hand circularly polarized (RHCP) wave at lower band (20.1 − 21.75 GHz) where the magnitude of orthogonal transmitted components is equal and a phase difference of 78.2° − 107.45° between them is obtained. In the upper frequency band (29.12 − 31.4 GHz) two equal magnitude orthogonal components having a phase difference varying from −75.72° to −95.66° are transmitted when LP wave is incident on the converter, therefore a left hand circularly polarized (LHCP) wave is transmitted at this frequency band. A prototype of 21 × 21 cells of the dual-band LTC is fabricated and a 3-dB ARBW of 5.56% (20.10 − 21.25 GHz) in the lower and 3.97% (29.12 − 30.30 GHz) at the upper frequency band is achieved. Next, a dual-band LP dipole antenna resonating at the same frequency as that of the LTC polarization converter is designed and fabricated. An array of 7 × 7 cells of the dual-band LTC are placed at distance of $\lambda_o/4$ ((λ_o is calculated with respect to 19.51 GHz)) in the end fire direction of the dipole antenna to obtain a dual-band CP dipole antenna with orthogonal CP polarization at the lower and upper frequency bands of operation. The antenna integrated with the polarization converter exhibits measured CP bandwidths of 7.80% and 6.57% in lower frequency band: 20.10 − 21.75 GHz and upper frequency band: 29.4 − 31.4 GHz, respectively. The integrated antenna can act as a feed source of a high gain dual-band transmit-array for uplink (30.0 − 31.0 GHz) and downlink (20.2 − 21.2 GHz) of Ka-band military satellite communication.

Thereafter, the design of four-port dual-band CP MIMO antenna with orthogonal circular polarization at the lower and upper frequency bands of operation. The single element of MIMO is composed of F-shaped dipole formed by cascading two dipoles of different lengths to achieve dual-band operation. The planar half-dipoles are fed by striplines on top and bottom, constituting two back-to-back F-shaped dipoles separated by a dielectric layer with ε_r= 2.2 and $tan\delta$ = 0.0009. An array of 7 × 7 elements of the unit cell of dual-band LTC polarization converter is placed at a distance of $\lambda_o/4$ in the end fire direction of the antenna. Initially a two port CP MIMO antenna is designed which is later transformed into a four port antenna by placing another two port antenna orthogonal to the first so that all the four elements are at right angles to each other with common ground connection. The four port CP antenna shows good MIMO performance with correlation coefficient (CC) less than 0.19 and diversity gain (DG) better than 0.98 at both the frequency bands. The four-port MIMO also agrees with polarization and spatial diversity, and the CP nature at lower and upper frequency bands can be interchanged by exciting the orthogonal ports. A prototype of the MIMO antenna is fabricated and the measured ARBW of 11.51% and 3.69% is obtained in the lower (19.65 − 22.05 GHz) and upper (29.25 − 30.35 GHz) frequency bands, respectively. The measured isolation among all the ports is better than -19 dB and -23 dB in the lower and upper frequency bands, respectively. The measured gain of 5.75 dBic and 4.77 dBic is obtained at 20 and 30 GHz, respectively along the direction $\theta = 90°$ and $\phi = 90°$. The proposed antenna can be used for Ka-band: 29.5 − 30.0 and 19.7 − 20.2 GHz fixed satellite service as uplink and downlink frequencies, respectively. To the best of the author's knowledge, the presented work reports the first dual-band four-port CP MIMO antenna with the capability of orthogonal CP at two operating frequency bands, with polarization and spatial diversity.

Scope of Future Work

In this thesis, several designs of single substrate layer LTC polarization converters are presented. The application of these LTC polarization converters to realize CP antenna/arrays is also presented. Still there remain enough scope for carrying out further studies in the design of LTC polarization converters with enhanced performances. The following research works can be considered as future scope of the proposed work:

1. A polarization reconfigurable converter proposed in this thesis transforms an incident LP wave to LP or a CP wave with either LHCP or RHCP polarization. Therefore, the work can be extended to obtain LP and both LHCP or RHCP waves within a single structure.

2. The dual-band LTC polarization converter proposed in this thesis converts an incident LP wave into orthogonal CP at the lower and upper frequency bands of operation. Therefore, the work can be extended to design a dual-band LTC polarization converter with same sense of polarization at the two frequency bands of operation.

3. The conformal LTC polarization converters can be designed, which can be integrated

with monopole antennas to obtain omnidirectional CP antenna.

4. Further studies can be carried out with the use of dual-band LTC polarization converter to design massive MIMO antennas with orthogonal circular polarization at the lower and upper frequency bands of operation.

5. Further studies can be carried out to design transmitarray/reflectrarray where the CP antenna/array realized by using the LTC polarization converters proposed in chapter-2 to chapter-4 can act as a feed source in the operating in the frequency band of the LTC polarization converter which can act as a useful ground station antenna for the K/Ka-band satellite communication.

Appendix A

Data Sheet PIN Diode BAR63-02LE6327

BAR63...

Silicon PIN Diodes

- PIN diode for high speed
  switching of RF signals
- Very low forward resistance (low insertion loss)
- Very low capacitance (high isolation)
- For frequencies up to 3GHz
- Pb-free (RoHS compliant) package
- Qualified according AEC Q101[1)]

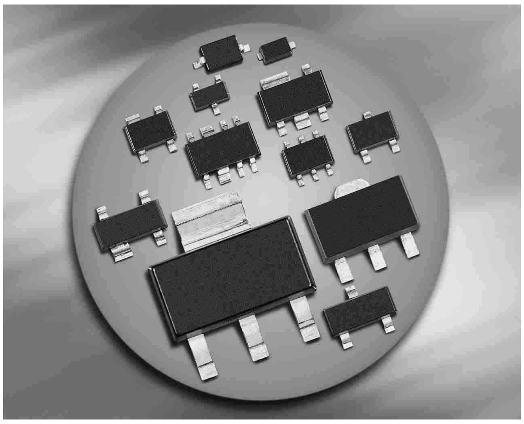

BAR63-02..	**BAR63-04**	**BAR63-05**	**BAR63-06**
BAR63-03W	**BAR63-04W**	**BAR63-05W**	**BAR63-06W**

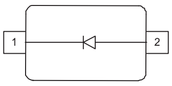

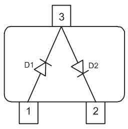

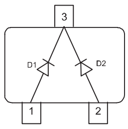

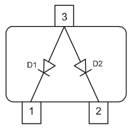

Type	Package	Configuration	L_S(nH)	Marking
BAR63-02L*	TSLP-2-1	single, leadless	0.4	G
BAR63-02V	SC79	single	0.6	G
BAR63-02W	SCD80	single	0.6	GG
BAR63-03W	SOD323	single	1.8	white G
BAR63-04	SOT23	series	1.8	G4s
BAR63-04W	SOT323	series	1.4	G4s
BAR63-05	SOT23	common cathode	1.8	G5s
BAR63-05W	SOT323	common cathode	1.4	G5s
BAR63-06	SOT23	common anode	1.8	G6s
BAR63-06W	SOT323	common anode	1.4	G6s

[1]*BAR63-02L is not qualified according AEC Q101

BAR63...

Maximum Ratings at T_A = 25°C, unless otherwise specified

Parameter	**Symbol**	**Value**	**Unit**
Diode reverse voltage	V_R	50	V
Forward current	I_F	100	mA
Total power dissipation BAR63-02L, $T_S \leq$ 118°C BAR63-02V, -02W, BAR63-03W, $T_S \leq$ 115°C BAR63-04...BAR63-06, $T_S \leq$ 55°C BAR63-04S, $T_S \leq$ 115°C BAR63-04W...BAR63-06W, $T_S \leq$ 105°C	P_{tot}	 250 250 250 250 250	mW
Junction temperature	T_j	150	°C
Operating temperature range	T_{op}	-55 ... 125	
Storage temperature	T_{stg}	-55 ... 150	

Thermal Resistance

Parameter	**Symbol**	**Value**	**Unit**
Junction - soldering point[1] BAR63-02L BAR63-02V, BAR63-02W BAR63-03W BAR63-04...BAR63-06 BAR63-04S BAR63-04W...BAR63-06W	R_{thJS}	 ≤ 125 ≤ 140 ≤ 155 ≤ 380 ≤ 180 ≤ 180	K/W

Electrical Characteristics at T_A = 25°C, unless otherwise specified

Parameter	**Symbol**	**Values**			**Unit**
		min.	**typ.**	**max.**	
DC Characteristics					
Breakdown voltage $I_{(BR)}$ = 5 µA	$V_{(BR)}$	50	-	-	V
Reverse current V_R = 35 V	I_R	-	-	10	nA
Forward voltage I_F = 100 mA	V_F	-	0.95	1.2	V

[1]For calculation of R_{thJA} please refer to the Technical Information

BAR63...

Electrical Characteristics at T_A = 25°C, unless otherwise specified

Parameter	Symbol	Values			Unit
		min.	typ.	max.	
AC Characteristics					
Diode capacitance	C_T				pF
V_R = 5 V, f = 1 MHz		-	0.21	0.3	
V_R = 0 V, 100 MHz ... 1.8 GHz		-	0.3	-	
Reverse parallel resistance	R_P				kΩ
V_R = 0 V, f = 100 MHz		-	500	-	
V_R = 0 V, f = 1 GHz		-	15	-	
V_R = 0 V, f = 1.8 GHz		-	5	-	
Forward resistance	r_f				Ω
I_F = 5 mA, f = 100 MHz		-	1.2	2	
I_F = 10 mA, f = 100 MHz		-	1	-	
Charge carrier life time I_F = 10 mA, I_R = 6 mA, measured at I_R = 3 mA, R_L = 100 Ω	τ_{rr}	-	75	-	ns
I-region width	W_I	-	4.5	-	µm
Insertion loss[1]	I_L				dB
I_F = 1 mA, f = 1.8 GHz		-	0.15	-	
I_F = 5 mA, f = 1.8 GHz		-	0.11	-	
I_F = 10 mA, f = 1.8 GHz		-	0.1	-	
Isolation[1]	I_{SO}				
V_R = 0 V, f = 0.9 GHz		-	17.9	-	
V_R = 0 V, f = 1.8 GHz		-	12.3	-	
V_R = 0 V, f = 2.45 GHz		-	10	-	
Series inductance	L_S	-	-	-	

[1]BAR63-02L in series configuration, Z = 50Ω

BAR63...

Diode capacitance $C_T = f\ (V_R)$

f = 1MHz - 1.8GHz

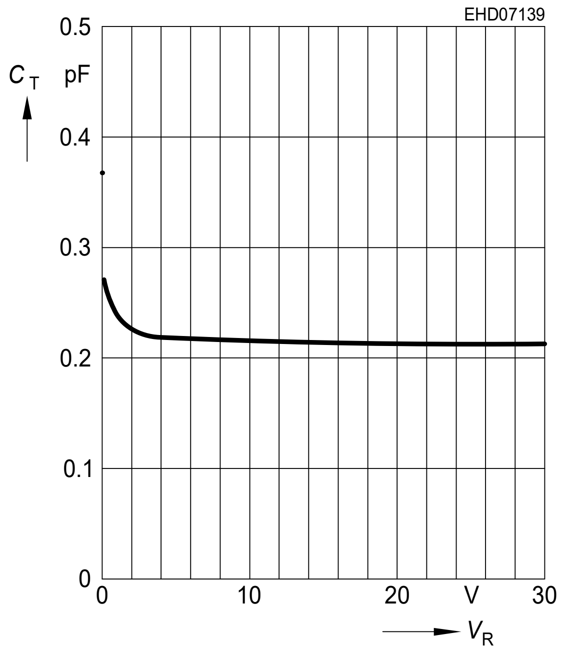

Reverse parallel resistance $R_P = f(V_R)$

f = Parameter

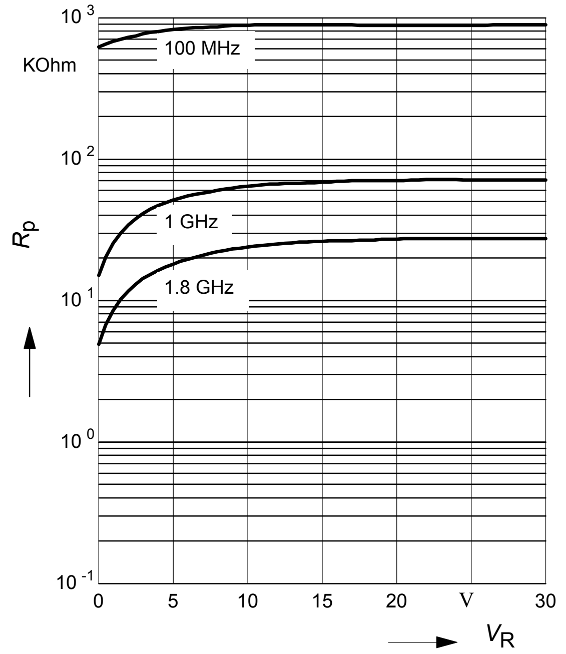

Forward resistance $r_f = f\ (I_F)$

f = 100MHz

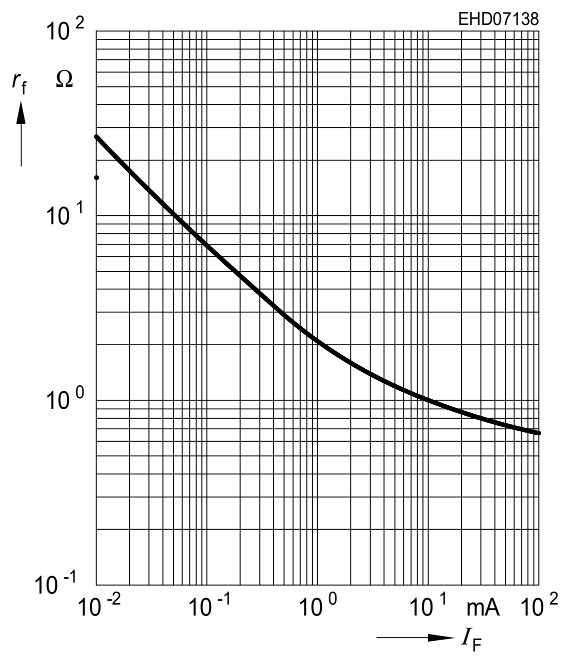

Forward current $I_F = f\ (V_F)$

T_A = Parameter

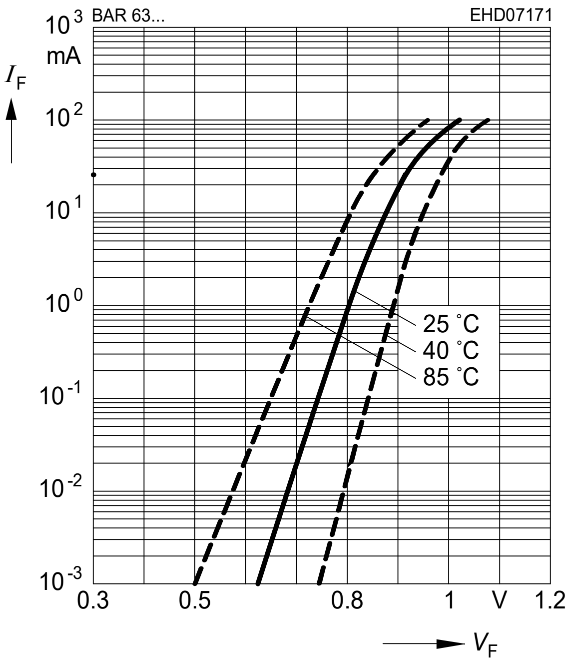

BAR63...

Forward current $I_F = f\,(T_S)$
BAR63-04...BAR63-06

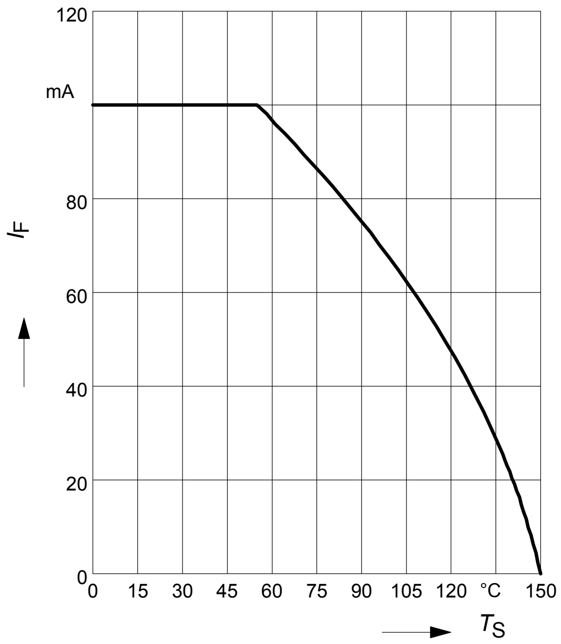

Forward current $I_F = f\,(T_S)$
BAR63-02V, BAR63-02W

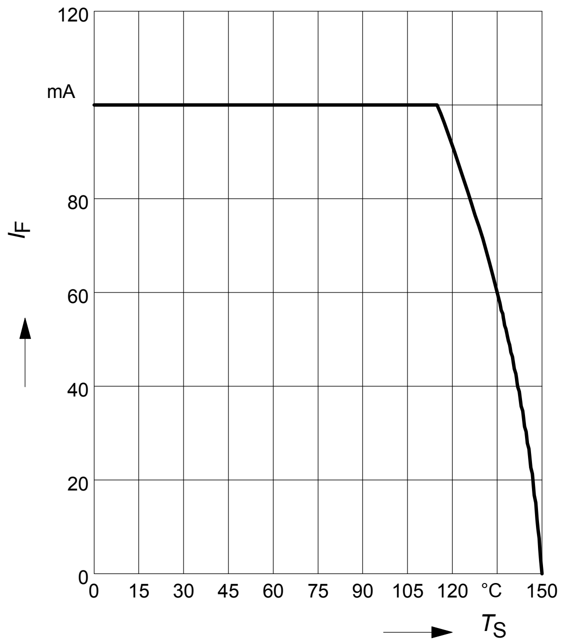

Forward current $I_F = f\,(T_S)$
BAR63-03W

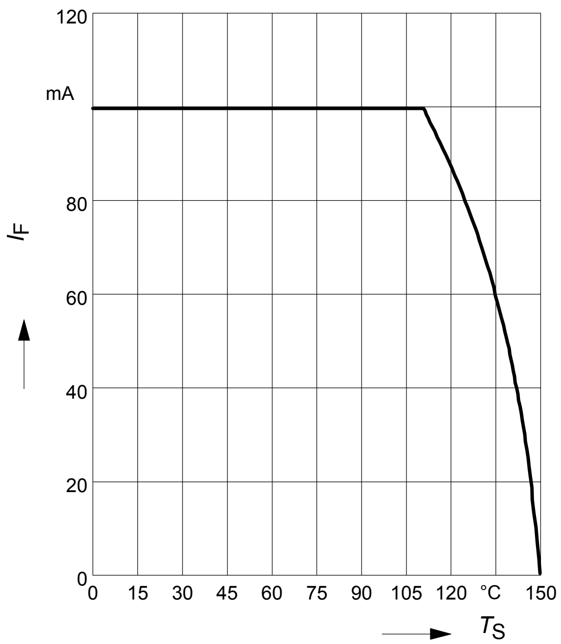

Forward current $I_F = f\,(T_S)$
BAR63-04W...BAR63-06W

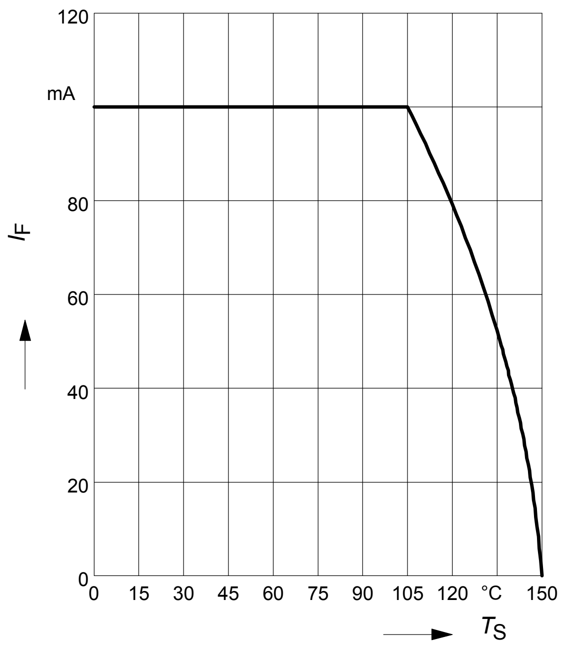

BAR63...

Permissible Puls Load $R_{thJS} = f(t_p)$

BAR63-04...BAR63-06

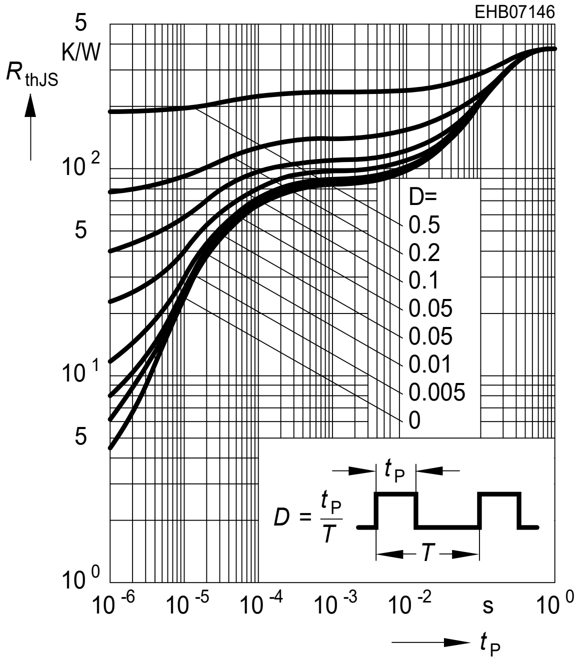

Permissible Pulse Load

$I_{Fmax}/ I_{FDC} = f(t_p)$

BAR63-04...BAR63-06

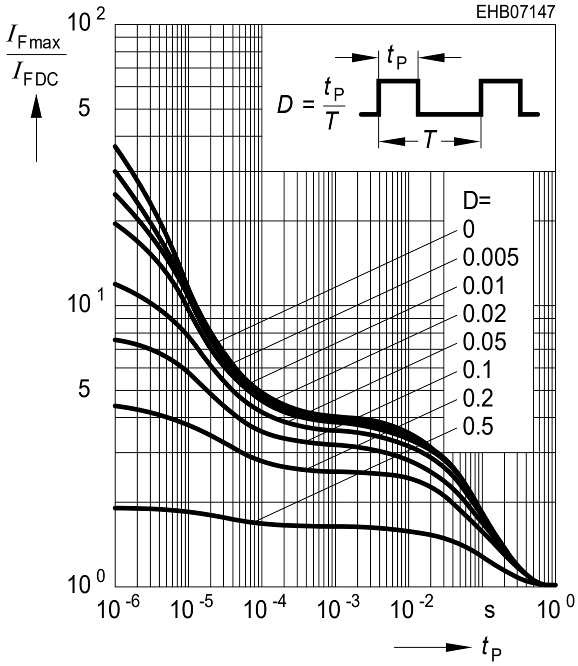

Permissible Puls Load $R_{thJS} = f(t_p)$

BAR63-02V, BAR63-02W

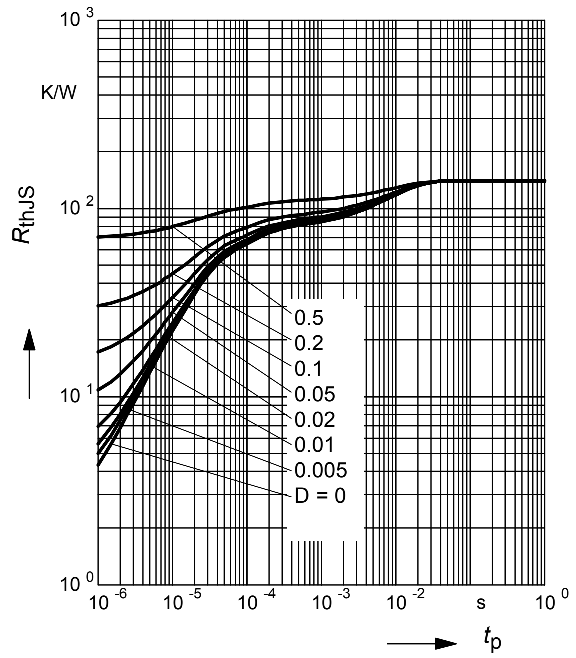

Permissible Pulse Load

$I_{Fmax}/ I_{FDC} = f(t_p)$

BAR63-02V, BAR63-02W

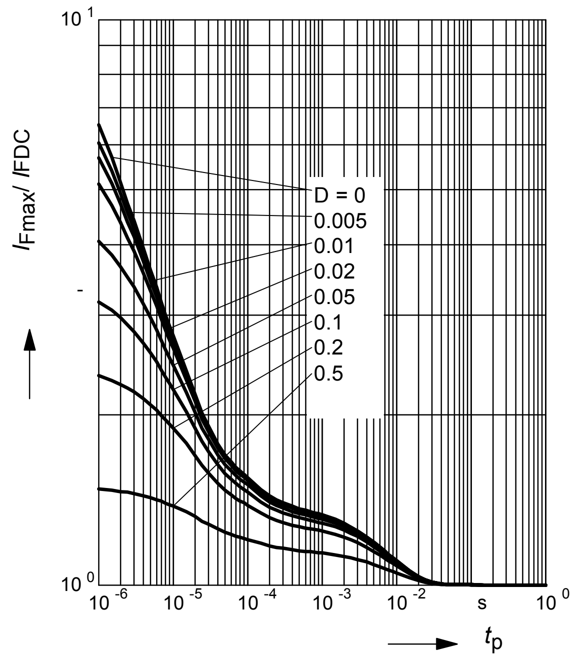

Permissible Puls Load $R_{thJS} = f\ (t_p)$

BAR63-03W

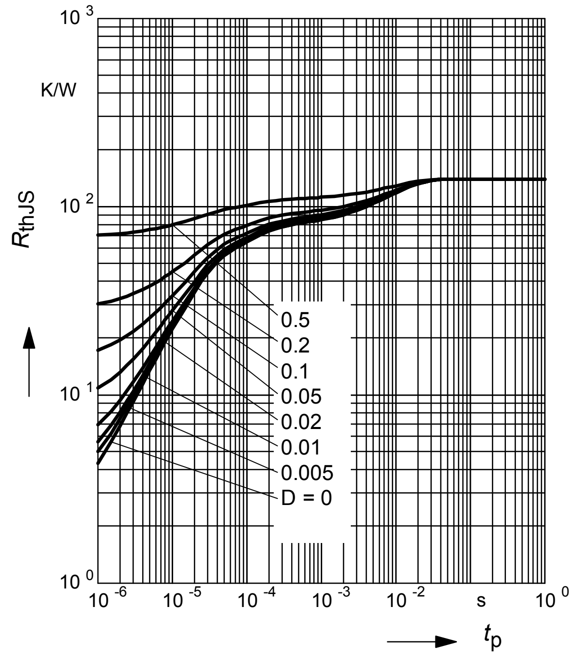

Permissible Pulse Load

$I_{Fmax}/\ I_{FDC} = f\ (t_p)$

BAR63-03W

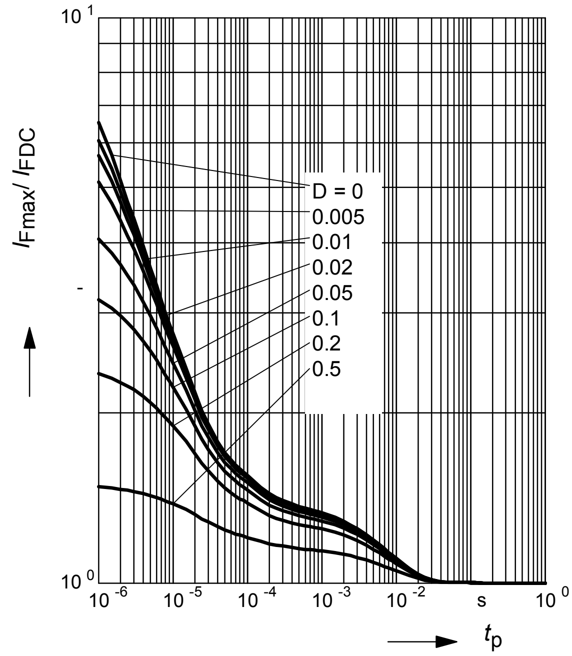

Permissible Puls Load $R_{thJS} = f\ (t_p)$

BAR63-04W...BAR63-06W

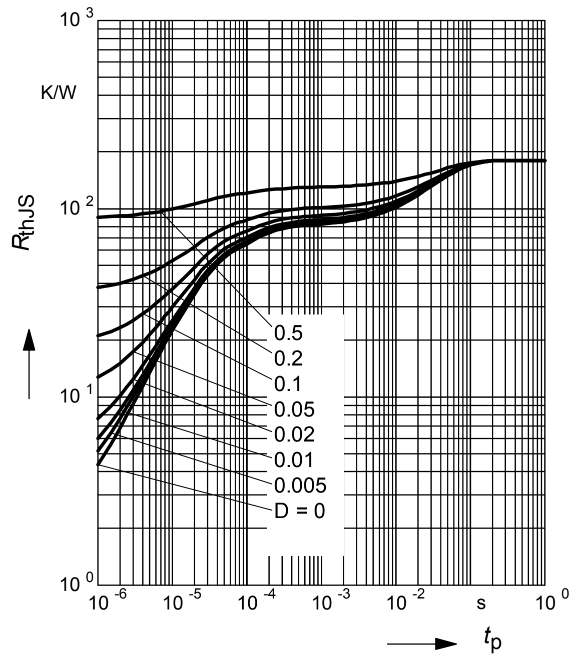

Permissible Pulse Load

$I_{Fmax}/\ I_{FDC} = f\ (t_p)$

BAR63-04W...BAR63-06W

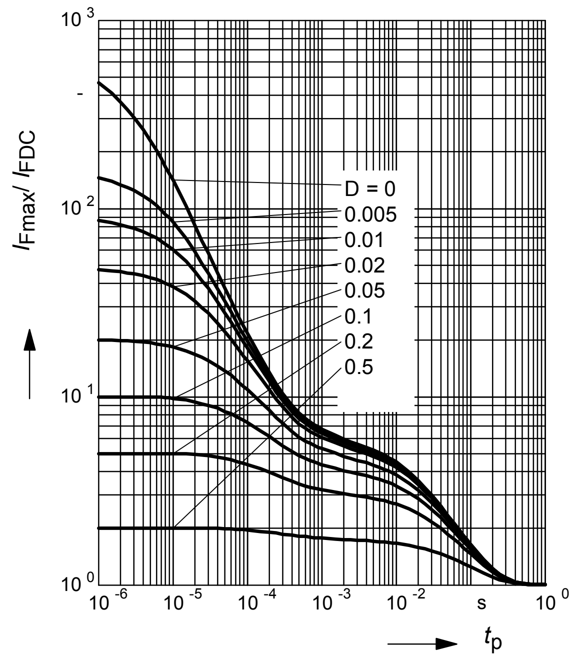

Insertion loss $I_L = -|S_{21}|^2 = f(f)$

I_F = Parameter

BAR63-02L in series configuration, $Z = 50\Omega$

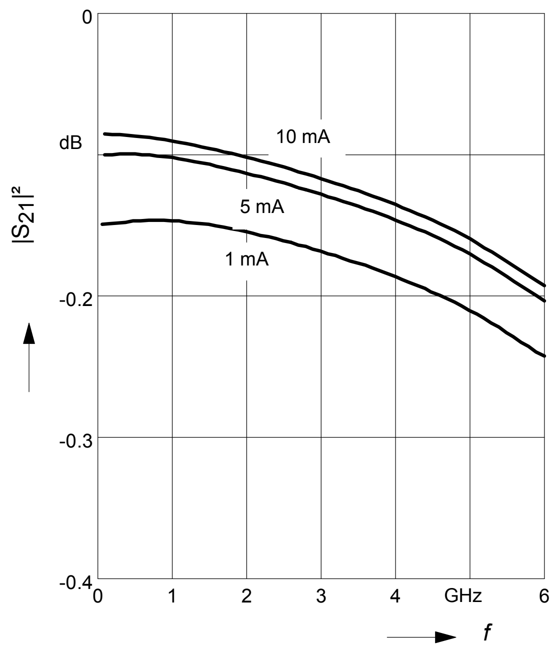

Isolation $I_{SO} = -|S_{21}|^2 = f(f)$

V_R = Paramter

BAR63-02L in series configuration, $Z = 50\Omega$

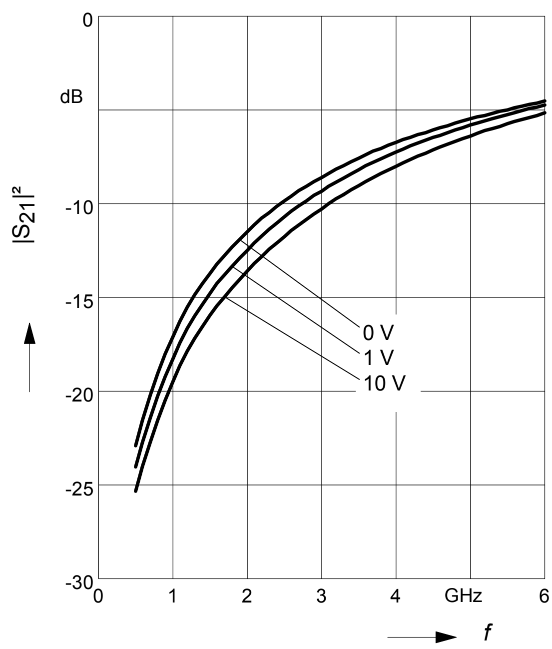

Bibliography

[1] C.A. Balanis, *Antenna Theory Analysis and Design.*, (4^{th} ed.) New York. John Wiley & Sons, pp. 70-75, 811-876, 2005.

[2] C. Dietlein, A. Luukanen, Z. Popovi, and E. Grossman, "A W-band polarization converter and isolator," *IEEE Trans. Antennas Propag.*, vol. 55, no. 6, pp. 1804–1809, Jun. 2007.

[3] Gerald, A. Burch, J.M, *Introduction to Matrix Methods in Optics* (1st ed.). John Wiley & Sons, 1975. ISBN 0471296856.

[4] P. Naseri, S. A. Matos, J. R. Costa, C. A. Fernandes and N. J. G. Fonseca, "Dual-Band Dual-Linear-to-Circular Polarization Converter in Transmission Mode Application to K/Ka -Band Satellite Communications," *IEEE Trans. Antennas Propag.*, vol. 66, no. 12, pp. 7128-7137, Dec. 2018, doi: 10.1109/TAP.2018.2874680.

[5] https://www.microwaves101.com/encyclopedias/polarization.

[6] B.D. Guenther. Guenther, "Polarization /Matrix Analysis," *Encyclopedia of Modern Optics.*, pp. 205-210, Elsevier, 2005, https://doi.org/10.1016/B0-12-369395-0/00692-8.

[7] David S. Kliger, James W. Lewis, Cora Einterz Randall, " Introduction to the Jones Calculus, Mueller Calculus, and Poincaré Sphere," *Polarized Light in Optics and Spectroscopy.*, Pp. 59-101, 1990, https://doi.org/10.1016/B978-0-08-057104-1.50007-(https://www.sciencedirect.com/science/article/pii/B9780080571041500077).

[8] D. Petr & F. Pavel, "Optical Fiber Birefringence Effects, Sources, Utilization and Methods of Suppression," *Recent Progress in Optical Fiber Research.*, Intechopen, 2012. 10.5772/27517.

[9] A. Kumar, A. Ghatak, "Birefringence in Optical Fibers: Applications," *Polarization of Light with Applications in Optical Fibers.*, 2011, Publisher SPIE Digital Library, https://doi.org/10.1117/3.861761.ch9.

[10] L. Htein, D. S. Gunawardena, W. -H. Chung, H. -Y. Au and H. -Y. Tam, "Accelerometer employing a side-hole fiber in a Sagnac interferometer," *Journal of Lightwave Technology.*, vol. 39, no. 10, pp. 3303-3311, 15 May15, 2021, doi: 10.1109/JLT.2021.3056474.

[11] L. J. Aplet and J. W. Carson, "A Faraday Effect Optical Isolator," *Appl. Opt..*, vol.3, no. 4, pp. 544-545, 1964.

[12] E Prati, "Propagation in gyroelectromagnetic guiding systems," *J. of Electr. Wav. and Appl..*, vol.17, no. 8, pp. 1177–1196, 2003.

[13] J. K. Gansel, M. Thiel, M. S. Rill, M. Decker, K. Bade, V. Saile, G. von Freymann, S. Linden, and M. Wegener, "Gold helix photonic metamaterial as broadband circular polarizer," *Science.*, vol. 325, no. 5947, pp. 1513–1515 sep. 2009.

[14] Pendry, J.B., Holden, A.J., Robbins, D.J. and Stewart, W.J, " Magnetism from conductors and enhanced nonlinear phenomena," *IEEE Trans. Microw. Theory. Techn.*, vol. 47 no. 11, pp.2075-2084, 1999.

[15] R.A. Shelby , D.R. Smith , S. Schultz, " Experimental verification of a negative index of refraction," *Science.*, vol. 6, pp. 77-91, 2001. doi: 10.1126/science.1058847. PMID: 11292865.

[16] N. Meinzer, W. L. Barnes and I. R. Hooper, " Plasmonic meta-atoms and metasurfaces," *Nature Photonics.*, vol. 8, no. 12, pp.889-898, 2014.

[17] A. V. Kildishev, A. Boltasseva, and V. M. Shalaev, " Planar photonics with metasurfaces," *Science.*, vol. 339 , Mar. 2013, doi: 10.1126/science.1232009.

[18] H. T. Chen, A. J. Taylor, and N. Yu, " A review of metasurfaces: physics and applications," *Reports on Progress in Physics.*, vol. 79, no. 7, 2016.

[19] C. Jansen, I. A. Al-Naib, N. Born, and M. Koch, " Terahertz metasurfaces with high Q- factors," *Applied Physics Letters.*, vol. 98, no. 5, 2011.

[20] M. Decker, I. Staude, M. Falkner, J. Dominguez, D. N. Neshev, I. Brener, T. Pertsch, and Y. S. Kivshar, "High-efficiency dielectric Huygens surfaces," *Advanced Optical Materials.*, vol. 3, no. 6, pp.813-820, 2015.

[21] B. A. Munk, *Frequency selective surfaces: theory and design*; John Wiley & Sons, 2005.

[22] J. J. S. Fernandez, "Frequency Selective Surface for Terahertz Applications," *Ph.D. Thesis*; The University of Edinburgh, United Kingdom, 2012.

[23] D. Lerner, "A wave polarization converter for circular polarization," *IEEE Trans. Antennas Propag.*, vol. 13, no. 1, pp. 3–7, 1965.

[24] $calvin.phys.columbia.edu/group_web/filter_development/download/filter.pdf$

[25] D. R. Smith, S. Schultz, P. Markos, and C. M. Soukoulis, "Determination of effective permittivity and permeability of metamaterials from reflection and transmission coefficients," *Physical Review B.*, vol. 65, no. 19, 2002. doi: 10.1103/PhysRevB.65.195104.

[26] N. Behdad, "A second order band pass frequency selective surface using non-resonant subwavelength periodic structures," *Microw. and Opt. Technol. Lett.*, vol. 50, no. 6, pp. 1639–1643, 2008.

[27] M. A. Al-Joumayly and N. Behdad, "A generalized method for synthesizing lowprofile, band-pass frequency selective surfaces with non-resonant constituting elements," *IEEE Trans. Antennas Propag.*, vol. 58, no. 12, pp. 4033– 4041, 2010.

[28] S. Zheng, Y. Yin, J. Fan, X. Yang, B. Li and W. Liu, "Analysis of Miniature Frequency Selective Surfaces Based on Fractal Antenna–Filter–Antenna Arrays," *IEEE Antennas Wireless Propag. Lett.*, vol. 11, pp. 240-243, 2012, doi: 10.1109/LAWP.2012.2189749.

[29] A. K. Rashid, B. Li and Z. Shen, "An overview of three-dimensional frequency-selective structures," *IEEE Antennas Propag. Mag.*, vol. 56, no. 3, pp. 43-67, June 2014, doi: 10.1109/MAP.2014.6867682.

[30] A. Chatterjee and S. K. Parui, "Performance Enhancement of a Dual-Band Monopole Antenna by Using a Frequency-Selective Surface-Based Corner Reflector," *IEEE Trans. Antennas Propag.*, vol. 64, no. 6, pp. 2165-2171, June 2016, doi: 10.1109/TAP.2016.2552543.

[31] Y. Pang, Y. Li, J. Zhang, Z. Xu and S. Qu, "Design of Frequency Selective Surface Based on Spoof Surface Plasmon Polariton Modes," *IEEE Antennas Wireless Propag. Lett.*, vol. 17, no. 6, pp. 1123-1126, June 2018, doi: 10.1109/LAWP.2018.2836346.

[32] X. -C. Zhu, P. -P. Zhang, Y. -X. Zhang, J. -X. Ge and Z. -H. Gao, "A High-Gain Filtering Antenna Based on Folded Reflectarray Antenna and Polarization-Sensitive Frequency Selective Surface," *IEEE Antennas Wireless Propag. Lett.*, vol. 19, no. 8, pp. 1462-1465, Aug. 2020, doi: 10.1109/LAWP.2020.3007540.

[33] J. Arnaud and F. Pelow,"Resonant-grid quasi-optical diplexers," *Bell Syst. Tech. J.*, vol. 54, pp. 263–283, 1975.

[34] S. W. Lee, ,"Scattering by dielectric-loaded screen," *IEEE Trans. Antennas Propag.*, vol. 19, pp. 656–665, 1971.

[35] E. Pelton and B. Munk,"A streamlined metallic radome," *IEEE Trans. Antennas Propag.*, vol. 22, no. 6, pp. 799-803, November 1974, doi: 10.1109/TAP.1974.1140896.

[36] S. Agahi, R. Mittra,"Design of a cascaded frequency selective surface as a dichroic subreflector," *In Proceedings of the Antennas and Propagation Society International Symposium: AP-S Merging Technologies for the 90' (Digest).*, Dallas, TX, USA, 7–11, pp. 88–91, May 1990.

[37] F. Costa, S. Genovesi, A. Monorchio, G. Manara,"A robust differential-amplitude codification for chipless RFID," *IEEE Microw. Wireless Compon. Lett*; vol. 25, pp. 832–834, 2015.

[38] D. Pozar, "Flat lens antenna concept using aperture coupled microstrip patches," *Electron. Lett.*, vol. 32, pp. 2109–2111, 1996.

[39] B. Zhang, C. Jin and Z. Shen, "Absorptive Frequency-Selective Reflector Based on Bent Metallic Strip Embedded With Chip-Resistor," *IEEE Trans. Antennas Propag.*, vol. 68, no. 7, pp. 5736-5741, July 2020, doi: 10.1109/TAP.2020.2971498.

[40] X. Xiu, W. Che, Y. Han and W. Yang, "Low-Profile Dual-Polarization Frequency-Selective Rasorbers Based on Simple-Structure Lossy Cross-Frame Elements," *IEEE Antennas Wireless Propag. Lett.*, vol. 17, no. 6, pp. 1002-1005, June 2018, doi: 10.1109/LAWP.2018.2829022.

[41] Z. Wang et al., "A High-Transmittance Frequency-Selective Rasorber Based on Dipole Arrays *IEEE Access.*, vol. 6, pp. 31367-31374, 2018, doi: 10.1109/ACCESS.2018.2843795.

[42] Q. Chen, D. Sang, M. Guo and Y. Fu, "Frequency-Selective Rasorber With Interabsorption Band Transparent Window and Interdigital Resonator," *IEEE Trans. Antennas Propag.*, vol. 66, no. 8, pp. 4105-4114, Aug. 2018, doi: 10.1109/TAP.2018.2835671.

[43] P. Yuste, J. M. Rius, J. Romeu, S. Blanch, A. Heldring and E. Ubeda, "A Microwave Invisibility Cloak: The Design, Simulation, and Measurement of a Simple and Effective Frequency-Selective Surface-Based Mantle Cloak," *IEEE Antennas Propag. Mag.*, vol. 60, no. 4, pp. 49-59, Aug. 2018, doi: 10.1109/MAP.2018.2839903.

[44] W. Tang, Y. Hao and R. Mittra, "Design of a Carpet Cloak to Conceal an Antenna Located Underneath," *IEEE Trans. Antennas Propag.*, vol. 60, no. 9, pp. 4444-4449, Sept. 2012, doi: 10.1109/TAP.2012.2207058

[45] M. Mahmoodi, L. VanZant and K. M. Donnell, "An Aperture Efficiency Approach for Optimization of FSS-Based Sensor Resolution," *IEEE Trans. Inst. Meas.*, vol. 69, no. 10, pp. 7837-7845, Oct. 2020, doi: 10.1109/TIM.2020.2986108.

[46] M. Mahmoodi and K. M. Donnell,“Performance Metrics for Frequency Selective Surface-Based Sensors,” *IEEE Sensors Lett.*, vol. 1, no. 6, pp. 1-4, Dec. 2017, Art no. 3501304, doi: 10.1109/LSENS.2017.2774830.

[47] S. Milici, J. Lorenzo, A. Lázaro, R. Villarino and D. Girbau,“Wireless Breathing Sensor Based on Wearable Modulated Frequency Selective Surface,” *IEEE Sensors Journal.*, vol. 17, no. 5, pp. 1285-1292, March, 2017, doi: 10.1109/JSEN.2016.2645766.

[48] M. Saikia, S. Ghosh and K. V. Srivastava,“Design and Analysis of Ultrathin Polarization Rotating Frequency Selective Surface Using V-Shaped Slots,” *IEEE Antennas Wireless Propag. Lett.*, vol. 16, pp. 2022-2025, 2017, doi: 10.1109/LAWP.2017.2693685.

[49] L. Li, Y. Li, Z. Wu, F. Huo, Y. Zhang and C. Zhao,“Novel Polarization-Reconfigurable Converter Based on Multilayer Frequency-Selective Surfaces,” *Proc. IEEE.*, vol. 103, no. 7, pp. 1057-1070, July 2015, doi: 10.1109/JPROC.2015.2437611.

[50] M. Fartookzadeh and S. H. Mohseni Armaki,“Dual-Band Reflection-Type Circular Polarizers Based on Anisotropic Impedance Surfaces,” *IEEE Trans. Antennas Propag.*, vol. 64, no. 2, pp. 826-830, Feb. 2016, doi: 10.1109/TAP.2015.2511152.

[51] M. Euler, V. Fusco, R. Cahill and R. Dickie,“325 GHz Single Layer Sub-Millimeter Wave FSS Based Split Slot Ring Linear to Circular Polarization Convertor,” *IEEE Trans. Antennas Propag.*, vol. 58, no. 7, pp. 2457-2459, July 2010, doi: 10.1109/TAP.2010.2048874.

[52] M. Hosseini and S. V. Hum,“A Semianalytical Approach to Designing High-Transparency Low-Profile Circular Polarizers,” *IEEE Trans. Antennas Propag.*, vol. 66, no. 12, pp. 7138-7147, Dec. 2018, doi: 10.1109/TAP.2018.2870426.

[53] E. Arnieri, F. Greco and G. Amendola,“A Broadband, Wide-Angle Scanning, Linear-to-Circular Polarization Converter Based on Standard Jerusalem Cross

Frequency Selective Surfaces," *IEEE Trans. Antennas Propag.*, vol. 69, no. 1, pp. 578-583, Jan. 2021, doi: 10.1109/TAP.2020.3004981.

[54] D. Li, T. W.Li, E. P. Li, Y.J. Zhang,"A 2.5-D Angularly Stable Frequency Selective Surface Using Via-Based Structure for 5G EMI Shielding," *IEEE Trans. Electromagn. Compat.*, vol. 60, pp. 768–775, 2018.

[55] https://www.slideshare.net/altairhtcus/cj-reddy-radomes-altairatc-final

[56] A. Tennant, W. Hurley, T. Dias,"Experimental knitted, textile frequency selective surfaces," *Electron. Lett.*, vol. 48, pp. 1386–1388, 2012.

[57] C. N. Chiu, K. P. Chang,"A novel miniaturized-element frequency selective surface having a stable resonance," *IEEE Antennas Wireless Propag. Lett.*, vol. 8, pp. 1175–1177, 2009.

[58] Martinez-Lopez, L. Rodriguez-Cuevas, J. Martinez-Lopez, J.I. Martynyuk, A.E," A multilayer circular polarizer based on bisected split-ring frequency selective surfaces," *Electron. Lett.*, vol. 13, pp. 153–156, 2014.

[59] A. H. Abdelrahman, A. Z. Elsherbeni, F. Yang,"Transmission phase limit of multilayer frequency-selective surfaces for transmitarray designs," *IEEE Trans. Antennas Propag.*, vol. 62, no. 2, pp. 690-697, Feb. 2014, doi: 10.1109/TAP.2013.2289313.

[60] S. M. A. Momeni Hasan Abadi, M. Li and N. Behdad,"Harmonic-Suppressed Miniaturized-Element Frequency Selective Surfaces With Higher Order Bandpass Responses," *IEEE Trans. Antennas Propag.*, vol. 62, no. 5, pp. 2562-2571, May 2014, doi: 10.1109/TAP.2014.2303822.

[61] S. M. A. M. H. Abadi and N. Behdad,"Design of Wideband, FSS-Based MultiBeam Antennas Using the Effective Medium Approach," *IEEE Trans. Antennas Propag.*, vol. 62, no. 11, pp. 5557-5564, Nov. 2014, doi: 10.1109/TAP.2014.2355192.

[62] N. Xu, J. Gao, J. Zhao, X. Feng,"A novel wideband, low-profile and second-order miniaturized band-pass frequency selective surfaces," *AIP Adv.*, vol. 5, 2015.

[63] A. L. P. Campos, E. E. C. de Oliveira, P. H. da Fonseca Silva,"Design of miniaturized frequency selective surfaces using Minkowski island fractal," *J. Microw. Optoelectron. Electromagn. Appl.*, vol. 9, no. 19, pp. 43–49, 2010.

[64] Y. Shi, W. Tang, W.Zhuang, C.Wang,"Miniaturised frequency selective surface based on 2.5-dimensional closed loop," *Electron. Lett.*, vol. 50, pp. 1656–1658, 2014.

[65] Y. Yu, C. Chiu, Y. Chiou and T. Wu,"A Novel 2.5-Dimensional Ultraminiaturized-Element Frequency Selective Surface," *IEEE Trans. Antennas Propag.*, vol. 62, no. 7, pp. 3657-3663, July 2014, doi: 10.1109/TAP.2014.2321153.

[66] B. Li and Z. Shen,"Three-Dimensional Bandpass Frequency-Selective Structures With Multiple Transmission Zeros," *IEEE Trans. Microw. Tech.*, vol. 61, no. 10, pp. 3578-3589, Oct. 2013, doi: 10.1109/TMTT.2013.2279776.

[67] A. K. Rashid, B. Li and Z. Shen,"An overview of three-dimensional frequency-selective structures," *IEEE Antennas Propag. Mag*; vol. 56, no. 3, pp. 43-67, June 2014, doi: 10.1109/MAP.2014.6867682

[68] G. I. Kiani,K. L. Ford, K. P. Esselle, A. R. Weily, C. Panagamuwa, J. C. Batchelor,"Single-layer bandpass active frequency selective surface," *Microw. Opt. Technol. Lett.*, vol. 50, pp. 2149–2151, 2008.

[69] L. Li,Y. Li, Z. Wu, F. Huo, Y. Zhang, C. Zhao,"Novel polarization-reconfigurable converter based on multilayer frequency-selective surfaces," *Proc. IEEE.*, vol. 103, no. 7, pp. 1057-1070, July 2015, doi: 10.1109/JPROC.2015.2437611.

[70] B. Li and Z. Shen,"Bandpass Frequency Selective Structure With Wideband Spurious Rejection," *IEEE Antennas Wirel. Propag. Lett.*, vol. 13, pp. 145-148, 2014, doi: 10.1109/LAWP.2014.2299278.

[71] C. Huang, C. Ji, X. Wu, J. Song and X. Luo,"Combining FSS and EBG Surfaces for High-Efficiency Transmission and Low-Scattering Properties," *IEEE*

Trans. Antennas Propag., vol. 66, no. 3, pp. 1628-1632, March 2018, doi: 10.1109/TAP.2018.2790430.

[72] L. Sun, H. Cheng, Y. Zhou, J. Wang,"Broadband metamaterial absorber based on coupling resistive frequency selective surface," *Opt. Express.*, vol. 20, pp. 4675–4680, 2012.

[73] K. S.Kunz, R. J. Luebbers,"The Finite Difference Time Domain Method for Electromagnetics., CRC Press: Boca Raton, FL, USA, 1993.

[74] J. S. Bagby,D. P. Nyquist, B. C. Drachman,"Integral formulation for analysis of integrated dielectric waveguides," *IEEE Trans. Microw. Theory Techn.*, vol. 33, pp. 906–915, 1985.

[75] M. Koshiba, M. Suzuki," Application of the Boundary-Element Method to Waveguide Discontinuities (Short Paper)," *IEEE Trans. Microw. Theory Techn.*, vol.34, pp. 301–307, 1986.

[76] J. W. Mink,F. K. Schwering,"Special Issue on Numerial Methods," *IEEE Trans. Microw. Theory Tech.*, vol. 33, no. 10, 1985.

[77] R. Mittra, C. H. Chan, T. Cwik,"Techniques for analyzing frequency selective surfaces-a review," *Proc. IEEE.*, vol. 76, pp. 1593–1615, 1988.

[78] R. Orta, R. Tascone, R. Zich," A unified formulation for the analysis of general frequency selective surfaces," *Electromagnetics.*, vol. 5, pp. 307–329, 1985.

[79] T. Cwik, R. Mittra, K. Lang, and T. Wu,"Frequency selective screens," *IEEE Antennas Propag. Society Newsletter.*, vol. 29, no. 2, pp. 5-10, 1987.

[80] D. K. Ghodgaonkar, V. V. Varadan, and V. K. Varadan,"A free-space method for measurement of dielectric constants and loss tangents at microwave frequencies," *IEEE Trans. Inst. Meas.*, vol. 38, no. 3, pp. 789-793, 1989.

[81] R. C. Johnson, H. A. Ecker, and J. S. Hollis,"Determination of far-field antenna patterns from near-field measurements," *Proc. IEEE.*; vol. 61, no. 12, pp. 1668-1694, 1973.

[82] B. Toh, R. Cahill, and V. Fusco,“Understanding and measuring circular polarization,” *IEEE Trans. Education.*, vol. 46, no. 3, pp. 313–318, Aug. 2003.

[83] C. L. Holloway, E. F. Kuester, J. A. Gordon, J. O’Hara, J. Booth and D. R. Smith,“An Overview of the Theory and Application of Metasurfaces: The Two-Dimensional Equivalents of Metamaterials,” *IEEE Trans. Antennas Propag.*, vol. 54, no. 2, pp. 10-11, 2012.

[84] J. Hao, Y. Yuan, L. Ran, T. Jiang, J. A. Kong, C. T. Chan and L. Zhou,“Manipulating electromagnetic wave polarizations by anisotropic metamaterials,” *Physical review lett.*, vol. 99, no. 6, 2007.

[85] S. L. Wadsworth, and G. D. Boreman,“Broadband infrared meanderline reflective quarter-wave plate,” *Optics express.*; vol. 19, no. 11, pp.10604-10612, 2011.

[86] C. Pfeiffer, and A. Grbic,“ Cascaded metasurfaces for complete phase and polarization control,” *Applied Physics Lett.*, vol. 102, no. 23, 2013.

[87] Y. Wang, M. Pu, C. Hu, Z. Zhao, C. Wang, and X. Luo,“ Dynamic manipulation of polarization states using anisotropic meta-surface,” *Optics Communications.*, vol. 319, pp.14-16, 2014.

[88] S. Liu, T. J. Cui, Q. Xu, D. Bao, L. Du, X. Wan, W. X. Tang, C. Ouyang, X. Y. Zhou, H. Yuan, and H. F. Ma,“ Anisotropic coding metamaterials and their powerful manipulation of differently polarized terahertz waves,” *Light: Science & Applications.*, vol. 5, no. 5, 2016.

[89] F. Dincer, C. Sabah, M. Karaaslan,E. Unal, M. Bakir, and U. Erdiven,“Asymmetric transmission of linearly polarized waves and dynamically wave rotation using chiral metamaterial,” *Prog. Electromag. Research.*, vol. 140, pp.227-239. 2013.

[90] Z. Li, M. Mutlu, and E. Ozbay,“ Chiral metamaterials: from optical activity and negative refractive index to asymmetric transmission,” *Journal of Optics.*, vol. 15, no. 2, 2013.

[91] J. H. Shi, H. F. Ma, C. Y. Guan, Z. P. Wang, and T. J. Cui,"Broadband chirality and asymmetric transmission in ultrathin 90-twisted Babinet-inverted metasurfaces," *Physical Review B.*, vol. 89, no. 16, 2014.

[92] D. Zarifi, M. Soleimani and V. Nayyeri,"Dual- and Multiband Chiral Metamaterial Structures With Strong Optical Activity and Negative Refraction Index," *IEEE Antennas Wirel. Propag. Lett.*, vol. 11, pp. 334-337, 2012, doi: 10.1109/LAWP.2012.2191261.

[93] L. Wu, Z. Yang, Y. Cheng, Z. Lu, P. Zhang, M. Zhao, R. Gong, X. Yuan, Y. Zheng, and J. Duan, Electromagnetic manifestation of chirality in layer-by-layer chiral metamaterials," *Optics express.*, vol. 21, no. 5, pp.5239-5246, 2013.

[94] Y. Liu, K. Li, Y. Jia, Y. Hao, S. Gong and Y. Guo,"Wideband RCS Reduction of a Slot Array Antenna Using Polarization Conversion Metasurfaces," *IEEE Trans. Antennas Propag.*, vol. 64, no. 1, pp. 326-331, 2016.

[95] X. Gao, X. Han, W. Cao, H. O. Li, H. F. Ma and T. J. Cui,"Ultrawideband and High-Efficiency Linear Polarization Converter Based on Double V-Shaped Metasurface," *IEEE Trans. Antennas Propag.*, vol. 63, no. 8, pp. 3522-3530, Aug. 2015, doi: 10.1109/TAP.2015.2434392.

[96] L. Peng, X. Li, X. Jiang and S. Li,"A Novel THz Half-Wave Polarization Converter for Cross-Polarization Conversions of Both Linear and Circular Polarizations and Polarization Conversion Ratio Regulating by Graphene," *Journal of Lightwave Techn.*, vol. 36, no. 19, pp. 4250-4258, Oct.1, 2018, doi: 10.1109/JLT.2018.2836904.

[97] L. Zhang, P. Zhou, H. Lu, H. Chen, J. Xie and L. Deng,"Ultra-Thin Reflective Metamaterial Polarization Rotator Based on Multiple Plasmon Resonances," *IEEE Antennas Wireless Propag. Lett.*, vol. 14, pp. 1157-1160, 2015, doi: 10.1109/LAWP.2015.2393376.

[98] H. Chen, J. Wang, H. Ma, S. Qu, J. Zhang, Z. Xu and A. Zhang,"Broadband perfect polarization conversion metasurfaces," *Chinese Physics B.*, vol. 24, no. 1, pp. 1-5, 2015.

[99] H. Chen, J. Wang, H. Ma, S. Qu, Z. Xu, A. Zhang, M. Yan and Y. Li,"Ultra-wideband polarization conversion metasurfaces based on multiple plasmon resonances," *Journal of Appl. Physics.*, vol. 115, no. 154504, pp. 1-5, 2014.

[100] E. Doumanis, G. Goussetis, J. L. Gomez-Tornero, R. Cahill, and V. Fusco,"Anisotropic impedance surfaces for linear to circular polarization conversion," *IEEE Trans. Antennas Propag.*, vol. 60, no. 1, pp. 212–219, Jan. 2012.

[101] N. J. G. Fonseca, and C. Mangenot,"High-performance electrically thin dual-band polarizing reflective surface for broadband satellite applications," *IEEE Trans. Antennas Propag.*, vol. 64, no. 2, pp. 640- 649, 2015.

[102] W. Tang, S. Mercader-Pellicer, G. Goussetis, H. Legay and N. J. G. Fonseca,"Low-profile compact dual-band unit cell for polarizing surfaces operating in orthogonal polarizations," *IEEE Trans. Antennas Propag.*, vol. 65, no. 3, pp. 1472-1477, 2017.

[103] Q. Zheng, C. Guo, and J. Ding,"Wideband metasurface-based reflective polarization converter for linear-to-linear and linear-to-circular polarization conversion," *IEEE Antennas Wireless Propag. Lett.*, vol. 17, no. 8, pp. 1459–1463, Aug. 2018.

[104] Y. Jia et al.,"Ultra-wideband metasurface with linear- to circular polarization conversion of an electromagnetic wave," *Opt. Mater. Express.*, vol. 8, no. 3, pp. 597-604, 2018.

[105] X. Huang, H. Yang, D. Zhang, and Y. Luo,"Ultrathin dual-band metasurface polarization converter," *IEEE Trans. Antennas Propag.*, vol. 67, no. 7, pp. 4636–4641, Jul. 2019.

[106] D. Kundu, J. Singh, D. Singh and A. Chakrabarty,"Design and Analysis of Broadband Ultrathin Reflective Linear-to-Circular Polarization Converter Using Polygon-Based Anisotropic-Impedance Surface," *IEEE Trans. Antennas Propag.*, vol. 69, no. 8, pp. 5154-5159, Aug. 2021, doi: 10.1109/TAP.2021.3060130.

[107] H. Ma, G. Wang, G. Kong and T. Cui,“Broadband circular and linear polarization conversions realized by thin birefringent reflective metasurfaces,” *Opt. Mater. Express.*, vol. 4, no. 8, pp. 1717-1724, 2014.

[108] P. Xu, W. X. Jiang, S. Y. Wang and T. J. Cui,“An Ultrathin Cross-Polarization Converter With Near Unity Efficiency for Transmitted Waves,” *IEEE Trans. Antennas Propag.*, vol. 66, no. 8, pp. 4370-4373, Aug. 2018, doi: 10.1109/TAP.2018.2839972.

[109] Y. Ye and S. He,“90° polarization rotator using a bilayered chiral metamaterial with giant optical activity,” *Applied Physics Lett.*, vol. 96, no. 203501, pp. 1-3, 2010.

[110] J. Shi, H. Ma, C. Guan, Z. Wang and T. Cui,“Broadband chirality and asymmetric transmission in ultrathin 90°-twisted Babinet-inverted metasurfaces,” *Physical Review B.*, vol. 89, no. 165128, pp. 1-7, 2014.

[111] Z. Wei, Y. Cao, Y. Fan, X. Yu and H. Li,“Broadband polarization transformation via enhanced asymmetric transmission through arrays of twisted complementary split-ring resonators,” *Applied Physics Lett.*, vol. 99, no. 221907, pp. 1-3, 2011.

[112] L. Young, L. A. Robinson, and C. Hacking,“Meander-line polarizer,” *IEEE Trans. Antennas Propag.*, vol. 21, no. 3, pp. 376–378, May 1973.

[113] P. Fei, Z. Shen, X. Wen, and F. Nian,“A single-layer circular polarizer based on hybrid meander line and loop configuration,” IEEE Trans. Antennas Propag., vol. 63, no. 10, pp. 4609–4614, Oct. 2015.

[114] M. Joyal and J. Laurin, “Analysis and design of thin circular polarizers based on meander lines,” *IEEE Trans. Antennas Propag.*, vol. 60, no. 6, pp. 3007–3011, Jun. 2012.

[115] R. Chu and K. Lee,“Analytical model of a multilayered meander-line polarizer plate with normal and oblique plane-wave incidence,” *IEEE Trans. Antennas Propag.*, vol. 35, no. 6, pp. 652–661, Jun. 1987.

[116] G. L. Matthaei. L. Young, and E. M. T. Jones," *Microwave Filters, Impedance Matching Networks and Coupling Structures.*, New York: McGraw-Hill, 1964, ch. 9.

[117] I. Sohail, Y. Ranga, K. P. Esselle and S. G. Hay,"A linear to circular polarization converter based on Jerusalem-Cross frequency selective surface," *2013 7th European Conference on Antennas and Propagation (EuCAP).*, Gothenburg, Sweden, 2013, pp. 2141-2143.

[118] E. Arnieri, F. Greco and G. Amendola,"A Broadband, Wide-Angle Scanning, Linear-to-Circular Polarization Converter Based on Standard Jerusalem Cross Frequency Selective Surfaces," *IEEE Trans. Antennas Propag.*, vol. 69, no. 1, pp. 578-583, Jan. 2021, doi: 10.1109/TAP.2020.3004981.

[119] V. Xiaoliang , C. Huang, M. Pu , C. Hu , Q. Feng , X. Luo ,"Single-layer circular polarizer using metamaterial and its application in antenna," *Microw. Opt. Technol. Lett.*, vol. 54, no. 7, pp. 1770-1774. https://doi.org/10.1002/mop.26884.

[120] S. M. A. M. H. Abadi and N. Behdad,"Wideband linear-to-circular polarization converters based on miniaturized-element frequency selective surfaces," *IEEE Trans. Antennas Propag.*, vol. 64, no. 2, pp. 525–534, Feb. 2016.

[121] W. Zhang, J.-Y. Li, and J. Xie,"A broadband circular polarizer based on cross-shaped composite frequency selective surfaces," *IEEE Trans. Antennas Propag.*, vol. 65, no. 10, pp. 5623-5627, Oct. 2017.

[122] C. Pfeiffer and A. Grbic,"Millimeter-wave transmitarrays for wavefront and polarization control,"*IEEE Trans. Microw. Theory Techn.*, vol. 61, no. 12, pp. 4407–4417, Dec. 2013.

[123] M. Mutlu, A. E. Akosman, A. E. Serebryannikov, and E. Ozbay,"Asymmetric chiral metamaterial circular polarizer based on four U-shaped split ring resonators,"*Opt. Lett.*, vol. 36, no. 9, pp. 1653–1655, 2011.

[124] S.-Y. Wang, W. Liu, and W. Geyi, "Dual-band transmission polarization converter based on planar-dipole pair frequency selective surface," *Sci. Rep.*, vol. 8, no. 1, Dec. 2018, Art. no. 3791.

[125] Q. Zeng, W. Ren, H. Zhao, Z. Xue, and W. Li, "Dual-band transmission-type circular polariser based on frequency selective surfaces," *IET Microw. Antennas Propag.*, vol. 13, no. 2, pp. 216–222, Feb. 2019.

[126] P. Naseri, C. A. Fernandes, S. A. Matos, and J. R. Costa, "Antenna filter-antenna-based cell for linear-to-circular polarizer transmitarray," *Proc. IEEE Int. Symp. Antennas Propag., USNC/URSI Nat. Radio Sci. Meeting.*, San Diego, CA, USA, Jul. 2017, pp. 1071–1072.

[127] P. Naseri, S. A. Matos, J. R. Costa, C. A. Fernandes, and N. J. G. Fonseca, "Dual-band dual-linear-to-circular polarization converter in transmission mode application to K/K a-band satellite communications," *IEEE Trans. Antennas Propag.*, vol. 66, no. 12, pp. 7128–7137, Dec. 2018.

[128] A. Abbaspour-Tamijani, K. Sarabandi, and G. M. Rebeiz, "Antenna filter-antenna arrays as a class of bandpass frequency-selective surfaces," *IEEE Trans. Microw. Theory Techn.*, vol. 52, no. 8, pp. 1781–1789, Aug. 2004.

[129] M. Hosseini and S. V. Hum, "A systematic circuit-based approach to efficiently realize singleand dual-band circular polarizers," *Proc. 12th Eur. Conf. Antennas Propag. (EuCAP).*, London, U.K., 2018, pp. 1–5.

[130] Y. Youn and W. Hong, "Planar dual-band linear to circular polarization converter using radial-shape multi-layer FSS," *Proc. IEEE Int. Symp. Antennas Propag., USNC/URSI Nat. Radio Sci. Meeting.*, Boston, MA, USA, Jul. 2018, pp. 1465–1466.

[131] S. Khan and T. F. Eibert, "A dual-band metasheet for asymmetric microwave transmission with polarization conversion," *IEEE Access.*, vol. 7, pp. 98045–98052, 2019.

[132] H. Zhu, S. Cheung, K. Chung and T. Yuk,"Linear-to-circular polarization conversion using metasurface," *IEEE Trans. Antennas Propag.*, vol. 61, no. 9, pp. 4615-4623, 2013.

[133] Y. Li, J. Zhang, S. Qu, J. Wang, L. Zheng, Y. Pang, Z. Xu and A. Zhang,"Achieving wide-band linear-to-circular polarization conversion using ultra-thin bi-layered metasurfaces," *Journal of Applied Physics.*, vol. 117, no. 044501, pp. 1-7, 2015.

[134] B. Lin, J. Wu and X. Da,"Linear-to-circular polarization converter based on a secondorder band-pass frequency selective surface," *Applied Physics A.*, vol. 123, no. 43, pp. 1-5, 2017.

[135] L. Martinez-Lopez, J. Rodriguez-Cuevas, I. Martinez-Lopez and A. Martynyuk,"A Multilayer Circular Polarizer Based on Bisected Split-Ring Frequency Selective Surfaces," *IEEE Antennas Wireless Propag. Lett.*, vol. 13, pp. 153-156, January 2014.

[136] W. A. Imbriale, S. S. Gao, and L. Boccia," *Space Antenna Handbook.*, John Wiley & Sons, 2012.

[137] C. A. Leal-Sevillano, J. A. Ruiz-Cruz, J. R. Montejo-Garai, and J. M. Rebollar,"Novel dual-band single circular polarization antenna feeding network for satellite communications," *2014 8th European Conference on Antennas and Propagation (EuCAP 2014).*, April 2014, pp. 3265–3269.

[138] B. W. Parkinson," *Global positioning system: Theory and applications.*, vol. 1: AIAA, 1996.

[139] C. C. Counselman,"Multipath-rejecting GPS antennas," *Proc. IEEE.*, vol. 87, pp. 86-91, 1999.

[140] E. Brookner, W. M. Hall, and R. H. Westlake,"Faraday loss for L-band radar and communications systems," *IEEE Trans. Aerospace Elect. Sys.*, pp. 459-469, 1985.

[141] S. Gao, Q. Luo, and F. Zhu," *Circularly polarized antennas.*, John Wiley & Sons, 2013.

[142] W. A. Imbriale, S. Gao, and L. Boccia," *Space antenna handbook.*, John Wiley & Sons, 2012.

[143] G. C. Tavik, C. L. Hilterbrick, J. B. Evins, J. J. Alter, J. G. Crnkovich, J. W. de Graaf, W. Habicht, G. P. Hrin, S. A. Lessin, and D. C. Wu,"The advanced multifunction RF concept,"*IEEE Trans. Microw. Theory Techn.*, vol. 53, pp. 1009-1020, 2005.

[144] P. S. Hall, P. Gardner, and A. Faraone,"Antenna requirements for software defined and cognitive radios,"*Proc. IEEE.*, vol. 100, pp. 2262-2270, 2012.

[145] J. P. Doane, K. Sertel, and J. L. Volakis,"A wideband, wide scanning tightly coupled dipole array with integrated balun (TCDA-IB)," *IEEE Trans. Antennas Propag.*, vol. 61, pp. 4538-4548, 2013.

[146] Y. -X. Zhang, Y. -C. Jiao and L. Zhang,"Wideband Circularly Polarized Array Antennas With Sequential-Rotation Polarization Grid and Simplified Full-SIW Feeding Networks," *IEEE Trans. Antennas Propag.*, vol. 68, no. 8, pp. 6088-6097, Aug. 2020, doi: 10.1109/TAP.2020.2985065.

[147] Q. Wu, J. Hirokawa, J. Yin, C. Yu, H. Wang and W. Hong,"MillimeterWave Multibeam Endfire Dual-Circularly Polarized Antenna Array for 5G Wireless Applications," *IEEE Trans. Antennas Propag.*, vol. 66, no. 9, pp. 4930-4935, Sept. 2018, doi: 10.1109/TAP.2018.2851667.

[148] J. Wu, Y. J. Cheng and Y. Fan,"Millimeter-Wave Wideband High Efficiency Circularly Polarized Planar Array Antenna," *IEEE Trans. Antennas Propag.*, vol. 64, no. 2, pp. 535-542, Feb. 2016, doi: 10.1109/TAP.2015.2506726.

[149] C. Ma, Z. Ma and X. Zhang,"Millimeter-Wave Circularly Polarized Array Antenna Using Substrate-Integrated Gap Waveguide Sequentially Rotating Phase Feed," *IEEE Antennas Wireless Propag. Lett.*, vol. 18, no. 6, pp. 1124-1128, June 2019, doi: 10.1109/LAWP.2019.2910657.

[150] T. -L. Zhang, L. Chen, S. M. Moghaddam, A. U. Zaman and J. Yang,"Millimeter-Wave Ultrawideband Circularly Polarized Planar Array Antenna Using Bold-C Spiral Elements With Concept of Tightly Coupled Array,"

IEEE Trans. Antennas Propag., vol. 69, no. 4, pp. 2013-2022, April 2021, doi: 10.1109/TAP.2020.3026873.

[151] H. Al-Saedi et al.,"A Low-Cost Ka-Band Circularly Polarized Passive Phased-Array Antenna for Mobile Satellite Applications," *IEEE Trans. Antennas Propag.*, vol. 67, no. 1, pp. 221-231, Jan. 2019, doi: 10.1109/TAP.2018.2878335.

[152] J. Huang and J. A. Encinar," *Reflectarray Antennas.*, John Wiley & Sons, 2007.

[153] W. Li et al.,"A Reconfigurable Polarization Converter Using Active Metasurface and Its Application in Horn Antenna," *IEEE Trans. Antennas Propag.*, vol. 64, no. 12, pp. 5281-5290, Dec. 2016, doi: 10.1109/TAP.2016.2620484.

[154] F. Yang and Y. Rahmat-Samii,"A reconfigurable patch antenna using switchable slots for circular polarization diversity*IEEE Microw. Wireless Compon. Lett.*, vol. 12, no. 3, pp. 96-98, March 2002, doi: 10.1109/7260.989863.

[155] S. Gao, A. Sambell, and S. Zhong,"Polarization-agile antennas*IEEE Antennas Propag. Mag..*, vol. 48, pp. 28-37, 2006.

[156] W. Cao, A. Liu, B. Zhang, T. Yu, and Z. Qian,"Dual-band spiral patch slot antenna with omnidirectional CP and unidirectional CP properties," *IEEE Trans. Antennas Propag.*, vol. 61, no. 4, pp. 2286-2289, Apr. 2013.

[157] S.Yan and G. A. E Vandenbosch, "Compact circular polarizer based on chiral twisted double split-ring resonator, " *Appl. Phys. Lett.*, vol. 102, no. 10, p. 103503, Mar. 2013.

[158] www.mouser.in/Search/Refine?Keyword=BAR63-02LE6327.

[159] J. Ren , W. Jiang, K. Zhang,S. Gong, "A High-Gain Circularly Polarized Fabry–Perot Antenna With Wideband Low-RCS Property," *IEEE Antennas Wireless Propag. Lett.*, vol. 17, no. 5, pp. 853-856, 2018.

[160] L. Nama ,S. Bhattacharya ,P. K. Jain, "An Ultra-thin Wideband Linear to Circular Polarization Converter using Metasurface ," *2018 IEEE International*

Symposium on Antennas and Propagation & USNC/URSI National Radio Science Meeting., July, 2018 Boston, MA.

[161] H. A. Ghalyon , M. Akbari, A. Sebak, "A 30GHz linear-to-circular polarization conversion using two-layer FSS," *2017 IEEE International Symposium on Antennas and Propagation & USNC/URSI National Radio Science Meeting.*, July, 2017; San Diego, CA.

[162] G.-B. Wu, S.-W. Qu, S, "Dual circularly polarized reflectarrays with linearly polarized feed," *IEEE Trans. Antennas Propag.*, vol. 64, no. 10, pp. 4235–4241, Oct. 2016.

[163] M. Hosseini and M. Hakkak, "Characteristics estimation for Jerusalem cross-based artificial magnetic conductors," *IEEE Antennas Wireless Propag. Lett.*, vol. 7, pp. 58–61, Apr. 2008.

[164] H. B. Wang, Y. J. Cheng and Z. N. Chen, "Wideband and Wide-Angle Single-Layered-Substrate Linear-to-Circular Polarization Metasurface Converter," *IEEE Trans. Antennas Propag.*, vol. 68, no. 2, pp. 1186-1191, Feb. 2020.

[165] M. Akbari, M. Farahani, A. Sebak and T. A. Denidni, "Ka-Band Linear to Circular Polarization Converter Based on Multilayer Slab With Broadband Performance," *IEEE Access.*, vol. 5, pp. 17927-17937, 2017, doi: 10.1109/ACCESS.2017.2746800.

[166] M. A. Sofi, K. Saurav and S. K. Koul, "A linear to circular polarization reconfigurable converter based on frequency selective surface," *Microw. Opt. Technol. Lett.*, vol. 63, no. 5, pp. 1425-1433, May 2021, doi:10.1002/mop.32779.

[167] J. Xu, W. Hong, Z. H. Jiang, H. Zhang and K. Wu, "Low-Profile Wideband Vertically Folded Slotted Circular Patch Array for Ka-Band Applications," *IEEE Trans. Antennas Propag.*, vol. 68, no. 9, pp. 6844-6849, Sept. 2020, doi: 10.1109/TAP.2020.3005028.

[168] B. Lee and Y. Yoon, "Low-Profile, Low-Cost, Broadband Millimeter-Wave Antenna Array for High-Data-Rate WPAN Systems," *IEEE Antennas Wireless Propag. Lett.*, vol. 16, pp. 1957-1960, 2017, doi: 10.1109/LAWP.2017.2690440.

[169] S.-J. Park and S.-O. Park, "LHCP and RHCP substrate integrated waveguide antenna arrays for millimeter-wave applications," *IEEE Antennas Wireless Propag. Lett.*, vol. 16, pp. 601-604, 2017.

[170] B. Lin, L. Lv, J. Guo, Z. Liu, X. Ji and J. Wu, "An Ultra-Wideband Reflective Linear-to-Circular Polarization Converter Based on Anisotropic Metasurface," *IEEE Access.*, vol. 8, pp. 82732-82740, April 2020.

[171] O. Fernndez, Gmez, J. Basterrechea and A. Vegas, "Reciprocal Circular Polarization Handedness Conversion Using Chiral Metamaterials," *IEEE Antennas Wireless Propag. Lett.*, vol. 16, pp. 2307-2310, June 2017.

[172] H. B. Wang and Y. J. Cheng, "Single-Layer Dual-Band Linear-to-Circular Polarization Converter With Wide Axial Ratio Bandwidth and Different Polarization Modes," *IEEE Trans. Antennas Propag.*, vol. 67, no. 6, pp. 4296-4301, June 2019.

[173] S. Matos, J. costa, C. fernandes, J. Felicio, A. Almeida, N. Fonseca, "Modular Design of a Dual-Band Dual-Circularly-Polarized Antenna to Feed a Ka-Band Transmit-array for SOTM Ground Terminals," *40th ESA Antenna Workshop - Antenna developments for terrestrial and small-space platforms*, The Netherlands, 2019.

[174] S. Y. Eom et al., "Design and Test of a Mobile Antenna System With Tri-Band Operation for Broadband Satellite Communications and DBS Reception," *IEEE Trans. Antennas Propag.*, vol. 55, no. 11, pp. 3123-3133, Nov. 2007.

[175] S. A. Matos et al., "High Gain Dual-Band Beam-Steering Transmit Array for Satcom Terminals at Ka-Band," *IEEE Trans. Antennas Propag.*, vol. 65, no. 7, pp. 3528-3539, July 2017.

[176] S. A. Matos, J. R. Costa, E. Lima, C. A. Fernandes and N. J. G. Fonseca, "Prototype of a compact mechanically steered Ka-band antenna for satellite on-the-move,"*2016 IEEE International Symposium on Antennas and Propagation (APSURSI)*, Fajardo, 2016, pp. 1487-1488.

[177] L. Di Palma, A. Clemente, L. Dussopt, R. Sauleau, P. Potier and P. Pouliguen, "Circularly Polarized Transmitarray With Sequential Rotation in Ka-Band," *IEEE Trans. Antennas Propag.*, vol. 63, no. 11, pp. 5118-5124, Nov. 2015.

[178] J. S. Silva, E. B. Lima, J. R. Costa, C. A. Fernandes and J. R. Mosig, "Tx-Rx Lens-Based Satellite-on-the-Move Ka-Band Antenna," *IEEE Antennas Wireless Propag. Lett.*, vol. 14, pp. 1408-1411, 2015.

[179] K. -L. Wong, J. -Z. Chen and W. -Y. Li, "Four-Port Wideband Annular-Ring Patch Antenna Generating Four Decoupled Waves for 5G Multi-Input-Multi-Output Access Points," *IEEE Trans. Antennas Propag.*, doi: 10.1109/TAP.2020.3025237.

[180] K. Saurav, N. K. Mallat and Y. M. M. Antar, "A Three-Port Polarization and Pattern Diversity Ring Antenna," *IEEE Antennas Wireless Propag. Lett.*, vol. 17, no. 7, pp. 1324-1328, July 2018.

[181] S. M. Mikki and Y. M. M. Antar, "On Cross Correlation in Antenna Arrays With Applications to Spatial Diversity and MIMO Systems," *IEEE Trans. Antennas Propag.*, vol. 63, no. 4, pp. 1798-1810, April 2015.

[182] S. Karamzadeh and M. Kartal, "Circularly polarised MIMO tapered slot antenna array for C-band application," *Electron. Lett.*, vol. 51, no. 18, pp. 1394-1396, 2015.

[183] S. Chakraborty, M. A. Rahman, M. A. Hossain, E. Nishiyama and I. Toyoda, "Design of a 5G Compatible Two-Element Dual-Band Circularly Polarized MIMO Antenna," *2019 Asia-Pacific Microwave Conference*, Singapore, 2019, pp. 923-925.

[184] A. Gaya, M. H. Jamaluddin, I. Ali and H. Mohamad, "Dual Band Circularly Polarized Rectangular Dielectric Resonator Antenna for millimeter wave 5G Applications," *2019 IEEE Asia-Pacific Conference on Applied Electromagnetics (APACE)*, Melacca, Malaysia, 2019, pp. 1-5.

[185] N. Hussain, M. Jeong, A. Abbas and N. Kim, "Metasurface-Based Single-Layer Wideband Circularly Polarized MIMO Antenna for 5G Millimeter-Wave Systems," *IEEE Access.*, vol. 8, pp. 130293-130304, 2020.

[186] A. Iqbal, A. Smida, A. J. Alazemi, M. I. Waly, N. Khaddaj Mallat and S. Kim, "Wideband Circularly Polarized MIMO Antenna for High Data Wearable Biotelemetric Devices," *IEEE Access.*,vol. 8, pp. 17935-17944, 2020.

[187] L. Qu, H. Piao, Y. Qu, H. Kim and H. Kim, "Circularly polarised MIMO ground radiation antennas for wearable devices," *Electron. Lett.*,vol. 54, no. 4, pp. 189-190, 2018.

[188] G. Bharti , D .Kumar , A. K. Gautam and A. Sharma, "Two-port dual-band circularly polarized dielectric resonator-based MIMO antenna with polarization diversity," *Electromagnetics.*,vol. 40, no. 7, pp. 463-478, 2020.

[189] S. Saxena, B. K. Kanaujia, S. Dwari, S. Kumar, H. C. Choi and K. W. Kim, "Planar Four-Port Dual Circularly-Polarized MIMO Antenna for Sub-6 GHz Band," *IEEE Access.*, vol. 8, pp. 90779-90791, 2020, doi: 10.1109/ACCESS.2020.2993897.

[190] K. -L. Wong, J. -Z. Chen and W. -Y. Li, "Four-Port Wideband Annular-Ring Patch Antenna Generating Four Decoupled Waves for 5G Multi-Input-Multi-Output Access Points," *IEEE Trans. Antennas Propag.*, doi: 10.1109/TAP.2020.3025237.

[191] A. Desai, C. D. Bui, J. Patel, T. Upadhyaya, G. Byun and T. K. Nguyen, "Compact Wideband Four Element Optically Transparent MIMO Antenna for mm-Wave 5G Applications," *IEEE Access.*, vol. 8, pp. 194206-194217, 2020, doi: 10.1109/ACCESS.2020.3033314.

[192] H. T. Chattha, "4-Port 2-Element MIMO Antenna for 5G Portable Applications," *IEEE Access.*, vol. 7, pp. 96516-96520, 2019, doi: 10.1109/ACCESS.2019.2925351.

[193] M. Akbari, H. Abo Ghalyon, M. Farahani, A. Sebak and T. A. Denidni, "Spatially Decoupling of CP Antennas Based on FSS for 30-GHz MIMO Systems," *IEEE Access.*, vol. 5, pp. 6527-6537, 2017.

[194] W. Li, K. W. Leung and N. Yang, "Omnidirectional Dielectric Resonator Antenna With a Planar Feed for Circular Polarization Diversity Design," *IEEE Trans. Antennas Propag.*, vol. 66, no. 3, pp. 1189-1197, March 2018.

[195] N. Hussain, M. Jeong, J. Park and N. Kim, "A Broadband Circularly Polarized Fabry-Perot Resonant Antenna Using A Single-Layered PRS for 5G MIMO Applications," *IEEE Access.*, vol. 7, pp. 42897-42907, 2019.

List of publications

Journals

1. **M. A. Sofi**, K. Saurav and S. K. Koul, "Frequency-Selective Surface-Based Compact Single Substrate Layer Dual-Band Transmission-Type Linear-to-Circular Polarization Converter," ***IEEE Transaction on Microwave Theory and Techniques***, vol. 68, no. 10, pp. 4138-4149, Oct. 2020, doi: 10.1109/TMTT.2020.3002248.

2. **M. A. Sofi**, K. Saurav and S. K. Koul, "A linear to circular polarization reconfigurable converter based on frequency selective surface," ***Microwave and Optical Technology Letters***, vol. 63, pp. 1425-1433, 2021.

3. **M. A. Sofi**, K. Saurav and S. K. Koul, "Four-Port Orthogonal Circularly Polarized Dual-Band MIMO Antenna With Polarization and Spatial Diversity Using A Dual-Band Linear-to-Circular Polarization Converter," ***IEEE Transaction on Antennas and Propagation***, Under Review (Revision Submitted).

4. **M. A. Sofi**, K. Saurav and S. K. Koul, "Linear-to-Circular Polarization Converter with Wide Angular Stability and Near Unity Ellipticity- Application to Linearly Polarized Antenna Array," ***IEEE Transaction on Antennas and Propagation***, Under Review.

Conferences

1. **M. A. Sofi**, K. Saurav and S. K. Koul "A Dual Band Linear to Circular Polarization Converter for Satellite Communication," ***2019 IEEE Asia-Pacific Microwave Conference (APMC)***, Singapore, 2019, pp. 563-565.

2. **M. A. Sofi**, K. Saurav and S. K. Koul, “Reconfigurable Polarization Converter Printed on Single Substrate Layer Frequency Selective Surface,” ***2019 IEEE MTT-S International Microwave and RF Conference (IMARC)***, Mumbai, India, 2019, pp. 1-4, doi: 10.1109/IMaRC45935.2019.9118663.

3. **M. A. Sofi**, K. Saurav and S. K. Koul, “A Linear-to-Circular Polarization Converter with Wide Angular Stability and High Ellipticity for Ka-Band Applications,” ***2021 European Microwave Conference***, London, UK. Accepted